

**STUDY OF Ge NANOSTRUCTURES EMBEDDED IN MBE
GROWN Si/Ge MULTILAYERS**

By

MANJULA SHARMA

PHY05200704011

Saha Institute of Nuclear Physics, Kolkata

A thesis submitted to the

Board of Studies in Physical Sciences

In partial fulfillment of requirements

for the Degree of

DOCTOR OF PHILOSOPHY

of

HOMI BHABHA NATIONAL INSTITUTE



February, 2015

Homi Bhabha National Institute

Recommendations of the Viva-Voce Committee

As members of the Viva Voce Committee, we certify that we have read the dissertation prepared by Manjula Sharma entitled “Study of Ge nanostructures embedded in MBE grown Si/Ge multilayers” and recommend that it may be accepted as fulfilling the thesis requirement for the award of Degree of Doctor of Philosophy.

Chairman-

Date:

Guide/Convener- Prof. Milan K. Sanyal

Date:

Member 1 -

Date:

Member 2 -

Date:

Member 3-

Date:

Final approval and acceptance of this thesis is contingent upon the candidate's submission of the final copies of the thesis to HBNI.

I hereby certify that I have read this thesis prepared under my direction and recommend that it may be accepted as fulfilling the thesis requirement.

Date:
Place:

Prof. Milan K. Sanyal
(Guide)

STATEMENT BY AUTHOR

This dissertation has been submitted in partial fulfillment of requirements for an advanced degree at Homi Bhabha National Institute (HBNI) and is deposited in the Library to be made available to borrowers under rules of the HBNI.

Brief quotations from this dissertation are allowable without special permission, provided that accurate acknowledgement of source is made. Requests for permission for extended quotation from or reproduction of this manuscript in whole or in part may be granted by the Competent Authority of HBNI when in his or her judgment the proposed use of the material is in the interests of scholarship. In all other instances, however, permission must be obtained from the author.

Signature

MANJULA SHARMA

DECLARATION

I, hereby declare that the investigation presented in the thesis has been carried out by me. The work is original and has not been submitted earlier as a whole or in part for a degree / diploma at this or any other Institution / University.

Signature

MANJULA SHARMA

List of Publications arising from the thesis

Journal

1. Surface and Interfacial structural characterization of MBE grown Si/Ge multilayers, B. Saha, **M. Sharma**, A. Sarma, A. Rath, P.V. Satyam, P. Chakraborty, M. K. Sanyal, *Applied Surface Science*, **2009**, 256, 547.
2. Structural and Morphological characterization of MBE grown Si/Ge multilayers using X-ray scattering techniques, **M. Sharma**, M. K. Sanyal, M. Mukhopadhyay, M. K. Bera, B. Saha and P. Chakraborty, *Journal of Applied Physics*, **2011**, 110, 102204.
3. Anomalous x-ray Scattering study of the growth of Inverted-Quantum-Hut Structures in Si-Ge Superlattice emitting strong Photoluminescence, **M. Sharma**, M. K. Sanyal, B. Satpati, O. H. Seeck and S. K. Ray, *Physical Review B*, **2014**, 89, 205304.
4. Excitation power-independent photoluminescence of inverted quantum hut structures embedded in SiGe superlattice, **M. Sharma**, M. K. Sanyal, A. Katiyar and S. K. Ray, *Applied Physics A*, *Accepted*.

Communicated:

1. Grazing incidence x-ray diffraction study to extract structure and composition of InAs quantum dots deposited on GaAs as a function of in-plane dot density, **M. Sharma**, M. K. Sanyal, I. Farrer, D. Ritchie.

Conferences

1. Application of x-ray scattering techniques for semiconductor-based quantum structures, **M. Sharma**, M. K. Sanyal, B. Saha, P. Chakraborty, 4th International Conference on Computers and Devices for Communication, *IEEE*, 1-3 (2009).
2. Anomalous X-ray Scattering study of quantum dots embedded in MBE grown Silicon/Germanium multilayers, **M. Sharma**, M. K. Sanyal and M. K. Mukhopadhyay, Solid State Physics: Proceedings of the 57th DAE Solid State Physics Symposium 2012, *AIP Conference Proceedings*, 1512, 738-739 (2012).

Signature
MANJULA SHARMA

To my family...

ACKNOWLEDGEMENTS

I would like to take this opportunity to express my deep gratitude towards my guide Prof. Milan Kumar Sanyal for introducing me to the fascinating field of Nanoscience. Apart from being an exceptional teacher, experimentalist and guide, he has always been a constant source of motivation and encouragement for the last six years. He imparted me with the opportunity to work on one of the best state-of-the-art machines, Molecular Beam Epitaxy setup and gave full freedom of work. He has always found time from his extremely busy schedule to do hectic experiments at several beamtimes which will always remain an inspiration. Due to his immense experience and objective approach towards experiments and data-analysis, the discussions with him have always been extremely informative leading to solution of the problems and also giving me a new perspective to deal with them. He is always very optimistic, full of enthusiasm and extremely supportive. It has been a wonderful experience working with him.

I would like to thank Prof. P. Chakraborty, Prof. A. Datta, Prof. D. Ghose, Prof. M. K. Mukhopadhyay, Dr. B. Satpati, Prof. K. S. R. Menon and Prof. S. Bhunia for their help and many useful discussions during this thesis work. I am also thankful to Dr. Oliver H. Seeck of Petra III, DESY, Germany and Prof. S. K. Ray of IIT, Kharagpur for allowing me to work single-handedly (on several occasions) in their respective beamline and lab to carry out useful experiments for this thesis work.

I would also thankfully acknowledge my seniors Mrinmay-da and Mrinal-da for their great help during my initial years in research. I have learned many details of the X-ray scattering experiments while working with them at Indian Beamline, Photon Factory, Japan. I am thankful to Mr. Avijit Das, Mr. Susanta Banerjee, Mr. Mukul Das, Mr. Subhashish Sanyal and Mr. Souvik Banerjee for their

help. It is my pleasure to acknowledge seniors Atikur-da, Indranil-da, Biswajit-da, Subarna-di, Rupak-da, Sirshendu-da, Suman-da, Abhisakh-da, Paramita-di, Safiul-da and juniors Santanu, Jayanta, Arpan, Sumona, Ishani, Mala, Debasree, Suvankar, Arka, Rajendra, Gouranga, Tapas, Uttam, Ashish and Arnab. They provided a nice and cooperative environment for work.

Atlast, I am thankful to my family who stood by me through every thick and thin I have been through. They have continuously extended their unconditional love, blessings, support and patience to me in most difficult of times, which always kept me on track. I am taking this special opportunity to thank my eldest brother, Yogesh Kumar Sharma, who has always believed in me. I owe a lot to my family for their enormous support throughout.

MANJULA SHARMA

SYNOPSIS

The 4% lattice mismatch between Si and Ge leads to the presence of an inherent strain in the epitaxial $\text{Si}_{1-x}\text{Ge}_x$ layers on Si. The presence of strain in these layers induces change in their band-structure and hence affect their electronic and optical properties substantially. Thus, strained Si/Ge heterostructures offer a means of tailoring the properties of semiconductors, such as band gap and carrier mobility in the devices and show a strong potential to produce devices with superior performance. High efficiency of these devices depends upon how well the band structure is engineered which leads to the confinement of electrons and holes in such heterostructures. Thus, performance of a device is critically linked to the composition and the strain present in SiGe layers as both of these influence the band structure. Monolithic integration of SiGe optoelectronic devices with well-developed very-large-scale-integration (VLSI) technology can reduce the production cost of devices hugely.

This thesis work focusses on the study of growth aspects of Ge nanostructures in Si/Ge multilayers by Molecular Beam Epitaxy (MBE) technique. The growth of SiGe on Si is generally described by classical Stranski-Krastanov (SK) process where the first three deposited Ge monolayers contribute to the wet-layer and then the formation of 3-D nanostructures (quantum dots) take place which is governed by the competition between kinetics and thermodynamics. However, the growth of SiGe films involves in fact more complex mechanisms not accounted for in the simplified SK growth process like interdiffusion with the lower layers and the manifestation of nonuniform stress fields in the subsurface regions. Thus, a modified SK growth mode is generally followed in the deposition of Si/Ge multilayers, which leads to a large amount of interfacial intermixing and also occurrence of nanostructures which are different from the conventional quantum dots obtained

in these multilayers. Generally quantum dots form in Si/Ge multilayers with their tip pointing towards the top surface, however at low growth temperatures, we have observed the formation of a new kind of Ge quantum huts with their base lying at the wet-layer and tip pointing towards the substrate. These nanostructures are identified as ‘Inverted Quantum Huts’ (IQH) in this thesis work. These IQH are observed to show high photoluminescence emission with a band-lineup to be of Type-I which is unlike the conventional quantum dots owing to lower strain in the IQH structures. Apart from this, the strain and intermixing occurring in InAs quantum dots formed on GaAs substrate by MBE technique have also been studied.

X-ray scattering techniques such as x-ray reflectivity, x-ray diffraction and anomalous grazing incidence x-ray diffraction have been used extensively to understand the growth mechanism of such multilayers. X-ray scattering experiments have been mainly performed at Indian Beamline, Photon Factory, Japan and Petra III, Germany synchrotron facilities. Also, cross-sectional transmission electron microscopy (XTEM) technique has been utilized to obtain a first-hand information of the Si/Ge interfaces. Following is the outline of the present thesis.

Chapter 1 provides a brief introduction of the growth mechanisms involved in epitaxial growth of Ge on Si. It gives an initiation of the idea of strain relaxation processes that occur in Si-Ge heteroepitaxy. Optimization of growth parameters in order to reduce undesirable misfit dislocations and plastic relaxation is discussed here followed by a brief review of conventional quantum dots which are obtained in SiGe superlattices.

Chapter 2 is devoted to the brief description of the various experimental techniques and instruments used during this thesis work. These include Molecular Beam Epitaxy setup, X-ray scattering facilities i.e. laboratory source and synchrotron source, Transmission electron microscopy and its special sample prepara-

ration for cross-sectional view, Atomic force microscopy and Optical techniques i.e., Photoluminescence spectroscopy and Raman spectroscopy.

Chapter 3 is based on the theoretical formalisms of X-ray scattering. X-ray scattering provides statistically averaged and useful information about the system in a non-destructive manner. Depending upon the geometry used, this technique allows to probe intermixing and strain at the buried interfaces and can also yield highly surface sensitive information such as about the quantum dots on top surface. As this thesis work is based mainly on the X-ray scattering technique, a full chapter is devoted to provide a base.

Chapter 4 gives detailed information about the growth method of Si/Ge multilayers. It is shown that how by choosing proper growth conditions, one can move from Si/Ge multilayer system which consists of large misfit dislocations to a Si/Ge superlattice system with negligible plastic dislocations. Interfacial Si-Ge intermixing and strain have been studied and it is found that intermixing increases with the growth temperature and decreases as the deposition rate is increased. A consistent analysis of specular reflectivity and diffraction profile is presented which provided valuable structural information as a function of depth.

Chapter 5 deals with the study of the formation of Inverted Quantum Hut (IQH) structures which form in the SiGe superlattice structure at low growth temperatures. Consistent results of XTEM, GID and out-of-plane XRD provide a simple model to explain the growth mechanism of these IQH. It is shown that the deposited Ge layer relaxes strain by uniform intermixing with the previously deposited lower Si layer to form a $\text{Si}_{0.6}\text{Ge}_{0.4}$ wet layer exhibiting an out-of-plane lattice parameter of 5.64 Å and an in-plane lattice parameter close to the Silicon value of 5.43 Å. The IQH structure forms with its base just below the wet layer. The anomalous x-ray scattering measurements have revealed interesting composition variation in this IQH structure from base to tip.

Chapter 6 present the results of a photoluminescence study of the IQH structures. Unlike conventional Ge quantum dots formed above Ge-on-Si interfaces, the presented quantum structures exhibit excitation-power independent photoluminescence energy which indicate a Type-I kind of band lineup in these structures.

Chapter 7 provide a study of the InAs quantum dots grown on GaAs substrate using MBE technique. Although this thesis work is primarily concerned with SiGe nano structure, we have shown here that the techniques developed by us in this thesis can also applied to other semiconductor nano structures. InGaAs quantum dots are very important for technological applications and we show here that the developed methods in this thesis can be used in these III-V systems to tune structure-spectroscopy relationship. The GID study provides us statistically averaged information regarding the composition and the size of the QD which is consistent with the results obtained from the AFM study. AFM measurements suggest the coalescence of small quantum dots to form uniformly sized larger quantum dots for the higher deposition temperature. This coalescence and absence of it lead to variation in In-Ga intermixing (observed from GID measurements) inside the quantum dots deposited at different growth temperatures. Relatively low variation of In composition within quantum dot structures present in high in-plane density region exhibit sharper PL emission.

Contents

1	Introduction	1
1.1	Growth Mechanism	6
1.2	Si-Ge Heteroepitaxy	12
1.3	Optimization of Growth	14
1.4	General Discussion	18
1.5	Quantum Dot Superlattice: Review	20
2	Experimental Techniques	23
2.1	Molecular Beam Epitaxy	23
2.1.1	MBE Basics	24
2.1.2	Outline of the MBE system	25
2.2	X-Ray Scattering Facility	31
2.2.1	Laboratory Source	32
2.2.2	Synchrotron Source	33
2.3	Transmission Electron Microscopy	38
2.4	Atomic Force Microscopy	44
2.5	Optical Techniques	49
3	X-ray Scattering Techniques	57
3.1	X-ray Diffraction	58
3.2	X-ray Reflectivity	66
3.2.1	Parrat Formalism	66
3.2.2	Scheme based on Distorted Wave Born Approximation	71
3.3	X-ray Diffuse Scattering	74
3.4	Grazing Incidence Diffraction	78
3.5	Anomalous X-ray Scattering	81
4	MBE growth of Si-Ge Multilayers	83
4.1	Si/Ge multilayers showing plastic relaxation	86

4.2	Si-Ge Superlattices	89
4.2.1	XTEM Study	89
4.2.2	Raman scattering	90
4.2.3	XRD Study	98
4.3	Interfacial intermixing and strain	104
4.3.1	Electron density profile	105
4.3.2	Strain profile	109
4.3.3	Summary of results	111
4.4	Conclusion	113
5	Quantum Structures in SiGe Superlattice	115
5.1	Formation of Inverted Quantum Huts	116
5.2	Experimental Details	118
5.3	Results and Discussion	119
5.3.1	In-plane Structure	120
5.3.2	Out-of-plane Structure	127
5.3.3	Growth Mechanism	129
5.4	Conclusion	133
6	Excitation-power independent Photoluminescence in Inverted-Quantum-Hut Structures	135
6.1	Introduction	137
6.2	Experimental Details	139
6.3	Results and Discussion	144
6.4	Conclusion	149
7	Extraction of structure and composition of InAs quantum dots grown on GaAs substrate as a function of in-plane dot separation	151
7.1	Introduction	152
7.2	Experimental Details	154
7.3	Results and Discussion	157
7.4	Conclusion	168
	Bibliography	169

List of Figures

1.1	Schematic diagram of the three possible growth modes.	7
1.2	Schematic illustration of major processes occurring during growth on a substrate surface.	10
1.3	Schematic showing the strain relaxation occurring during heteroepitaxy by elastic and inelastic means.	13
1.4	Critical thicknesses of smooth strained SiGe layers on (001) Si for relaxation by dislocation formation at high and moderate substrate temperature d_{MB} and d_{DT} . (Ref. [17])	15
1.5	XTEM of Si/Ge multilayer sample ($T_G= 550^\circ\text{C}$, Si/Ge:110/40 Å) showing inelastic relaxation.	16
1.6	XTEM of Si/SiGe alloy multilayer sample ($x=48\%$, $T_G = 750^\circ\text{C}$, Si/SiGe : 175/100 Å) showing completely pseudomorphic layers.	17
1.7	HAADF STEM cross section images of island superlattices grown by MBE ($\text{Si}_{0.54}\text{Ge}_{0.46}/\text{Si}$ superlattice with 3.4 nm thick alloy layers and 13.7 nm Si spacers, grown at 625°C) (Ref. [24]).	20
2.1	Schematic diagram of a Molecular Beam Epitaxy setup.	26
2.2	A typical Effusion Cell.	28
2.3	Molecular Beam Epitaxy setup present at Saha Institute of Nuclear Physics.	28
2.4	Schematic of a typical Synchrotron source	34
2.5	Diffractometer at Indian Beamline, Photon Factory, Japan.	36
2.6	Line diagram of the diffractometer at Indian Beamline, Photon Factory, Japan.	37
2.7	Schematic showing formation of HRTEM image and SAED pattern in TEM.	39
2.8	Step flow of XTEM sample preparation method.	42

2.9	Step flow of XTEM sample preparation method continued after steps in Figure 2.8.	43
2.10	Schematic illustration of AFM.	45
2.11	Dependence of force on the distance between the tip and sample.	47
2.12	Electronic band-structure for Ge and Si.	51
2.13	Band gap variation of $Si_{1-x}Ge_x$ alloys against Ge content x . The top curve gives the band gap energy for unstrained (cubic) alloys, which show a crossover from the Si-like (conduction band minima at Δ) to the Ge-like bandstructure (conduction band minima at the L point) at $x = 0.85$. The two other curves are for pseudomorphic $Si_{1-x}Ge_x$ layers on a cubic Si substrate, which leads to a splitting of the valence band.	52
2.14	Band structures of type I and type II. In the former one the confinement of both electrons and holes is taking place in the same layer contrary to what is happening in the latter one. The dashed lines represent the energies of the confined particles.	54
3.1	(a) Definition of the real space vectors. The origin of the crystal is shown, point A is the origin for the n^{th} unit cell, point B is the j^{th} atom of the n^{th} unit cell and point C is an electron belonging to the j^{th} atom of the n^{th} unit cell. (b) Definition of the reciprocal space incident and exit wave vectors k_i and k_f . These wave vectors both have magnitude $2\pi/\lambda$, with λ being the x-ray wavelength. The momentum transfer q is $k_f - k_i$	59
3.2	Schematic showing the GIXS scattering geometry.	65
3.3	Schematic showing reflection and refraction of incident X-rays for Vacuum-Medium interface.	67
3.4	Schematic showing reflection and transmission of incident X-rays for a thin film sandwiched between two media.	69
3.5	Specular reflectivity of the test 5 bilayer Si/Ge system. Black filled circles represent the 'Data' and red line the profile obtained from DWBA formalism. The inset shows the EDP used to generate Data (black symbols) and EDP obtained by fitting (blue line), using DWBA formalism. The horizontal (red) line in the inset shows the value of AED, ρ_0	73

3.6	A typical rough surface. For an isotropic rough surface the height correlation functions depends on r , irrespective of the location of the points (x, y) and (x', y')	75
3.7	Schematic showing the GID scattering geometry.	78
3.8	Anomalous corrections f' and f'' for Ge in the vicinity of the K-absorption edge. [Ref: [98]]	82
4.1	XTEM images (a) of a 4 bilayer Si/Ge multilayer sample and (b) its High resolution TEM micrograph. The presence of misfit dislocations is evident and are indicated by arrows.	86
4.2	SIMS depth profile of the four bilayer sample. The profiles for Si and Ge are indicated. Separate layers of Si and Ge can be observed as the presence of Ge (peak in Ge profile) leads to absence of Si (dip in Si profile).	87
4.3	X-ray diffraction profile of the four bilayer sample. The sharp peak corresponds to Si and the broad one is due to the presence of Ge in almost relaxed state.	87
4.4	(a) and (b) XTEM and high resolution XTEM images for SG7. Dark lines correspond to the presence of pure Ge and lighter portion corresponds to Si.	91
4.5	High resolution XTEM image of SG7 showing formation of inverted quantum huts.	91
4.6	XTEM image for SG16. Lower Ge layers can be seen to have undergone large intermixing with the Si layers leading to strain relaxation in them. However, the upper layers do not show much intermixing. The superlattice sample consists of inverted Ge-huts which are stacked over one-another in various Ge-layers. Quantum hut stacking allows elastic strain relaxation in these epitaxial layers.	92
4.7	XTEM image for SG5. This sample consists of alternate Si and SiGe alloy ($x_{Ge} = 0.57$) layer. There is clearly no sign of elastic or plastic relaxation in these layers.	92
4.8	XTEM image for SG6. This sample consists of alternate Si and SiGe alloy ($x_{Ge} = 0.34$) layer. There is clearly no sign of elastic or plastic relaxation in these layers.	93

4.9	XTEM image for SG8. This sample consists of alternate Si and SiGe alloy ($x_{Ge} = 0.48$) layer. These are highly commensurate layers with no visible form of elastic or plastic relaxation.	93
4.10	Raman spectra for pure Si/Ge superlattices. Insets show the zoomed-in peaks for Ge-Ge and Si-Ge modes.	94
4.11	Raman spectra for Si/SiGe superlattices. The Si-Ge mode peak is highly pronounced due to very high alloy content in these superlattices.	95
4.12	The black curve is experimental XRD profile of SG16 and red curve is the calculated diffraction profile by taking sharp interfaces i.e., no interfacial alloying. Inset shows the variation of Ge content with depth. Clearly, the calculation doesn't fits the experimental data.	100
4.13	Experimental and calculated x-ray diffraction profile for SG16. Inset shows the Ge content as a function of depth. The interfaces are taken to as intermixed with a linear variation in the Ge content.	101
4.14	Experimental and calculated x-ray diffraction profile for SG5. Inset shows the Ge content as a function of depth.	102
4.15	Experimental and calculated x-ray diffraction profile for SG6. Inset shows the Ge content as a function of depth.	103
4.16	Experimental and calculated x-ray diffraction profile for SG8. Inset shows the Ge content as a function of depth.	103
4.17	Schematic representation of the Si/Ge 10 bilayer superlattice on Si(001). The thicknesses are nominal as obtained from the MBE growth conditions. The total thickness of the multilayer structure was taken as 1500 Å for XRR analysis.	106
4.18	The measured X-ray reflectivity curve of the Si/Ge 10 bilayer stack is shown by black filled circles. The red line represents the fitted reflectivity curve obtained by DWBA method. Inset shows the obtained EDP of the studied Si/Ge multilayer system containing 10 bilayers.	108
4.19	The measured X-ray diffraction profile of the sample is shown in black filled circles and the red line shows the generated profile obtained by Born's Approximation. The highest peak corresponds to the substrate Si(004). The numbers represent the order of superlattice satellite peaks.	108

- 4.20 Figure shows the electron density variation in the multilayer stack. The blue curve shows the EDP obtained from X-ray reflectivity calculations and red curve shows the structural profile obtained from the fitting of XRD data. 109
- 4.21 Left axis shows the variation in fractional content of Si and Ge in the second and third bilayers. Fractions of Si and Ge have been represented by red and blue curves respectively. The right axis shows the % strain with respect to Si (consider blue curve) in the second and third bilayers of the superlattice stack. 110
- 5.1 (a) STEM-HAADF image of the superlattice structure. Brighter lines correspond to Ge layers while the gray portions are Si. Buffer (B) and cap (C) layers are indicated. (b) STEM-EDX line profile along the line shown in (a). The line profile is taken over the IQH stack in various layers. (c) Ge EDX profile using bars of equal thickness ($\sim 13 \text{ \AA}$) for the lowest three Si-Ge bilayers. (d) High-resolution XTEM micrograph of self-organized IQH structures formed in a Si-Ge superlattice sample. 'B' and 'C' indicate the location of buffer and cap layer respectively. 121
- 5.2 (a) and (b) show two-dimensional GID data of the superlattice sample shown in Fig. 5.1(a) at the Ge K-edge (11 103 eV) energy and away from it (11 043 eV) respectively around (800). (c) The extracted radial scans for the superlattice structure at the two energies as indicated, around (800). This plot is generated by integrating the counts on Mythen detector for each $a_{||}$. Also shown is the (800) profile for Si substrate for comparison. (d), (e) and (f) Variation of Ge concentration, in-plane strain and out-of-plane lattice parameter respectively with the in-plane lattice parameter as obtained from (800) radial scans. Refer text for details about the shaded region in (f). 124
- 5.3 (a) Experimental data and calculated XRD profile of the superlattice structure. (b), (c) and (d) Variation in lattice parameter, out-of-plane strain (ε_{\perp}) and Ge fraction (x) respectively with depth as obtained from the XRD data analysis. Insets in (b), (c) and (d) show the expanded version of one bilayer for clarity. 128

- 5.4 (a) and (b) Angular scans around (400) of the superlattice sample measured at 11 043eV and 11 103eV respectively. Each scan is associated with a different $a_{||}$ as indicated in the plot. The solid lines show fits assuming IQH composed of five disks having same in-plane lattice parameter. (c) the Ge fraction variation over the disk radially used for fitting. (d) Variation of the isostrain region with $a_{||}$ as obtained from the fits. Inset shows the schematic (not upto scale) of the IQH being divided into disks of isostrain region. The dark border represents the rim area having higher Ge concentration as observed in the XTEM images and also included in the calculation of fitted curves (refer text for further details). 132
- 6.1 (a) HAADF image of IQH embedded superlattice structure. Stacking of IQH in various layers is evident. (b) High resolution XTEM image of self organized IQHs embedded in the superlattice structure. 139
- 6.2 Angular scans around (400) of the IQH embedded superlattice structure measured at 11043 eV. Each scan is associated with a different $a_{||}$. The solid lines show fits assuming the IQH to be composed of five disks having same in-plane lattice parameter. The diameter of the disks for different $a_{||}$ is indicated. 141
- 6.3 Schematic showing a typical bilayer consisting of IQH structures. The various dimensions (as indicated) represent the results as obtained from the analysis of x-ray data. 143
- 6.4 (a) Temperature dependence of the IQH embedded superlattice PL spectra. The PL spectra at low temperature can be fit using three gaussians as indicated by three dash-dot curves for 10 K spectrum. (b) and (c) Temperature dependence of PL peak positions and IPL respectively of the three peaks corresponding to IQH, TO_{WL} and NP_{WL} . At higher temperatures (60 K and above) only IQH related PL is observed. 145
- 6.5 (a) The excitation power dependent PL spectra at 10 K. (b) and (c) show the power dependence of the PL peak energies and the I_{PL} respectively for the three Gaussian at 10 K. 146

- 6.6 (a) I_0/I_{PL} versus temperature plot for IQH related emission. The line profile represents the fit considering two activation energies (12.2 and 51.6 meV). Also, calculation of the intensity variation is shown for activation energy of 12.2 meV. (b) Temperature variation of PL peak position and fit by Varshni's relation for IQH related emission. (c) Variation of integrated PL intensity for the three peaks with excitation power. The line profiles represent the power law ($I \propto P^m$) fit for the IQH and NP_{WL} peaks. The corresponding power exponents are indicated. 147
- 7.1 (a) and (b) AFM images of InAs quantum dots formed on the top surface of the substrate at centre and edge respectively. Insets show the 3-D view of a single QD in the respective low and high density regions. 155
- 7.2 (a) and (b) Size distribution of the QD in the respective low and high QD density regions as obtained from the AFM analysis software WSxM. 157
- 7.3 (a) and (b) Two-dimensional GID data around (200) for the high and low QD density regions respectively. Y-axis represents the exit angle in the Mythen detector. (c) and (d) Line profile of the radial scans around (200) and (400) as indicated for the high and low QD density regions respectively. These line profiles are generated by the integration of all the pixels of mythen detector. Respective insets show the variation of In concentration with $a_{||}$. (e) and (f) Profiles of the absolute strain present in the QD and strain with respect to GaAs (refer text for the method of calculation) as a function of $a_{||}$ for the high and low QD density regions respectively. (g) and (h) Angular scans around (400) corresponding to different in-plane lattice parameters as indicated for the high and low QD regions respectively. 158
- 7.4 Isostrain region (2R) variation with $a_{||}$ for the two QD density regions. The larger 'R' value are chosen from Tables 7.1 and 7.2 for the plot as their contribution is higher. 164

- 7.5 (a) and (b) Experimental exit angle (α_f) spectra corresponding to different $a_{||}$ for high and low QD density regions respectively. (c) Height with respect to the GaAs substrate (refer text for calculation) for different $a_{||}$. (d) The variation of In content with height inside the QD for the two QD densities. 164
- 7.6 Photoluminescence spectra at the low and high QD density regions. 167

List of Tables

4.1	Table contains the Growth Parameters for the various multilayer samples.	90
4.2	Table contains the values used for various constants during the strain calculation.	96
4.3	Table contains the Raman shift peak positions for Ge-Ge mode, Si-Ge mode, Ge-Ge mode peak width and the biaxial and longitudinal strain values.	96
4.4	Table contains the Raman shift peak positions for Ge-Ge mode, Si-Ge mode for the alloy samples.	97
4.5	Table contains the Growth Parameters for the various multilayer samples and the fitting parameters used for XRD simulation. T_G is the growth temperature for various samples. t_1 & t_2 and m_1 & m_2 are the alloy thicknesses and the slope of linear profile considered (for the concentration of Ge variation in alloy) at the Si-on-Ge interface and Ge-on-Si interface respectively. The alloy layer thicknesses (t_1 and t_2) are excluded from Si and Ge layer thicknesses.	104
7.1	High QD density	163
7.2	Low QD density	163

Chapter 1

Introduction

In his famous lecture ‘Plenty of room at the bottom’, Richard P. Feynman in 1959 explored the immense possibilities which can be achieved by miniaturization. Since then, a plenty of work has been done in this field and many new inventions such as scanning tunneling microscope and upgradations in transmission electron microscopes have allowed us to image and control single atoms and molecules. Research in last few decades has also led to the easy accessibility of nanomaterials which show extraordinary properties. Nanomaterials are generally referred to those materials having feature dimensions in the range of 0.1-100 nm. These nanomaterials such as clusters of atoms (quantum dots), fullerenes, carbon nanotubes or biomolecules have novel electronic, optical and chemical properties attributed to their dimensions. Further, by varying their size and controlling their interactions, the fundamental properties of nanostructured materials synthesized from these building blocks may be tuned.

Semiconductor nanostructures are significant from the scientific point of view as they provide a means to create artificial potentials for carriers, i.e. electrons and holes in semiconductors, at length scales comparable to or smaller than the De-Broglie wavelength. Due to such small length scales, quantum mechanical properties such as confinement effects become important. These confinement effects lead to the feasibility of new devices. Restrictions (such as indirect band-gaps) which arise due to the material property are shifted or lifted and hence, electronic band structure of the semiconductors can be engineered [1, 2]. Semiconductor nanostructures in the form of quantum wells, quantum wires and quantum dots are very important as they offer confinement in one, two and three dimensions respectively. Some examples of devices which are based on the electronic band offsets and the sub-band structure in superlattice and quantum well heterostructures are high electron-mobility transistor structures (HEMTs) [3,4], hetero-bipolar transistors (HBTs), inter-band light emitting diodes (LEDs) and laser diodes, inter-band photodiodes, quantum well infrared photodetectors (QWIPs) [5] and quantum cascade laser structures [6] with intra-band emission in the mid-infrared spectral range. The realization of zero-dimensional objects in which the electrons are confined in all three dimensions, the so-called quantum dots, have attracted a lot of attention for their applications in optoelectronics [7, 8] and quantum information technology.

Semiconductor nanostructures become even more important due to the saturation of complementary metal oxide semiconductor (CMOS) technology. Ac-

According to the Moore's law, the density of integrated MOSFET transistors double every 18 months, which so far has been satisfied. It is observed that scaling down the devices to 25 nm leads to a degradation in their electrical properties. Hence, alternative materials to the CMOS technology have been pursued. Strained Ge and III-V compound semiconductors are found to be the most suitable candidates for replacing the CMOS technology for integration in the well-developed Si very large scale integration (VLSI) microelectronics. These advanced techniques involve the preparation of strained Ge and III-V semiconductor quantum dots. It is hence necessary to develop methods to fabricate these semiconductor quantum dots on a large scale in a controlled manner in order to integrate them into usable devices. In addition to the control of size, an arrangement of the quantum dots in regular arrays is also desired, as by doing so, the quantum dots can be coupled together to enhance their output. The two broad approaches to create nanostructures in a controlled manner are 'top-down' and 'bottom-up' techniques. The top-down approach involves use of lithography techniques such as electron beam lithography, focussed ion beam milling, selective chemical etching or photolithography. These sophisticated lithography techniques lead to a very high manufacturing cost of the devices and are generally very slow methods as well. In contrast, bottom-up approach utilizes the inherent properties of the material used, to produce organized nanostructures.

Fabrication of nanostructures by bottom-up approach is essentially based on the growth process. In this, generally atoms or molecules are deposited on a

substrate surface and depending upon the material properties, nanostructures are formed. It is non-equilibrium growth process and is governed by the competition between kinetics and thermodynamics. Such self-organized growth is attractive as it yields quantum dots which are free of defects that might degrade their performance. This method also enables growth of very small nanostructures having far-spaced energy levels that are essential for room-temperature operation. Hence, bottom-up approach utilizing self assembly of quantum dots is an alternate cost-effective approach towards this issue. As most of the physical properties of these quantum dots depend upon their shape and size, it is necessary to have a deep insight into the nucleation and growth processes involved. Recent progress in the characterization techniques to understand the growth of various germanium (Ge) quantum structures formed in silicon (Si) lattice have made this research field active again as this development may provide us future optical materials for seamless integration with the present Si-based very large scale integration (VLSI) technology [9, 10].

Self-organization of Ge quantum structures on Si and InAs quantum dots on GaAs by heteroepitaxy opens up a comfortable route to new devices. The heteroepitaxy of these semiconductors is generally realized by advanced growth techniques such as Molecular Beam Epitaxy (MBE) or Chemical Vapor Deposition (CVD). These quantum dots are formed by the Stranski-Krastonov (S-K) growth mode followed in their heteroepitaxy due to the nearly 4% and 7% lattice mismatch between Si/Ge and InAs/GaAs respectively. For both the systems, defect-

free but strained 3D islands form on top of a thin wet-layer during heteroepitaxial growth. Epitaxial multilayers of these semiconductors have been observed to show self organization of such quantum dots in which they stack one over the other in alternate layers due to strain propagation. Lateral ordering of the quantum dots can be achieved by the self-ordering due to elastic interactions. Hence, by choosing proper growth conditions, three-dimensional self assembled quantum dot arrays can be formed. This thesis work mainly deals with the growth and study of Si/Ge multilayers with embedded Ge nano-structures.

These Si/Ge multilayers were prepared using Molecular Beam Epitaxy technique. Apart from Si/Ge multilayers, Ge quantum dots on Si and InAs quantum dots on GaAs were also studied in detail. X-ray scattering and cross-sectional transmission electron microscopy (XTEM) techniques have been used extensively for the characterization of these structures. These techniques are particularly important as they provide information about the buried structures and interfaces present in the system. X-ray scattering is a non-destructive method and provides a statistically averaged information over a few microns of the sample. However, the intensity distribution is in reciprocal space leading to the requirement of a lot of model assumptions and fitting routines for data interpretation. XTEM on the other hand provides a direct image of the interfaces and buried structures with atomic resolution. In this, the information is very localized and lacks generalization over the whole sample. For the structures on the sample surface i.e. quantum dots on the surface, Atomic Force Microscopy (AFM) technique is used to study the

size and density of the structures. In the following sections, a brief introduction of the growth mechanism of Si-Ge heteroepitaxy is provided. Importance of the optimization of growth parameters for the reduction of defects in epitaxy has been discussed. Later, a general discussion of SiGe system is provided followed by a brief review of the quantum dots formed in SiGe superlattice structures.

1.1 Growth Mechanism

The word epitaxy [from the ancient Greek words $\varepsilon\pi\tau$ (on top) and $\tau\alpha\xi\iota\sigma$ (to order)] indicates a growth process in which the impinging atoms attach to an existing crystalline surface by forming layers that have the same order as the original matrix. Heteroepitaxy is therefore defined as an epitaxial growth realized by depositing the atoms on a substrate having different composition. Epitaxial growth is a non-equilibrium kinetic phenomenon. As, in equilibrium conditions, adsorption and desorption from the gas phase occur at the same rate, the same holds for cluster nucleation and decay and there is no net growth. That is, the properties like surface roughness or coverage remain constant in equilibrium conditions. Depending on the relative bond strengths of atoms in the deposited layer and between these atoms and the substrate atoms, as well as the degree of the lattice match between the two materials, that give rise to different thermodynamic conditions, three epitaxial growth modes have been studied and classified so far [11]:

1. Layer by layer growth in lattice matched systems (Frank-Van der Merwe).

This is typically observed in homoepitaxy, for example in the growth of Si on Si or materials having very low lattice mismatch.

2. The layer by layer, then island growth mode (Stranski-Krastanov, SK) in lattice mismatched systems. The SK mode occurs frequently in systems with a small lattice mismatch, for example Ge on Si (4.2%) or InAs on GaAs (7%).
3. The island growth mode (Volmer-Weber). This growth mode, in which islands nucleate on a bare substrate, is typical of systems with a large lattice mismatch.

In this simple description of growth, reaction or interdiffusion is not allowed.

These three growth modes are schematically represented in Fig. 1.1.

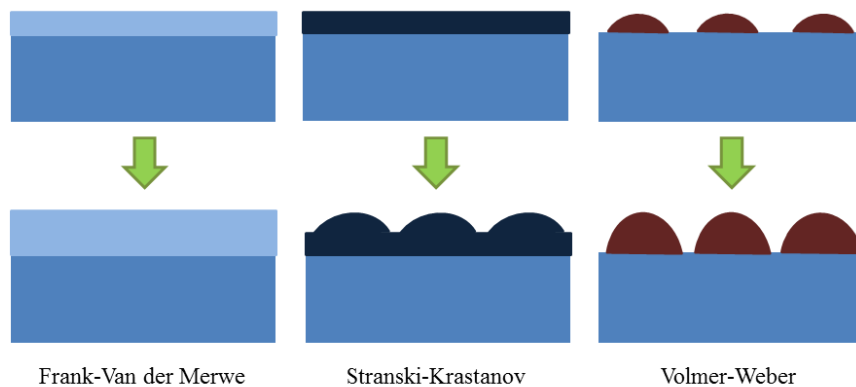


Figure 1.1: Schematic diagram of the three possible growth modes.

The relationship between surface and interfacial free energies [12] gives us a way to predict growth modes. Surface free energy is defined as the free energy to create a unit area of surface on an infinite bulk solid. Given specific (per area)

surface energies for the substrate and film as γ_s , γ_f , respectively (where these are the values for the semi-infinite crystals) and an interfacial energy γ_{in} , where the subscript i stands for interface and n stands for the number of monolayers of film deposited, monolayer-by-monolayer growth occurs only when

$$\Delta\gamma_n = \gamma_{fn} + \gamma_{in} - \gamma_s \leq 0 \quad (1.1)$$

for all values of n . The term γ_{fn} differs from γ_f to allow for an n -dependent surface strain. The term γ_{in} includes the excess free energy needed to create the initial interface between two different materials γ_{i0} , plus the additional free energy arising from strain due to lattice mismatch between the overlayer film and the substrate. In the opposite extreme, one obtains cluster growth when, for all values of n ,

$$\Delta\gamma_n = \gamma_{fn} + \gamma_{in} - \gamma_s \geq 0 \quad (1.2)$$

In this case the over layer doesn't wet the substrate. In the intermediate case, the adlayer initially wets the substrate, but because of lattice mismatch, as n increases, strain energy contributes to γ_{in} to the point at which the film no longer wets. Typically, at this point, misfit dislocations are incorporated to relieve strain and, given sufficient mobility of adatoms, preferential growth will occur in the relaxed region, leading to the nucleation of 3D clusters. Alternately, roughening of the growth front can relieve strain at the expense of additional surface energy. The film thickness at which Equation 1.1 no longer holds is one of the definitions of

the critical thickness, below which the overlayer film grows in registry with the substrate. Equations 1.1 and 1.2 show that it would be quite difficult to grow a coherent strained layer superlattice of two unlike materials A and B. If A wets B, then B will not wet A. The fact that binary strained layer superlattices can be grown shows that more is involved than thermodynamics, that is, kinetics also plays a role. Interdiffusion, chemical reaction, or surface segregation also can change surface wetting and the growth mode as will be presented in this thesis work.

Kinetic Processes

Film growth is a non-equilibrium process in which kinetics play an essential role in determining the film morphology. Kinetic processes can be partly controlled by varying substrate temperature and deposition rate. Deposition of adatoms onto a surface drives the system into supersaturation, from which the system tries to relax back to equilibrium by forming a condensed phase, e.g. 2D islands for an adlayer that wets the substrate. Adatoms move randomly on the surface and, when meeting each other, form islands. All islands larger than the critical nucleus will grow by further addition of adatoms until the supersaturation is eliminated. Another means of removing the supersaturation is by the adsorption of adatoms on those substrate steps that are good sinks. The surface diffusion coefficient determines the relative rates of these processes. From an atomistic point of view, kinetic processes in growth can be categorized into pure migration of adatoms on

a flat terrace and the interactions of adatoms with surface steps.

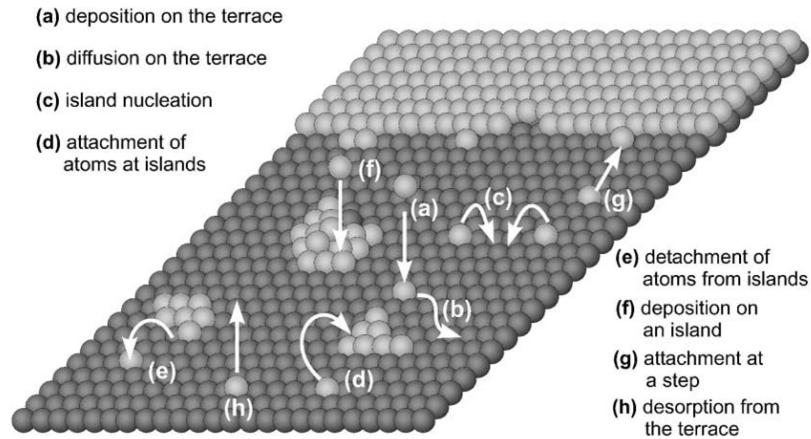


Figure 1.2: Schematic illustration of major processes occurring during growth on a substrate surface.

An adatom, in addition to meeting another to form a nucleus, meeting an existing island, or traveling between existing islands along a concentration gradient (coarsening), may also meet one of these fates: walking into a special sink site like a substrate step, diffusing into the bulk of the substrate, or re-evaporating from the surface as is schematically shown in Fig. 1.2. As the film growth can be performed under conditions far from equilibrium, a variety of growth-front morphologies can be obtained depending on which kinetic process is rate limiting. The three kinetic growth modes observed in homoepitaxy are:

- kinetically rough growth
- layer-by-layer growth
- step-flow growth

The kinetically rough growth occurs in the extreme limit of a high deposition rate and slow lateral diffusion of adatoms, in which atoms migrate only on the order of a few lattice sites before they incorporate into growing film or are buried. In the extreme case, if the surface diffusion coefficient is zero and all adatoms stay where they land, the roughness of the growth front will diverge as the thickness increases. As the growth rate is reduced or the substrate temperature is raised (increasing adatom mobility), the regime of layer-by-layer growth can be achieved. In this growth mode, adatoms have sufficient mobility to find one another, nucleate 2-D islands that grow, coalesce, and ultimately fill in the initial starting surface at ~ 1 monolayer of deposition. The layer-by-layer growth mode usually shows an increase of surface roughness with coverage because the previously deposited layer is never completely filled in before the next layer nucleates. The step-flow growth-mode ensures a smooth surface during deposition. In this case, the surface is like a staircase with atomic-height risers. Step-flow growth is achieved when deposited atoms have sufficient time to migrate and incorporate into a step before other atoms deposited on the surface increases the supersaturation sufficiently to force nucleation on the terraces. To maintain it, one either deposits relatively slowly or heats the substrate to a high enough temperature for adatoms to diffuse far enough to incorporate into steps before nucleating islands.

1.2 Si-Ge Heteroepitaxy

Heteroepitaxy is a bottom-up approach to prepare fine nanostructures without referring to the lithographic techniques. This can be used to fabricate self-organized semiconductor nanostructures and possibly tailor their physical properties. This thesis work is based upon the Si/SiGe heterostructures fabricated on Si(001) using Molecular Beam Epitaxy system.

SiGe alloys are miscible in the whole composition range for temperatures used in epitaxy i.e., 300-750°C [13]. The surface energy of SiGe is lower than that of Si, resulting in two-dimensional growth of $\text{Si}_{1-x}\text{Ge}_x$ layers in the Frank-Van-der-Merwe growth mode. This applies for a very low Ge content x of the alloy layer, at which lattice strain plays a minor role. The lattice parameter of Ge $a_{\text{Ge}} = 5.646 \text{ \AA}$ is about 4% larger than that of Si $a_{\text{Si}} = 5.431 \text{ \AA}$. However, with increasing Ge content x , the elastic energy $\sim \varepsilon^2 d$ stored in a layer of thickness 'd' increases, with the increase in built-in biaxial strain $\varepsilon = 0.04x$. Thus the elastic energy increases linearly with layer thickness and drives inelastic and elastic strain relaxation. Inelastic strain relaxation takes place by formation and glide of misfit dislocations. The formation, gliding and pinning of dislocations also induces a high density of threading dislocations that intersect the deposited SiGe layers and degrade layer quality. The density of threading dislocations can be reduced by deposition of thick SiGe buffer layers with a graded Ge content [14]. Fig. 1.3 shows the schematic representing the two types of strain relaxation. Strained SiGe layers of increasing thickness on Si tend to relax strain not only by dislocation formation

but also by local elastic relaxation which involve an increasing undulation and roughening [15] of the surface. Such a roughening may be enhanced by local inhomogeneities caused by dislocations, point defects or contaminations. However, even a perfect SiGe layer on Si may roughen due to the two fundamental mechanisms. Homogeneous deposition of a SiGe layer in the step-flow mode on a Si substrate with a small (inevitable) miscut may result in a layer of modulated thickness. Some SiGe material may accumulate at the intrinsic step edges, as mismatch strain can partially relax there. Even at an atomically flat substrate, undulations of a strained layer surface enable elastic strain relaxation.

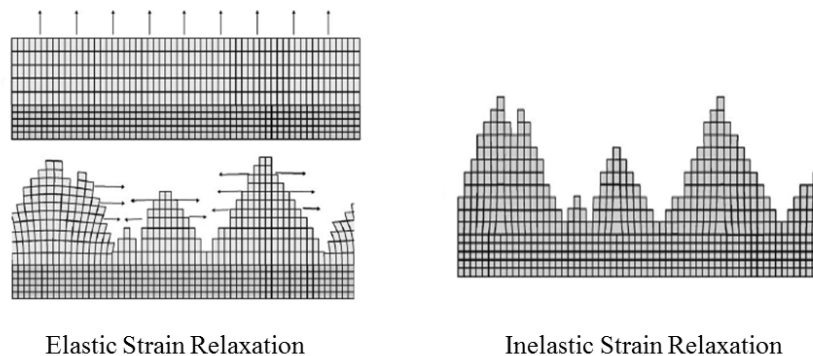


Figure 1.3: Schematic showing the strain relaxation occurring during heteroepitaxy by elastic and inelastic means.

Under conditions of relatively high misfit coherency strain $\varepsilon_{coh} > 2\%$, heteroepitaxial thin films grow via the Stranski-Krastanov (S-K) mode [12], i.e., the first 1-3 monolayers (ML) of film grow as a two dimensional (2D) wetting layer, but subsequent adatoms cluster to form small three dimensional (3D) islands. These islands can retain coherent interfaces with the underlayer, but nonetheless

some portion of the net strain energy is relaxed by the 2D-3D transition. This behavior is governed by the energetics of the strain field and the surface [15], subject to the kinetics of adatom transport that regulate nucleation and evolution of islands, in competition with dislocation introduction [20, 21]. However, in case of dilute $\text{Si}_{1-x}\text{Ge}_x$ alloys (having low Ge concentration) with low misfit strain, the 3D islands form only after a critical thickness is achieved. The atoms at the top of the island are free to relax towards the bulk Ge lattice parameter and the elastic energy released exceeds the increase in surface energy. Apart from this simple approach of growth in SiGe heteroepitaxy, modified S-K growth mode is widely observed. In this, the growth mechanism (kinetics and thermodynamics) is highly influenced by the intermixing of Si and Ge at the interfaces [16].

1.3 Optimization of Growth

As already discussed, SiGe heteroepitaxy follows S-K growth mode. The quality and the type of structure formation in SiGe heteroepitaxy depends on the growth parameters i.e. growth temperature, composition, deposition rate and layer thicknesses. Due to the biaxial compressive strain developed in the pseudomorphic $\text{Si}_{1-x}\text{Ge}_x$ layers, an elastic energy is stored in these layers. The energy density is proportional to the thickness of the layer and leads to the elastic and inelastic strain relaxation. Inelastic strain relaxation takes place by formation and glide of misfit dislocations. It causes a severe limitation of layer parameters for pseudomorphic defect-free heteroepitaxy. The calculated critical thicknesses for disloca-

tion formation depending on Ge content of a SiGe layer on Si(001) are plotted in Fig. 1.4 [17].

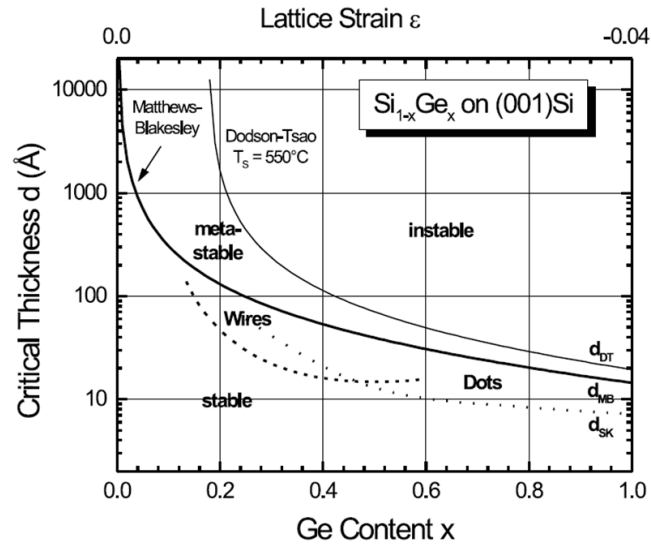


Figure 1.4: Critical thicknesses of smooth strained SiGe layers on (001) Si for relaxation by dislocation formation at high and moderate substrate temperature d_{MB} and d_{DT} . (Ref. [17])

Matthews and Blakesley [18] determined an equilibrium critical thickness d_{MB} for formation of dislocations from the balance of relevant forces. These values are in reasonable agreement with experimental results observed for high growth temperatures $T_G \geq 750^\circ\text{C}$. At lower T_G , kinematic limitations become important as explained by Dodson and Tsao [19]. A certain, (temperature-dependent) amount of excess stress is necessary to induce the gliding of dislocations required for strain relaxation. The resulting curve of critical thickness d_{DT} for a moderate temperature of 550°C is significantly above the equilibrium curve in Fig. 1.4. In between the two curves, there is a range of parameters for metastable strained SiGe layers, which can be deposited without inelastic relaxation at low temper-

ature. During this work, several kind of multilayer structures were grown and their structure was studied by cross-sectional transmission electron microscopy (XTEM). Depending upon the growth conditions, different structures were obtained in the several epitaxial SiGe samples so prepared. Threading dislocations were also observed when either the growth temperature was low and/or the thickness of the Ge layer was higher than the critical thickness for elastic relaxation. Variation in the growth parameters led to the formation of completely pseudomorphic layers when the growth temperature was kept at higher values (750°C) and SiGe alloy layers were grown with Si spacers as the lattice mismatch between SiGe alloy and Si is lower than that between Ge and Si. Following are two examples of multilayer samples with and without dislocations as deposited in our MBE chamber.

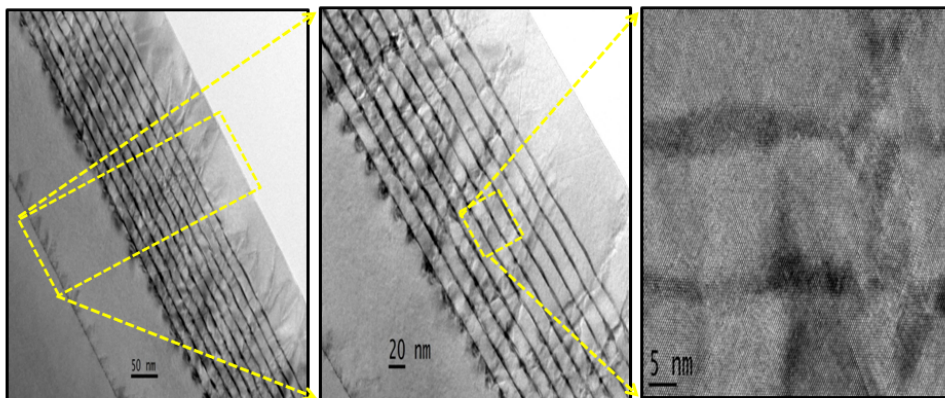


Figure 1.5: XTEM of Si/Ge multilayer sample ($T_G = 550^\circ\text{C}$, Si/Ge:110/40 Å) showing inelastic relaxation.

Fig. 1.5 shows XTEM study of a Si/Ge multilayer sample grown at substrate temperature of 550°C and having layer thicknesses as Si/Ge:110/40 Å. As can be

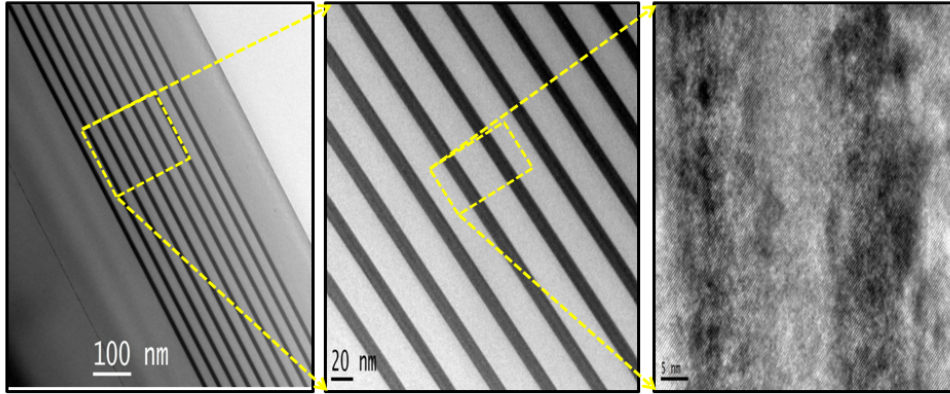


Figure 1.6: XTEM of Si/SiGe alloy multilayer sample ($x=48\%$, $T_G = 750^\circ\text{C}$, Si/SiGe : 175/100 Å) showing completely pseudomorphic layers.

seen from the Fig. 1.4, the Ge layer thickness is higher than the critical thickness for dislocation formation, we observe a 3D islanding taking place in the system and the accumulated strain is relaxed by the formation of threading dislocations. High resolution XTEM images verify the inelastic relaxation occurring in these multilayers by the presence of dislocations. Completely pseudomorphic $\text{Si}_{1-x}\text{Ge}_x/\text{Si}$ epitaxial multilayers can be grown by choosing the growth parameters properly. Fig. 1.6 shows a completely pseudomorphic multilayer system where a $\text{Si}_{0.52}\text{Ge}_{0.48}$ alloy layer having thickness of 100 Å is deposited alternately with Si spacers of 175 Å. This multilayer system was deposited at a substrate temperature of 750°C . The layer thicknesses with the Ge composition in alloy layer fall in region below the critical thickness for dislocation formation as depicted in Fig. 1.4. High resolution XTEM images show a complete pseudomorphic growth.

1.4 General Discussion

Both silicon and germanium occur in nature as crystalline diamond lattice structures, in which each atom is covalently bonded to four neighboring atoms. The diamond structure unit cell consists of two inter-penetrating face-centered cubic unit cells, one of which is displaced along the body diagonal by a quarter of the unit cell lattice parameter relative to the other. Si and Ge are completely miscible and can form any $\text{Si}_{1-x}\text{Ge}_x$ alloy with x varying from 0 to 1. The lattice constant of any $\text{Si}_{1-x}\text{Ge}_x$ alloy (a_{SiGe}) can therefore be described by Vegard's law, according to which, for any germanium composition, x , $a_{\text{Si}_{1-x}\text{Ge}_x}$ is an interpolation between the lattice constants of silicon (a_{Si}) and germanium (a_{Ge}) and can be written as [11]:

$$a_{\text{Si}_{1-x}\text{Ge}_x} = a_{\text{Si}}(1 - x) + a_{\text{Ge}}x + [0.0273(x^2 - 10x)] \quad (1.3)$$

The final term is a correction factor for $\text{Si}_{1-x}\text{Ge}_x$ to account for the slight discrepancy between theoretical and empirically obtained lattice parameters.

The 4% lattice mismatch between the two elements is utilized to fabricate strained (pseudomorphic) layers. Deposition of $\text{Si}_{1-x}\text{Ge}_x$ atoms on a silicon substrate to form a commensurate interface will result in a layer under biaxial compressive strain in the plane of growth due to the larger bulk lattice constant of $\text{Si}_{1-x}\text{Ge}_x$. The interface between the two materials is known as a misfit interface, and the in-plane compression of the $\text{Si}_{1-x}\text{Ge}_x$ layer will be accompanied by an

extension of the lattice in the growth direction, according to the Poisson ratio. Alternatively, the growth of silicon on a substrate of bulk $\text{Si}_{1-x}\text{Ge}_x$ will result in a biaxially tensile strained layer. The in-plane strain ($\varepsilon_{||}$) in the layer due to the lattice mismatch (or misfit) can be expressed in terms of the lattice constants of the layer, $a_{layer} = a_{||}$, and substrate, $a_{substrate}$:

$$\varepsilon_{||} = \frac{a_{||} - a_{substrate}}{a_{substrate}} \quad (1.4)$$

For silicon-germanium strained layers, $\varepsilon_{||}$ varies with germanium composition from zero to 0.04 and will be positive (negative) for compressive (tensile) strain. The lateral compression is compensated by an elongation ε_{\perp} of the SiGe layer leading to a tetragonal distortion of the lattice. This distortion can be found by the elastic theory as: $\varepsilon_{\perp} = -2C_{12}\varepsilon_{||}/C_{11}$ where C_{ij} are the elastic constants. The introduction of strain into silicon has a profound effect on its electrical properties, which are highly desirable for the manufacture of future electronic devices.

If the layer thickness exceeds the critical thickness, the strain relaxation takes place by plastic (defect) accommodation instead of elastic mismatch compensation. Plastic relaxation in the form of misfit dislocations are created at the interfaces or threading dislocations so created can pass through the whole layer leading to the relaxation of stored elastic energy.

1.5 Quantum Dot Superlattice: Review

Stacked islands or undulated superlattices can be obtained by depositing alternating layers of strained islands and thin substrate material spacers in near-equilibrium growth conditions. This is a good means to increase the total volume of 3D nanostructures without incurring strain relaxation via plastic deformation (i.e. injection of misfit dislocations). In general, island superlattices exhibit a strong vertical correlation.

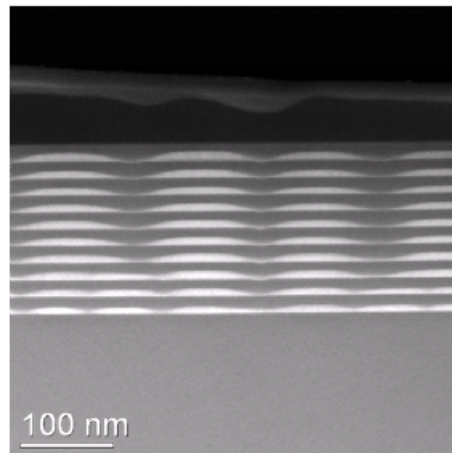


Figure 1.7: HAADF STEM cross section images of island superlattices grown by MBE ($\text{Si}_{0.54}\text{Ge}_{0.46}/\text{Si}$ superlattice with 3.4 nm thick alloy layers and 13.7 nm Si spacers, grown at 625°C) (Ref. [24]).

The micrograph (Fig.1.7) obtained from an MBE grown structure shows extremely regular undulations forming at the alloy to Si interfaces. In the SiGe system, the vertical alignment of the islands arises from a partial elastic relaxation of the $\text{Si}_{1-x}\text{Ge}_x$ lattice at the apex of the island, which causes tensile strain in the Si lattice above the $\text{Si}_{1-x}\text{Ge}_x$ island. This locally reduces the misfit strain

and makes it an energetically favorable nucleation site for a $\text{Si}_{1-x}\text{Ge}_x$ island in the next alloy layer. This vertical alignment may be lost if the Si spacer layer thickness is increased to the extent that negligible strain exists at the surface. The critical spacer thickness depends on the growth methods and conditions [22] but, in general, strong vertical alignment is achieved for spacers less than 25 nm thick, while little alignment is preserved beyond 100 nm. The degree of vertical ordering has been correlated with a reduction of the thickness of the WL in stacked islands, which is also consistent with strain propagation in the Si spacers. The coarsening and coalescence of islands in the upper layers of island superlattices is a self-organization process that may be explained in the framework of continuum elasticity theory [23]. The strain field overlap of two closely spaced small islands will result in the nucleation of a larger island in the next alloy layer rather than the replication of the small islands, while for larger islands the strain field will not expand beyond the lateral size of the islands and their size will be self-limited. Finally, some oblique stacking of islands is sometimes observed and has been explained by the interplay of surface stress and the development of Si surface depressions (step-bunching) in the vicinity of large islands [17]. No well ordered staggered stacking has been observed in the SiGe system on (001) Si, because elastic anisotropy favors vertical alignment.

Self-assembly offers an attractive route to the fabrication of quantum dot arrays, especially since the islands can be unexpectedly uniform in size. A fascinating feature of such structures is that the dots (i.e., buried islands) in successive

layers are spatially correlated. Tersoff et al [23] gave a theoretical model for the self assembly of Ge/Si islands. At the surface, new islands tend to nucleate directly above buried islands. This spatial bias arises from the strain at the surface due to buried strained islands. The island sizes and spacings actually become more regular with each successive layer. This phenomenon provides a mechanism for obtaining the uniform island sizes required in electronic devices. They showed that the size and spacing of islands can be directly controlled via the thickness of the layers.

Liu et al [22] have shown an evidence of the breakdown of vertical correlation and also the growth mode changes before and after the reach of effective thickness of superlattices. In each period, the strain is relaxed by the formation of quantum dots after reaching the critical thickness. However, for the quantum dot superlattice also, a critical thickness exists after which the dislocations are induced in the superlattice. To understand critical thickness for quantum dot superlattice, the equivalent Ge content should be determined. From both theoretical and experimental results of the critical thickness of SiGe alloy and SiGe/Si superlattice on Si [27,28], it is concluded that the nominal Ge thickness rather than wetting layer thickness only contribute on the strain accumulation and determine the film critical thickness, even though misfit strain in each layer is partially relaxed by the formation of the dots.

Chapter 2

Experimental Techniques

2.1 Molecular Beam Epitaxy

The first successful use of a molecular beam apparatus for the crystallization and investigation of GaAs epilayers by Cho and Arthur dates back to the late 1960s. Since then, MBE has evolved into one of the most widely used techniques for producing epitaxial layers of metals, insulators and superconductors as well, both at the research and the industrial production level. The principle underlying MBE growth is relatively simple: it consists essentially of atoms or clusters of atoms, produced by heating up a solid source which then migrate in a UHV environment and impinge on a hot substrate surface, where they can diffuse and eventually incorporate into the growing film. In spite of simple concept, a lot of technological strength is required to produce MBE systems that yield the desired quality in terms of material purity, uniformity, high vacuum and interface control.

2.1.1 MBE Basics

Molecular beam epitaxy is a technique for epitaxial growth via the interaction of one or several molecular or atomic beams that occurs on a surface of a heated crystalline substrate under ultrahigh-vacuum condition [30–32]. Source materials are placed in a crucible inside the evaporation cells (known as Knudsen cells), whose shape and dimensions ensure the required angular distribution of atoms in the beam. A manipulator with substrate holder is used to ensure the required position of the substrate relative to the cells and to heat it to the required temperature. The homogeneity of the resulting films can be improved by rotating the substrate.

For typical distances between the sources and the substrate, the molecular beam condition is ensured (i.e., the free path of the particle is larger than the geometrical size of the chamber). The MBE systems are provided with the means to reach and maintain ultrahigh vacuum ($\sim 10^{-11}$ Torr) and operation is usually oil-free. One of the reasons why the MBE system must be oil-free is the need to ensure that the substrate is atomically clean before growth. On the other hand, a low level of background doping and control over the properties of the grown material can be ensured only if uncontrolled fluxes reaching the substrate surface are as weak as possible. An ultrahigh vacuum is essential for this purpose, but it is not a sufficient condition. Firstly, any vacuum represents an equilibrium between the rate of gas evolution and the rate of pumping, so that construction and crucible materials with lowest possible rate of gas evolution are used. Secondly, it is important to ensure cryogenic screening around the substrate in such a way

that it will minimize the stray fluxes of atoms and molecules from the walls of the chamber, which are present at room temperature and can arise from the heated components of the apparatus. Thirdly, only ultra-pure materials can be used as source materials in MBE.

One advantage of MBE is the intrinsic feasibility of controlling the profile of the composition and doping of a growing structure at monolayer level. This feasibility is ensured by a molecular beam regime during growth that excludes any interaction between atoms or molecules in the beam and between different beams, in combination with a low growth rate. An abrupt change in composition and/or degree and nature of doping are achieved by opening or closing the relevant fluxes using the shutters with which each cell is equipped. The operation time of a shutter (< 0.1 sec) is usually considerably less than the time needed to grow one monolayer (typically 1-5 sec). Variation of cell temperatures and, consequently, the intensities of molecular fluxes, and the corresponding variation of the growth rate provide a way of establishing any specified composition profile in the film. Preliminary preparation of an atomically clean, defect-free substrate surface is exceptionally important in this technology.

2.1.2 Outline of the MBE system

A schematic drawing of a generic MBE system is presented in Fig. 2.1. Some basic components can be identified: The vacuum system consists of a growth chamber, UHV-connected to a preparation chamber, where substrates are degassed prior

to growth, and a load-lock module for transfer to and from air (not shown). All the components of the growth chamber must be able to resist bake-out temperatures of up to 200°C for extended periods of time, which are necessary to minimize out-gassing from the internal walls. The pumping system must be able to efficiently reduce residual impurities to a minimum. In practice, base pressure is reduced to the 10^{-11} - 10^{-12} Torr range. The pumping system usually consists of ion pumps, with auxiliary Ti-sublimation and cryogenic pumps.

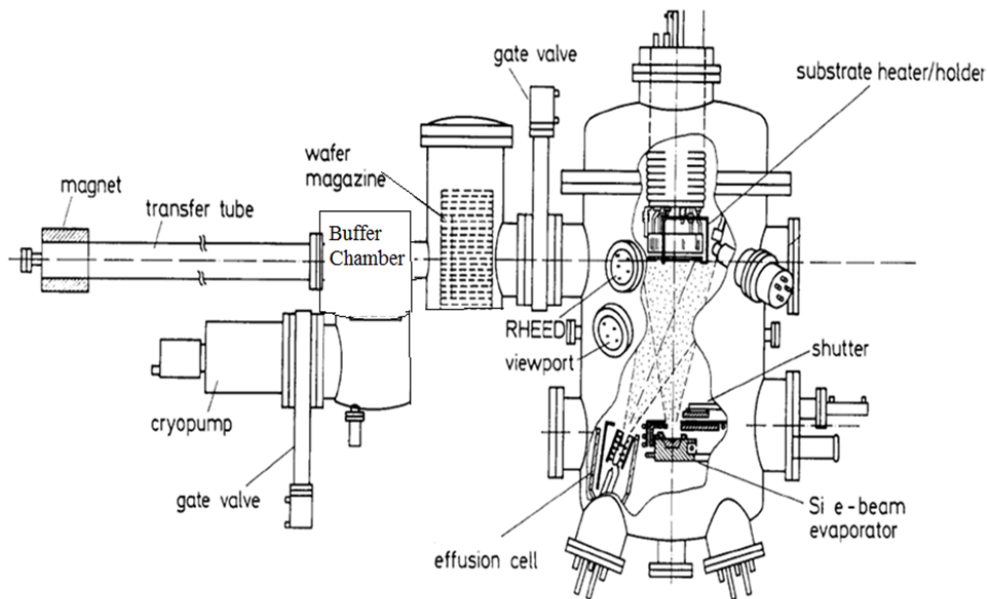


Figure 2.1: Schematic diagram of a Molecular Beam Epitaxy setup.

Liquid N₂ cryopanels surround internally both the main chamber wall and the source flange. Since MBE is a cold wall technique, cryopanels prevent re-evaporation from parts other than the hot cells. Also they provide thermal isolation among the different cells. Effusion cells are the key components of an MBE

system, because they must provide excellent flux stability and uniformity, and material purity. Therefore a careful choice of elements, materials and geometry is required. The cells are placed on a source flange, and are co-focused on the substrate heater, to optimize flux uniformity. The temperature control is of the order of $\pm 1^\circ\text{C}$ at 1000°C . A schematic drawing of a typical effusion cell is shown in Fig. 2.2, and some of the main features are indicated. The crucible (1) is usually made of pyrolitic boron nitride, which can stand temperatures of up to $\sim 1300^\circ\text{C}$ without appreciable degassing. Its shape can be cylindrical or conical with different tapering angles, depending on the material to be evaporated. Its size depends on the material to be evaporated as well, and has to be big enough to provide several months of operation before the depletion of the material. Heating is provided by a Ta filament (2), while multiple Ta foils provide heat shielding (3). A thermocouple (4) is located in an appropriate position in order to measure the material temperature; temperature regulation is provided by high-precision PID regulators. A mechanical or pneumatic shutter, usually made of Tantalum or Molybdenum, is placed in front of the cell to trigger the flux. The shutters operate much faster than the growth rate (typically 0.1 s), and are computer-controlled to provide reproducible growth cycles, especially for superlattices. Besides, these are designed not to outgas when heated from the cells, and not to constitute an appreciable heat shield, giving rise to flux transients after opening. The substrate manipulator is capable of continuous azimuthal rotation (CAR) around its axis to improve uniformity across the wafer. The heater behind the sample is designed to



Figure 2.2: A typical Effusion Cell.

maximize temperature uniformity and minimize power consumption and impurity outgassing. On the manipulator a Mo or Ta substrate holder is mounted containing the wafer on which deposition has to be done.

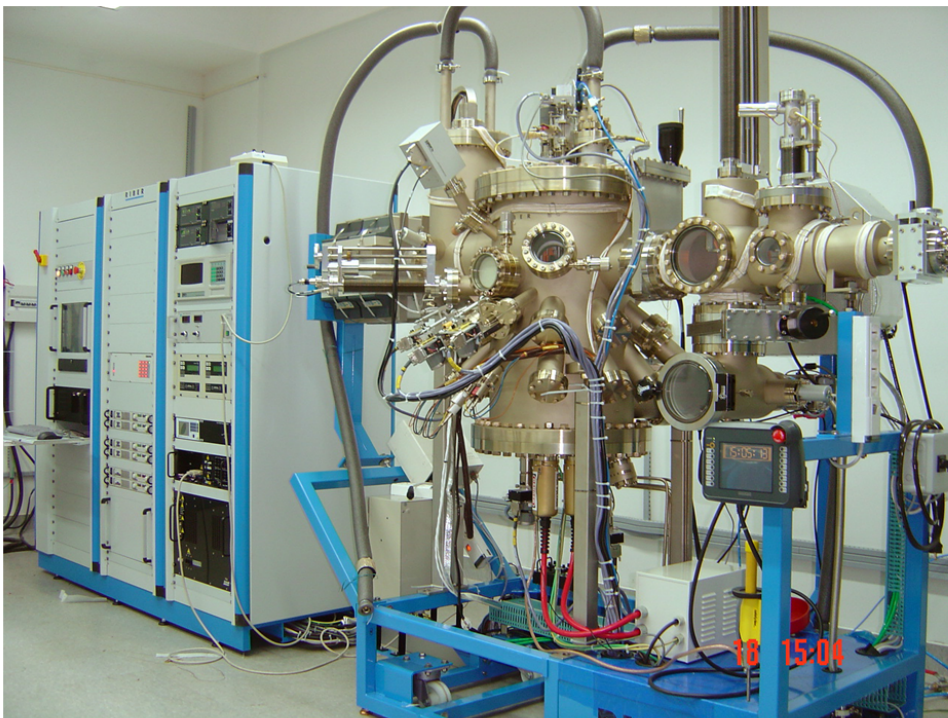


Figure 2.3: Molecular Beam Epitaxy setup present at Saha Institute of Nuclear Physics.

All the SiGe samples are prepared by the solid source Riber Compact21 MBE system (shown in Fig. 2.3) present at Saha Institute of Nuclear Physics. It consists

of three chambers viz. load-locked sample-loading chamber (LC), preparation chamber (PC) and growth chamber (GC). While a high vacuum ($\sim 10^{-9}$ Torr) is maintained in LC and PC using turbo and ion pumps respectively, an ultra high vacuum ($\sim 10^{-11}$ Torr) is maintained in GC using titanium sublimation and ion pumps. GC is provided with a residual gas analyzer (RGA) (Hiden Analytical, UK) for the detection of residual impurities. For the insertion of the substrate wafers (chemically cleaned beforehand) in LC, the same are put in metal (Mo) cassettes prior to loading. These are then transferred to PC with the help of sample lift and transfer rod, where the wafers are degassed by radiative heating. The maximum temperature of this degas chamber (PC) is 820°C . After this, the wafers are transferred to GC, where they are further heated up to a maximum temperature of 1100°C for degassing and oxide removal. This procedure allows making ultra-clean reconstructed surfaces for further studies. Reflection high energy electron diffraction (RHEED) system (STAIB instruments) present in GC, allows in situ monitoring of the surface reconstruction process as well as the growth process. The four effusion cells present in GC, of which two are of high temperature (2000°C) and two are of low temperature (1450°C), are used for the evaporation of materials to be deposited. Germanium and silicon, used for Si/Ge multilayer deposition in the present work, are evaporated using low temperature effusion cell and electron gun (e-gun) evaporator, respectively. The deposition of Ge and Si is controlled by main shutters attached to the sample manipulator. The deposition rate of Si is maintained with the help of a Quartz Crystal Microbalance (Inficon

XTC/2 Deposition Controller), by controlling power of the electron beam. The Ge deposition rate is determined by controlling effusion cell temperature. Substrate is rotated azimuthally during growth so as to ensure better homogeneity of the films. During deposition, liquid nitrogen is continuously circulated around GC for system cooling and maintaining ultra high vacuum. The deposition process is fully software controlled.

Chemical Cleaning

Si(001) wafers, used as substrates, are chemically cleaned using two-step RCA process. In the first step, Si substrates are lowered into a boiling mixture of HCl (30%), H₂O₂ (31%) and deionized water (DI-H₂O) in the ratio 1:1:5 for 15 min. The wafers are then rinsed in a DI-H₂O bath for a further 15 min. In the second step, the substrates are immersed in a boiling mixture of NH₃ (25%), H₂O₂ (31%) and DI-H₂O in parts of 1:1:5 for 15 min. After this, the wafers are rinsed in the DI-H₂O bath for 15 min to wash away residual ions of the acid. Hydrofluoric acid solution (HF-Dip) was used to remove the native oxide from the wafer surface immediately before they are put into the load-lock chamber. HF-Dip was a mixture of HF (40%) and DI-H₂O with ratio 1:10. In order to desorb the oxide, the substrate was first heated up to 800°C for 30 min in the preparation chamber, which was followed by a further heating at 1100°C for 5min in the growth chamber. Surface cleanliness was checked by in-situ RHEED.

2.2 X-Ray Scattering Facility

X-rays were discovered in 1895 by the German physicist Roentgen and were so named because their nature was unknown at the time. It was not until 1912 that the exact nature of x-rays was established. In that year the phenomenon of x-ray diffraction by crystals was discovered, and this discovery simultaneously proved the wave nature of x-rays and provided a new method for investigating the fine structure of matter. X-ray diffraction is extremely useful technique as it can indirectly reveal details of internal structure of the order of 10^{-8} cm in size. X-rays are basically electromagnetic radiation of exactly the same nature as light but of very much shorter wavelength. The unit of measurement in the x-ray region is the angstrom (\AA), ($=10^{-8}$ cm), and x-rays used in diffraction have wavelengths lying approximately in the range 0.5-2.5 \AA , whereas the wavelength of visible light is of the order of 6000 \AA . X-rays therefore occupy the region between gamma and ultraviolet rays in the complete electromagnetic spectrum. Till the mid 1970, X-ray tubes were only used as X-ray sources in which X-rays are generated by bombarding high energy electrons on a suitable target material like Copper (Cu), Molybdenum (Mo) etc. In mid 1970s it was realized that the synchrotron radiation emitted from charged particles circulating in storage rings constructed for high energy nuclear physics experiments was potentially a much more intense and versatile source of x-rays. Indeed synchrotrons have proved to be such vastly better source that many storage rings have been constructed around the world dedicated solely to the production of X-rays.

2.2.1 Laboratory Source

After the discovery of x-rays in 1895, the first X-ray tube to be used as a standard x-ray source was developed by W. D. Coolidge in 1912. A typical x-ray tube consists of a filament or cathode made of Tungsten to produce electrons which are focused and accelerated by applying a high voltage between cathode and anode. The anode is generally coated with a metal like Copper (Cu), Molybdenum (Mo), etc., depending upon the requirement of wavelength of x-rays to be generated. The point where the electron beam strikes the anode is called the focal spot. Most of the kinetic energy of the electrons after bombardment with anode is converted to heat and only about 1% of the energy is converted into x-ray. The heat generated during the bombardment is dissipated by keeping the anode in contact with circulating coolant like cold water. This generation of heat at anode and efficiency of cooling restrict the power of the x-ray tube around 1 kW. A further improvement in the power was achieved when a rotating anode was used instead of fixed anode. A rotating anode can dissipate heat over a larger volume compared to fixed one. The technical difficulties like problem of maintaining high vacuum seal on the rotating shaft of anode took some time to settle and only after 1960's rotating anode x-ray sources could be available on commercial basis.

X-rays produced from bombardment of electrons on anode consist of two distinct components depending the nature interaction of electrons with anode material. There is a continuous part due to the electrons being decelerated, and eventually stopped in the metal. This is known as bremsstrahlung radiation and has

maximum energy that corresponds to the high voltage applied to the tube. During collision of a high energy electron with an atom of the anode, an electron from inner shells of the atom can be knocked off creating a vacancy. The spontaneous relaxation of an electron from an outer shell into the vacancy produces an x-ray photon with a characteristic energy equal to the difference between the energies of the shells. These characteristic energy peaks superimposed on continuous bremsstrahlung give the total spectrum of x-rays emitted from that particular anode material. The experiments with monochromatic beam utilize the K-lines of the anode material which is several orders of magnitude more intense than bremsstrahlung spectrum.

2.2.2 Synchrotron Source

Fig. 2.4 shows a schematic of the key components of a typical synchrotron source. The details will vary according to the particular requirements, but many components will be found in one form or the other. Synchrotron light starts with an electron gun. A heated element or cathode produces free electrons which are pulled through a hole in the end of the gun by a powerful electric field which produces an electron stream. The electron stream is fed into a linear accelerator or linac. Here, high energy microwaves and radio waves chop the stream into bunches or pulses. When they exit the linac, the electrons are travelling at 99.99986% of the speed of light and carry about 300 million electron. The linac feeds into the booster ring which uses magnetic fields to force electrons to travel in a circle. The

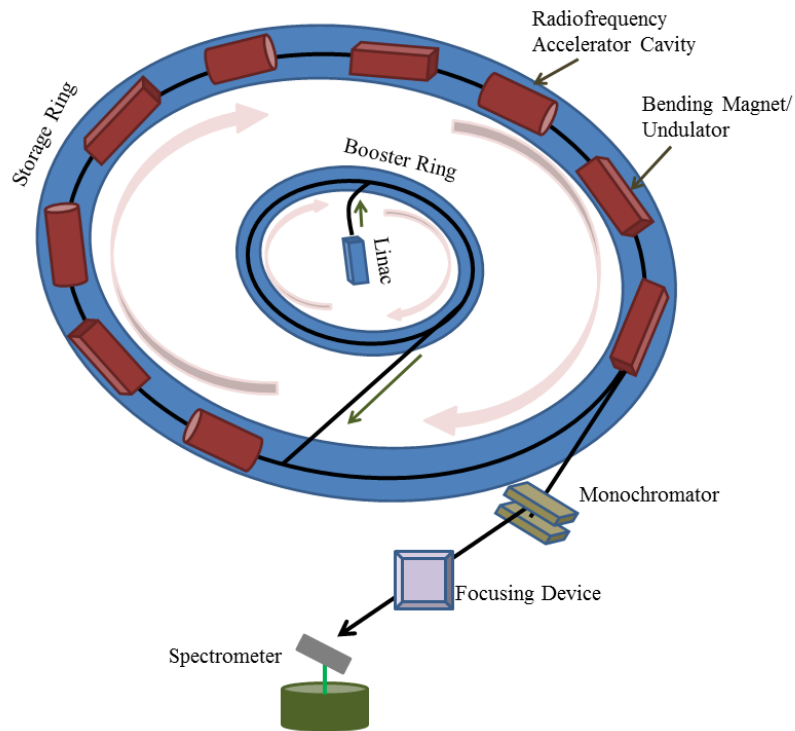


Figure 2.4: Schematic of a typical Synchrotron source

booster ring ramps up the energy in the electron stream to the order of gigaelectron volts (GeV). This is enough to produce synchrotron light in the infrared to hard x-ray range. The booster ring feeds electrons into the storage ring, a many-sided donut-shaped tube. The tube is maintained under vacuum, as free as possible of air or other stray atoms that could deflect the electron beam. Bending magnets or insertion devices such as undulators are used to finally produce the Synchrotron light. Bending magnets deflect the electron beam to produce the radiation. The main function of bending magnets is to bend the electrons into their racetrack orbit. However, as the electrons are deflected from their straight path when passing through these magnets, they emit a spray of x-rays tangentially to the plane of the electron beam. The synchrotron light from a bending magnet covers a wide and

continuous spectrum, from microwaves to hard x-rays, and it is much less focused, or brilliant, than the fine beam of x-rays from an insertion device. Undulators are magnetic structures, made up of a complex array of small magnets which force the electrons to follow an undulating, or wavy, trajectory. The radiation emitted at each consecutive bend overlaps and interferes with that from other bends. This generates a much more focused, or brilliant, beam of radiation than that generated by a single magnet. Also, the photons emitted are concentrated at certain energies (called the fundamental and harmonics). The gap between the rows of magnets can be changed to fine-tune the wavelength of the x-rays in the beam. The second key component is the monochromator, as in many applications it is required to work at a particular average wavelength. It may also be desirable to choose the wavelength bandwidth, and monochromators made from perfect crystals through to multilayers allow for a considerable variation in this parameter. After this, the monochromatic beam is focussed down to small sizes by using devices such as x-ray mirrors and refractive Fresnel lenses. Finally, x-rays are delivered on the sample on which experiments are performed.

The quality of the Synchrotron x-ray beam can be parameterized depending upon several aspects. These aspects can be combined into single quantity, called the 'brilliance'. First of all, there is the number of photons emitted per second, then collimation which defines how much beam diverges as it propagates. Collimation is in milliradians both in horizontal and vertical directions. Other important aspect is the source area which is given in mm^2 . Lastly, important factor is

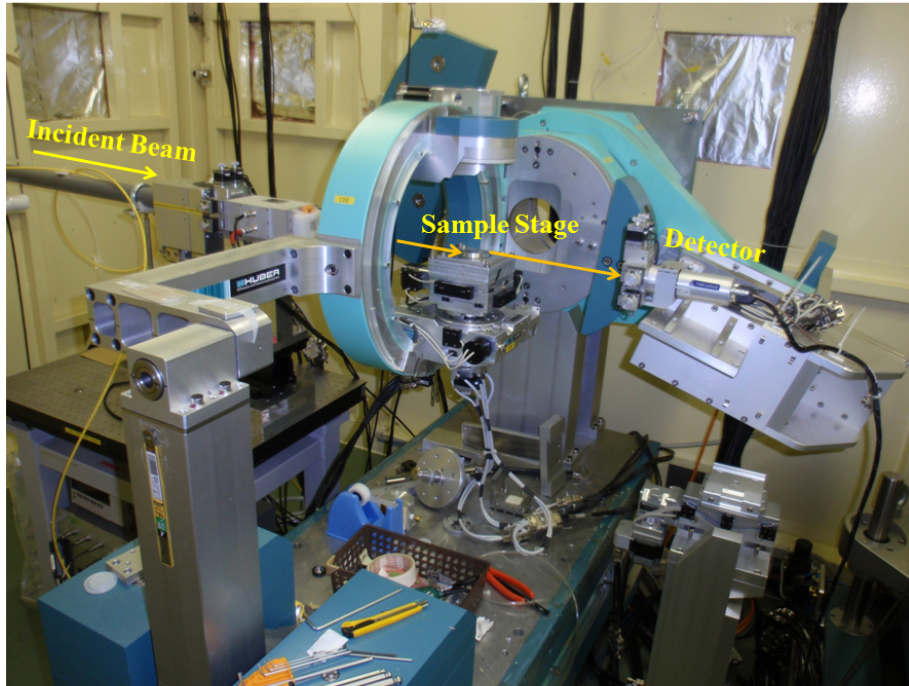


Figure 2.5: Diffractometer at Indian Beamline, Photon Factory, Japan.

the spectral distribution. Some sources produce very smooth spectra, others have peaks at certain photon energies. The convention is therefore to define the photon energy range as a fixed relative energy band-width (BW), which is chosen to be 0.1%. Altogether, the figure-of-merit of the source is given as:

$$Brilliance = \frac{Photons/second}{(mrad)^2(mm^2\ source\ area)(0.1\%BW)} \quad (2.1)$$

The brilliance is a function of the photon energy. The maximum brilliance from third generation undulators is approximately 10 orders of magnitude higher than that from a rotating anode at the K_α line. In this thesis work, most of our x-ray experiments were performed using x-ray synchrotron sources at Indian Beam-

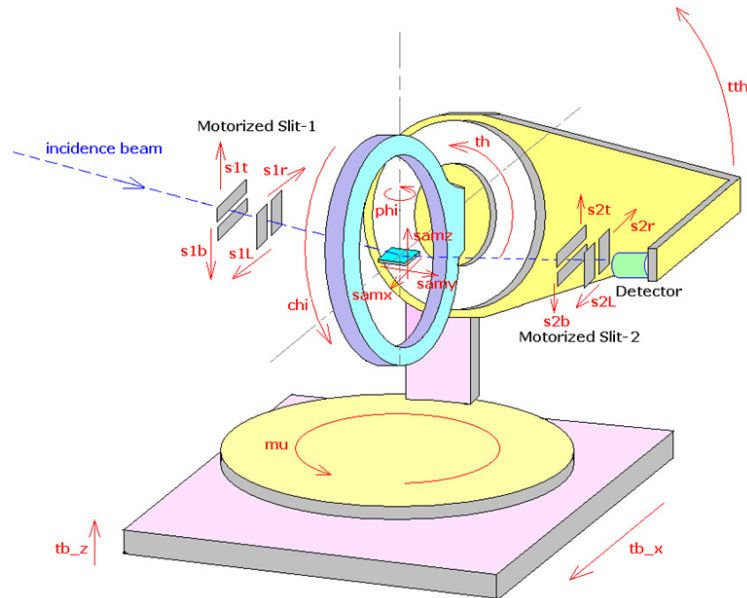


Figure 2.6: Line diagram of the diffractometer at Indian Beamline, Photon Factory, Japan.

line, Photon Factory, Japan and P08 beamline of Petra III, Germany.

While performing on X-ray scattering measurements, from the experimental point of view, it is extremely important to have a precise machinery in order to have an accurate control over the incidence and exit angles. Also, x-ray sources are required which have low angular divergence. Today both of these requirements are met easily due to the availability of very high precision diffractometers and the Synchrotron radiation sources. Fig. 2.5 shows a four-circle diffractometer (in grazing incidence and exit angle geometry) installed at Indian beamline, Photon Factory, Japan. The path of incident x-ray beam, exit beam into detector and sample stage are indicated. This versatile diffractometer has four circles of rotation so as to provide several degrees of freedom to perform GIXS experiments.

Fig. 2.6 shows the line diagram of the said diffractometer. It consists of a set of vertical and horizontal motorized slits present both in the path of the incident x-ray beam and in front of the detector, so as provide a defined beam profile and high signal to noise ratio respectively.

2.3 Transmission Electron Microscopy

The structures formed in the Si/Ge heteroepitaxy have a size of the order of few hundred nanometers. To understand the structural properties at nanometer scale, Transmission Electron Microscopy (TEM) comes across as a very powerful and versatile instrument. It offers variety of information obtained from different modes such as high resolution lattice imaging, scanning tunneling electron microscopy-energy dispersive x-ray spectroscopy (STEM-EDX), high angle annular dark field (HAADF) imaging and selected area electron diffraction (SAED). Fig. 2.7 is a schematic showing the formation of high resolution TEM image and SAED pattern in transmission electron microscope.

The first TEM was built by two German scientists, M. Knoll and E. Ruska, in 1932. The transmission electron microscope (TEM) [33] operates on the same basic principles as the light microscope but uses electrons instead of light. TEMs use electrons as ‘light source’ and their much lower wavelength makes it possible to get a resolution a thousand times better than with a light microscope. A ‘light source’ at the top of the microscope emits the electrons that travel through vacuum in the column of the microscope. Instead of glass lenses focusing the light in the

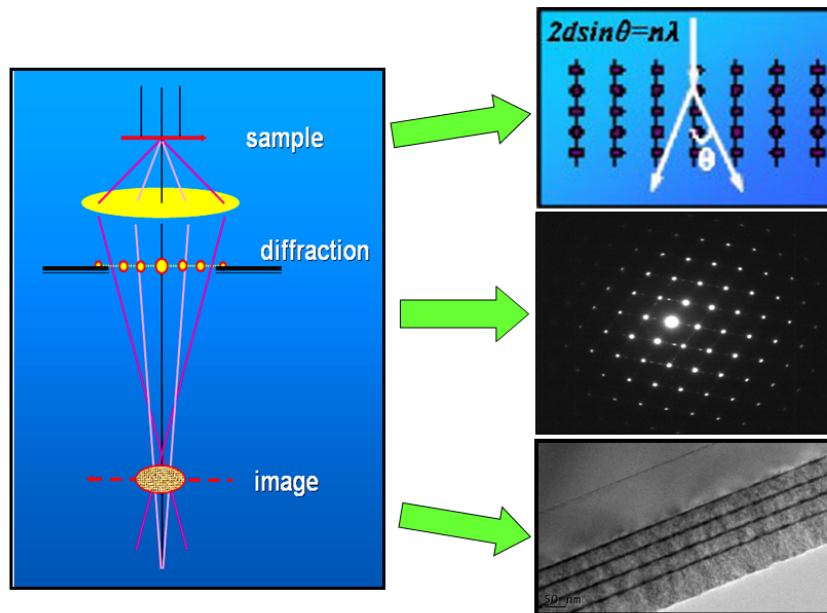


Figure 2.7: Schematic showing formation of HRTEM image and SAED pattern in TEM.

light microscope, the TEM uses electromagnetic lenses to focus the electrons into a very thin beam. The electron beam then travels through the specimen. Depending on the density of the material present, some of the electrons are scattered and disappear from the beam. At the bottom of the microscope the unscattered electrons hit a fluorescent screen or CCD camera, which gives rise to a 'shadow image' of the specimen with its different parts displayed in varied darkness according to their density. The image can be studied directly by the operator or photographed with a camera. In a TEM, a thin crystalline specimen is subjected to a parallel beam of high-energy electrons. As TEM specimens are typically 100 nm thick, and the electrons typically have an energy of 100-400 kiloelectron volts, the elec-

trons pass through the sample easily. During transmission, the electrons interact with the specimen, giving rise to signals containing information about the internal structure and chemistry of the specimen. Electron diffraction patterns and lattice images are two forms of data which give an insight of crystallographic information in TEM. Lattice images are interference patterns between the direct beam and diffracted beams, viewed in direct space, and are obtained by high-resolution TEM (HRTEM) imaging. In the images, the spacing of a set of fringes represents the lattice spacing. For direct information of defect structure on the atomic scale, a HRTEM is particularly useful.

A STEM is in principle very similar to the more commonly known scanning electron microscope (SEM) in that electron optics are used before the specimen to focus an electron beam to form an illuminating spot, or probe, that is scanned over the specimen in a raster fashion. Various signals produced by the scattering of the electrons can be detected and displayed as a function of the illuminating probe position. Since there is very little scattering of the electrons in a thin sample, little beam spreading occurs and the spatial resolution is mainly controlled by the illuminating probe size. Energy dispersive x-ray spectroscopy (EDX) is useful in determining the chemical composition of the materials in the specimen. High angle annular dark-field (HAADF) imaging [82] refers to the use of a particular detector geometry in STEM. A geometrically large annular detector is placed in the optical far field beyond the specimen. The total intensity detected over the whole detector is recorded and displayed as a function of the position of the illu-

minating probe. Since the detector only receives a signal when the specimen is present, the vacuum appears dark. For the heavier atom, the scattering intensity is higher, which leads to atomic number (Z) contrast in the image. In selected area electron diffraction pattern (SAED), the sample is illuminated with a parallel electron beam to ensure the focusing of the transmitted and diffracted beam onto the back focal plane of the objective lens. A specific area of the sample is selected by a SAED aperture that is in an image plane conjugate with the sample in the electron optic system of the TEM. A few hundred nanometers is therefore the typical lateral size of the region sampled by SAED in TEM. In this case, electrons are treated as wave-like, rather than particle-like. Because the wavelength of high-energy electrons is a fraction of a nanometer, and the spacings between atoms in a solid is only slightly larger, the atoms act as a diffraction grating to the electrons, which are diffracted. That is, some fraction of them will be scattered to particular angles, determined by the crystal structure of the sample, while others continue to pass through the sample without deflection. As a result, the image on the screen of the TEM will be a series of spots-the selected area diffraction pattern (SADP), each spot corresponding to a satisfied diffraction condition of the sample's crystal structure. If the sample is tilted, the same crystal will stay under illumination, but different diffraction conditions will be activated, and different diffraction spots will appear or disappear. Fig. 2.7 shows the formation of HRTEM image and SAED pattern in TEM.

Sample preparation for Cross-sectional TEM

Sample preparation is the most crucial part of the TEM characterization. For the electrons to transmit through the sample, it has to be thinned down to the electron transparency (<100 nm) for conventional TEM and even lesser (<10 nm) for HRTEM. To study the interfaces or the bulk of the sample, cross-sectional transmission electron microscopy (XTEM) measurements are required, which need rigorous sample preparation. Step by step procedure for XTEM sample preparation is shown in Fig. 2.8 and 2.9.

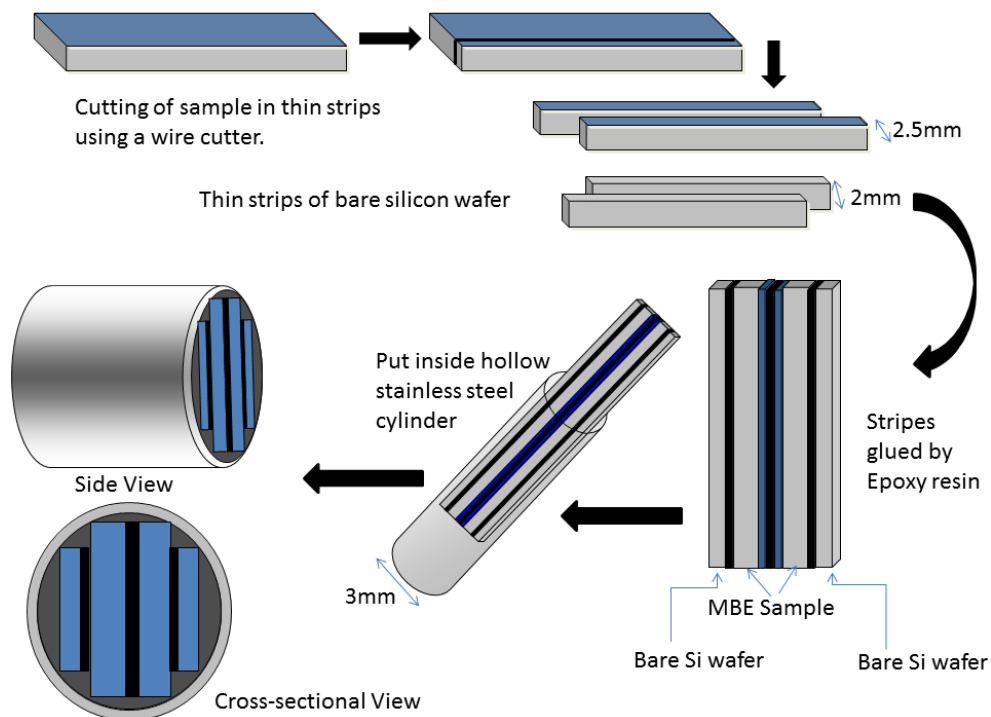


Figure 2.8: Step flow of XTEM sample preparation method.

The MBE sample is first of all cut into two thin stripes of around 2.5 mm thickness using a fine wire cutter. Also, two thin stripes (2 mm) of Si wafer are

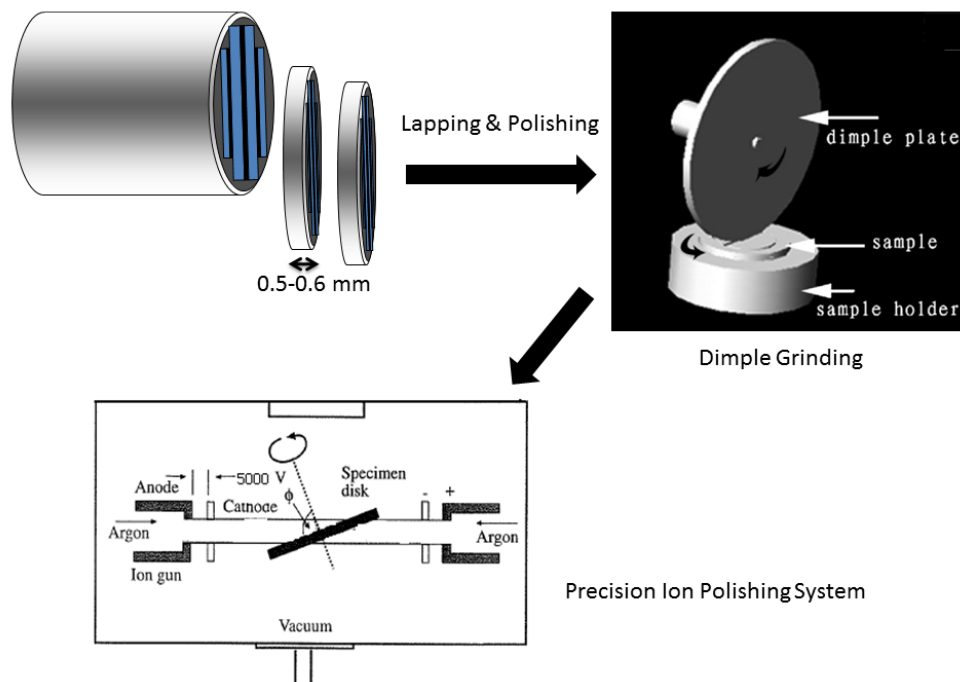


Figure 2.9: Step flow of XTEM sample preparation method continued after steps in Figure 2.8.

also cut which are used as dummy. These four stripes are then glued to each other using the epoxy-resin such that the deposited sides of the sample face each other as shown in the schematic [Fig. 2.8]. Now, the glued stripes are put inside a stainless steel hollow tube having inner and outer diameter of 2.5 and 3 mm respectively. The vacant space inside the tube is filled by the epoxy resin. The tube is then cut into thin discs by the wire cutter. These thin discs are then further thinned to $100\ \mu\text{m}$ using lapping and polishing method. In this, several emery papers are used in a particular sequence and the discs are rotated over them for thinning. Now, the sample is put inside the Dimple Grinder where the sample is thinned from the center to about $30\text{-}40\ \mu\text{m}$. At last, sample is put inside the Precision ion

polishing system (PIPS) whose schematic is shown in Fig. 2.9. In this, the sample is sputtered by 5kV Argon gun from top and bottom with only one gun working at a time. Thus, a tiny hole is formed at the center of sample making the region in its vicinity to be electron transparent (~ 100 nm). Finally, the sample becomes ready to be probed inside the TEM system. The Transmission electron microscopy (TEM) investigations in this thesis work were carried out using FEI, TECNAI G2 F30, S-TWIN microscope operating at 300 kV equipped with a GATAN Orius CCD camera. High-angle annular dark field (HAADF) scanning transmission electron microscopy (STEM) is employed here using the same microscope, which is equipped with a scanning unit and a HAADF detector from Fischione (Model 3000). This TEM facility is installed in Saha Institute of Nuclear Physics.

2.4 Atomic Force Microscopy

The advent of Scanning Probe Microscopes and especially of the Atomic Force Microscope (AFM) has opened new perspectives in the field of microscopy. AFM is a very high-resolution type of scanning probe microscope having nanometer order of resolution which is more than 1000 times better than the optical diffraction limit. The Atomic Force Microscope was developed mainly to overcome a basic drawback with STM - that it can only image conducting or semiconducting surfaces. The AFM, however, has the advantage of imaging almost any type of surface, including polymers, ceramics, composites, glass, and biological samples.

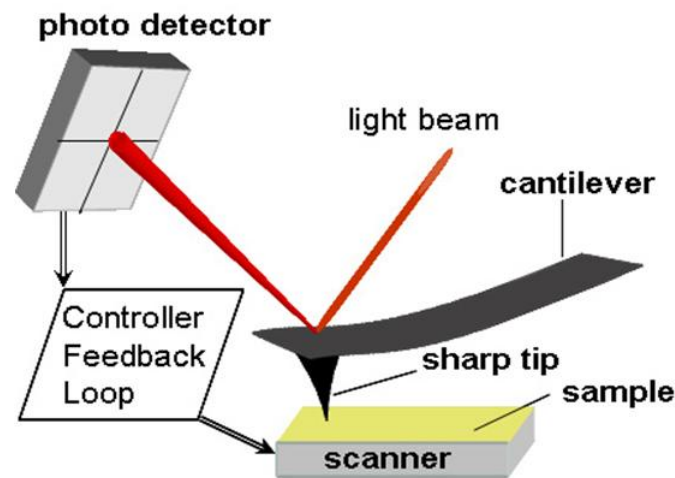


Figure 2.10: Schematic illustration of AFM.

Basic Principles

In AFM a sharp tip mounted on a cantilever is allowed to scan over a sample surface and deflection of the tip due to its interaction with the sample surface atoms is monitored. Schematic of AFM functioning is shown in Fig. 2.10. Under normal working conditions the interaction forces between the tip and sample atoms bend the cantilever following Hooke's law. The cantilever deflection is detected by an 'optical lever' principle and converted into an electrical signal to produce the images. In optical lever method, a laser beam reflected from the backside of the cantilever is made incident on a Position Sensitive Photo Detector (PSPD). As the cantilever deflects, the angle of reflected beam changes and the spot falls on a different part of the detector. Generally the detector is made of four quadrants and the signals from the four quadrants are compared to calculate the position of the laser spot. The vertical deflection of the cantilever can be calculated by comparing the signal from the 'top' and 'bottom' halves of the detector. The lateral twisting

of the cantilever can also be calculated by comparing the 'left' and 'right' halve signals from the detector. This detection system measures the cantilever deflection with sub-Angstrom sensitivity. The spring constant of the cantilever should be small enough to allow detection of small forces and its resonant frequency should be high to minimize sensitivity to mechanical vibration. The scanning i.e tip or sample movement is performed by an extremely precise positioning device made from piezo-electric ceramics, most often in the form of a tube scanner. The scanner is capable of sub-Angstrom resolution in X, Y and Z-directions. To control the relative position of the tip with respect to the sample accurately, good vibration isolation of the microscope has to be ensured. The AFM tips and cantilevers are microfabricated from Si or Si₃N₄. Typical tip radius is from a few to 10 s of nm.

In AFM, the force $F(r)$ which acts between the tip and sample is used as the imaging signal. For two electrically neutral and non-magnetic bodies held at a distance r of the order of several nanometers, the Van-der-Waals forces usually dominate the interaction between them. The force can be derived from the Lenard-Jones potential and its distance dependence can be given as

$$F(r) \propto \left(\frac{1}{r^{13}} - \frac{1}{r^7} \right) \quad (2.2)$$

The variation of interaction force with the distance is depicted in Fig. 2.11. As the atoms are gradually brought together the attractive force between them increases until they are so close together that their electron clouds begin to repel each other electrostatically. This electrostatic repulsion progressively weakens

the attractive force as the inter-atomic separation continues to decrease and when the distance between the atoms reaches a couple of Angstroms, the total Van-der-Waals force becomes repulsive. In AFM, the local variation of the force acting between the tip and the sample is measured in order to generate the three dimensional images of the surface.

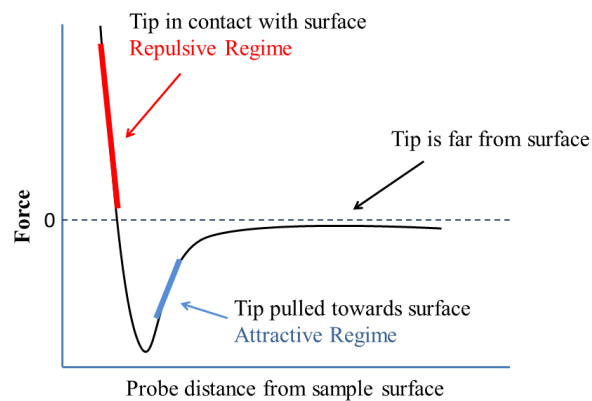


Figure 2.11: Dependence of force on the distance between the tip and sample.

Modes of operation

Because of AFM's versatility, it has been applied to a large number of research topics. The Atomic Force Microscope has also gone through many modifications for specific application requirements.

Contact Mode: The first and foremost mode of operation, contact mode is widely used. As the tip is raster-scanned across the surface, it is deflected as it

moves over the surface corrugation. In constant force mode, the tip is constantly adjusted to maintain a constant deflection, and therefore constant height above the surface. It is this adjustment that is displayed as data. However, the ability to track the surface in this manner is limited by the feedback circuit. Sometimes the tip is allowed to scan without this adjustment, and one measures only the deflection. This is useful for small, high-speed atomic resolution scans, and is known as variable-deflection mode.

Because the tip is in hard contact with the surface, the stiffness of the lever needs to be less than the effective spring constant holding atoms together, which is on the order of 1-10 nN/nm. Most contact mode levers have a spring constant of less than 1 N/m.

Noncontact mode: Noncontact mode belongs to a family of AC modes, which refers to the use of an oscillating cantilever. A stiff cantilever is oscillated in the attractive regime, meaning that the tip is quite close to the sample, but not touching it (hence, 'noncontact'). The forces between the tip and sample are quite low, of the order of pN (10^{-12} N). The detection scheme is based on measuring changes to the resonant frequency or amplitude of the cantilever.

Dynamic Force / Intermittant-contact / 'Tapping Mode' AFM: A stiff cantilever is oscillated closer to the sample than in noncontact mode. Part of the oscillation extends into the repulsive regime, so the tip intermittently touches or 'taps' the surface. The advantage of tapping the surface is improved lateral reso-

lution on soft samples. Lateral forces such as drag, common in contact mode, are virtually eliminated.

2.5 Optical Techniques

Luminescence in semiconductors can be stimulated by several different ways such as carrier excitation by using lasers or by current injection. A non-equilibrium state of electron and holes in conduction and valence band respectively is obtained. The adjacent recombination of electrons and holes may lead to the emission of a photon and this is called as radiative recombination.

Photoluminescence Spectroscopy

A very simple and powerful measurement technique is photoluminescence (PL) spectroscopy. The carriers are excited by a pump beam with a photon energy higher than the bandgap of the structure. The electrons then thermalize to the bottom of the conduction band and recombine emitting light with the bandgap energy. At room temperature, the luminescence of silicon is rather weak as most of the recombination of electron-hole pairs occur non-radiatively due to the traps and impurities. Thus, a laser is used as the excitation source together with a high sensitivity detector, such as a photomultiplier tube or an avalanche photodiode. PL spectroscopy is a very simple and fast technique, and is mainly used for material characterization in a broad variety of fields. The use of the as grown samples without any further treatment is one of its main advantage. Si and Ge are indirect

semiconductors and this can be understood by their band-structure.

Band-Structure

The electronic and optical properties of Si and Ge are related to their band structure. The band structure of a material depends upon the crystal structure and is the key to the dispersion relation of the charge carriers. Experiments on optical absorption, luminescence, and transport properties can be interpreted only if the band shapes and band-gaps are known. In a heterostructure, band offsets at the heterojunction are also needed for designing devices and interpreting experiments. The band structure of any material is conventionally embodied by the dispersion relation $E(\mathbf{k})$ where E is the energy of an electron (or hole) at the band edge with a wave vector \mathbf{k} in the first Brillouin zone.

Fig. 2.12 schematically shows energy dispersion relations for Ge and Si. Positive and negative energies refer to electrons and holes, respectively. Note that the conduction band minimum for Si doesn't lie at $\mathbf{k}=0$ i.e. Γ symmetry point, but away from it. Since, this minima lies in $[100]$ direction (Δ - minima), there is not just a single minimum of energy. Rather, there are six equal minima existing along the equivalent $\langle 100 \rangle$ directions in the crystal. For the case of Ge, the conduction band minima lies in the $[111]$ direction and hence there are eight equal minima existing along the equivalent $\langle 111 \rangle$ directions. Also, the valence band structure of both semiconductors is similar, exhibiting a maximum at the zone center $\mathbf{k}=0$. In the case of Si the maximum of the valence band is twofold degenerated.

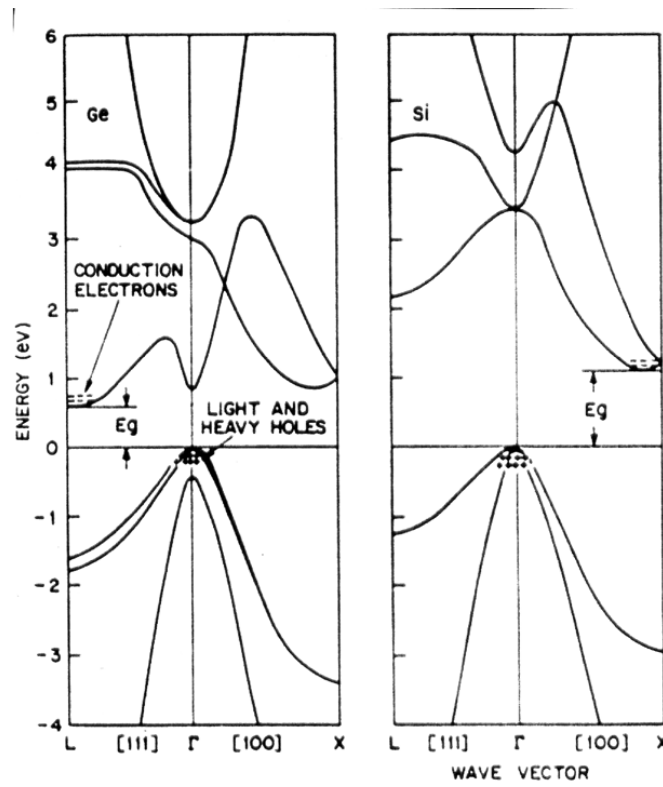


Figure 2.12: Electronic band-structure for Ge and Si.

In accordance to the different band bending and the resulting effective masses the states of both bands are called heavy and light holes (hh and lh, respectively). Due to the spin-orbit interaction the degeneracy is partly broken shifting the so-called spin-orbit-holes (soh) by 0.04 eV in the case of Si and 0.30 eV in the case of Ge to lower energies.

Optical transitions are divided into direct and indirect ones, depending on whether conduction band minimum and valence band maximum occur at the same k value. Figure 1 shows that the conduction band minimum of Si does not occur at $k = 0$. Hence, this is an indirect band-gap semiconductor. For direct band-gap semiconductors, exciting an electron from the top of the valence band to the bottom of the conduction band, leaving a hole in the valence band, will lead to the

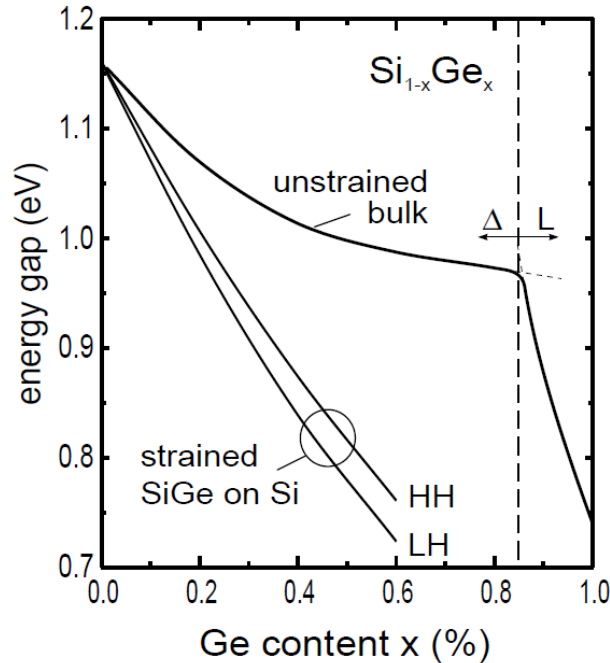


Figure 2.13: Band gap variation of $Si_{1-x}Ge_x$ alloys against Ge content x . The top curve gives the band gap energy for unstrained (cubic) alloys, which show a crossover from the Si-like (conduction band minima at Δ) to the Ge-like band-structure (conduction band minima at the L point) at $x = 0.85$. The two other curves are for pseudomorphic $Si_{1-x}Ge_x$ layers on a cubic Si substrate, which leads to a splitting of the valence band.

emission of a photon after the recombination of these two carriers. The energy of this photon is the same energy as the band gap E_g . In the case of indirect semiconductors, such direct recombination is not possible since the bulk selection rule $\Delta\mathbf{k} = 0$ has to be fulfilled. The transition from the highest occupied level of the valence band to the lowest unoccupied level of the conduction band is forbidden unless one or several momentum conserving phonons participate (absorption or emission).

Figure 2.13 shows the bandgap variations of $Si_{1-x}Ge_x$ alloys grown pseudo-

morphically on Si(001) substrate. Strain lowers the symmetry of the $\text{Si}_{1-x}\text{Ge}_x$ layers from cubic to tetragonal [34–36]. Lowering of the symmetry causes splitting of the band edges and modifies the band-gap. For $x < 0.85$ conduction band of the alloy remains Si-like. In the tetragonal symmetry the sixfold degeneracy of the Δ conduction band is partially lifted; it splits into a fourfold and a twofold degenerate state. When the layers are under biaxial compression (e.g., $\text{Si}_{1-x}\text{Ge}_x$ layers grown on Si(001) substrate), the fourfold degenerate state moves down toward the valence band and the twofold degenerate state moves up, away from the valence band. The degeneracy of the L band is not lifted under the tetragonal distortion. Degeneracy of the valence band at $\mathbf{k}=0$ is also lifted; the heavy hole band moves up (towards the conduction band) and the light hole band moves down. The difference in energy between the lowest conduction band and the highest valence band is the band-gap of the strained layers. A small contribution to the band-gap comes from the hydrostatic component of the strain. The actual separation of the split components depends on the magnitude of the strain and is calculated by the potential deformation theory.

Hence, the recombination of an electron-hole pair requires the emission (or absorption) of a phonon to fulfill the momentum conservation rule. The emission (or absorption) of a phonon offers one way to conserve the momentum during the recombination process of electrons and holes. The energy of the emitted photon is reduced by the amount of energy of the involved phonon, shifting the emission lines to lower energies. In the case of interband transitions the k-conservation

rule results from the exact periodicity of the crystal lattice. However, the Ge atoms in the $\text{Si}_{1-x}\text{Ge}_x$ alloy are statistically distributed, leading to some degree of disorder, which also effects the electronic properties due to different potentials of Si and Ge atoms. Thus, the k conservation rules must not always be fulfilled and there is a non-zero probability, that transitions without a phonon involvement may occur. These are called no-phonon (NP) transitions. In this case, the required momentum is conserved through scattering of the carriers at the alloy fluctuation potentials inside the $\text{Si}_{1-x}\text{Ge}_x$ layer.

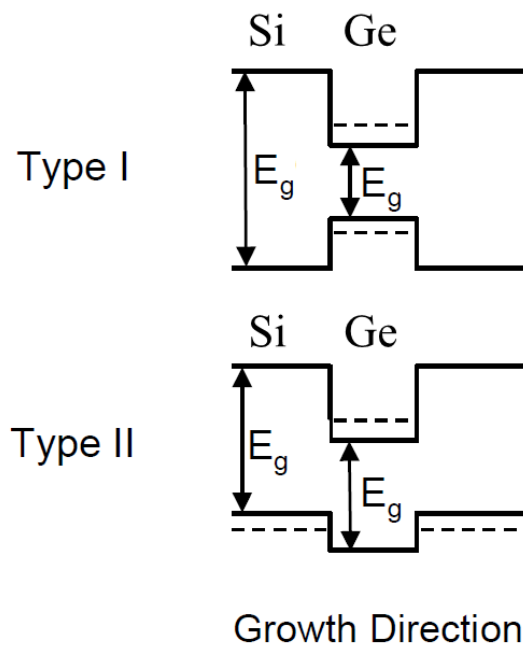


Figure 2.14: Band structures of type I and type II. In the former one the confinement of both electrons and holes is taking place in the same layer contrary to what is happening in the latter one. The dashed lines represent the energies of the confined particles.

Whenever a film of material with a smaller bandgap is grown between material

with a larger bandgap, localization of carriers takes place in the growth direction, due to the band offsets. Depending on the relative position of conduction and valence bands, one distinguishes between type I and type II alignment. In type I both types of carriers, electrons and holes, are localized in the same layer while in type II the charge carriers are localized in different layers (Fig. 2.14). Generally, strained SiGe on Si has been shown to have a type II structure.

PL spectroscopy is mostly performed at cryogenic temperatures in order to reduce thermal broadening effects. At such temperatures, the binding state of the electron-hole pair due to Coulomb attraction i.e., exciton is also observed. Due to the low excitonic binding energy, they are dissociate into free carriers by increasing the sample temperature.

Raman Spectroscopy

In Raman spectroscopy, a photon is scattered inelastically in a crystal. Incident and scattered photons have energy $\hbar\omega_L$ and $\hbar\omega_S$ respectively with corresponding wave-vectors k_L and k_S . In first order process one or several elementary excitations are created (Stokes process) or annihilated (Antistokes process). The conservation rules for a first order Raman process are given by

$$\omega_L - \omega_S = \pm\omega_J$$

$$k_L - k_S = \pm k_J$$

(2.3)

with $\hbar\omega_J$ and k_J are the energy and wavevector of the elementary excitations, here limited to a phonon, the $+(-)$ signs refer to the stokes (antistokes) process. A Raman spectrum is a plot of the intensity of Raman scattered radiation as a function of its frequency difference from the incident radiation (usually in units of wavenumbers, cm^{-1}). This difference is called the Raman shift. A variety of information can be extracted from the Raman spectra like the characteristic raman frequencies identify the composition of the material, the changes in the frequency of raman peak indicate the stress/strain state of the crystal, width of the raman peak suggest the quality of the crystal and the intensity of raman peak signify the amount of material.

Chapter 3

X-ray Scattering Techniques

X-rays have long been used as an essential tool in research to study the structure of bulk crystalline materials. They interact weakly with matter due to which multiple reflections can be neglected. The x-rays can penetrate deep into the bulk ranging from 0.1-10 mm, depending upon the material and the energy used. Thus, special sample preparation or environment is not usually required for the measurements. This allows them to provide microscopic structural information averaged over large sample volume. However, the penetration depth of x-rays can be tuned by choosing proper scattering geometry in order to gain information about the surface or about the bulk. For example, the differences in the refractive index are used in x-ray reflectivity and grazing-incidence small-angle x-ray scattering, while the strain fields are measured in coplanar x-ray diffraction (XRD) and grazing-incidence diffraction (GID). Also, the differences in the atomic scattering factors and their dependence on energy are used in anomalous scattering experi-

ments. In x-ray scattering, intensity distributions in reciprocal space are recorded instead of real-space images, and in most cases the interpretation of experimental data requires model assumptions and fitting routines.

3.1 X-ray Diffraction

X-Ray Diffraction (XRD) is used to study surfaces and interfaces. XRD has contributed also to many advances in the field of surface science, particularly when synchrotron radiation is used. In XRD, x-rays are directed at a crystal and the scattered rays are viewed from various angles at large distance. Specifically, we calculate the cross section of scattering from the sample. X-rays are used because their wavelength is comparable with the interatomic spacing. When an x-ray beam falls on an atom, two processes may occur: (a) the beam may be absorbed leading to removal of electrons from atom or (b) it may be scattered. Considering the classical theory for scattering process, the primary beam is an electromagnetic wave with electric vector varying sinusoidally with time and directed perpendicular to the direction of propagation of beam. The electric field exerts forces on the electrons of the atom producing accelerations of the electrons which in turn emit radiation. This radiation spreads in all the directions and is called scattered radiation having frequency same as the primary beam.

The Thompson formula describes the amplitude of the wave A_1 that comes from a scattering electron at r_e , as a function of the amplitude of the wave A_0 , that goes in, assuming the dipole approximation [41],

$$A_1 \exp(-ik_f \cdot r_e) = A_0 \frac{e^2}{mc^2} \frac{1}{R_0} \exp(-ik_i \cdot r_e) \quad (3.1)$$

where e and m are the electron's charge and mass, and R_0 , is the distance to the observer. $1/R_0$ arises because a spherical wave comes out when a plane wave goes in. The constant, e^2/mc^2 , has a very small value, of $3 \times 10^{-15} \text{m}$. Thus, even with the large number of electrons in a crystal, the total scattering cross section is still quite small. Hence, the kinematical approximation is valid, in which the amplitude scattered by an object is taken to be the sum of independent contributions from all the individual electrons.

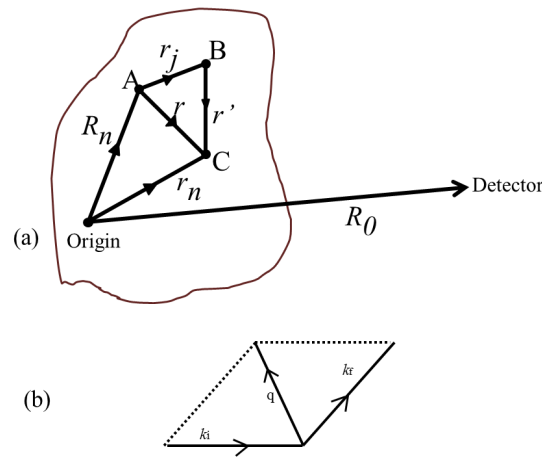


Figure 3.1: (a) Definition of the real space vectors. The origin of the crystal is shown, point A is the origin for the n^{th} unit cell, point B is the j^{th} atom of the n^{th} unit cell and point C is an electron belonging to the j^{th} atom of the n^{th} unit cell. (b) Definition of the reciprocal space incident and exit wave vectors k_i and k_f . These wave vectors both have magnitude $2\pi/\lambda$, with λ being the x-ray wavelength. The momentum transfer q is $k_f - k_i$.

A very important concept is that of 'momentum transfer', represented by 'q' and is the vector difference between the in-going wavevector k_i and the outgoing

wavevector k_f . Since the modulus of k_i and k_f are same and equal to $(2\pi/\lambda)$ for elastic scattering, where λ is the x-ray wavelength, we can derive,

$$|q| = 2|k| \sin \frac{2\theta}{2} \quad (3.2)$$

The momentum transfer relates both to the experimental scattering angle, 2θ , through equation 3.2, and to the theoretical scattering amplitude that is derived below. This can be seen by rearranging equation 3.1, with the definition $q = k_f - k_i$,

$$A_1 = A_0 \frac{e^2}{mc^2} \frac{1}{R_0} \exp(-iq \cdot r_e) \quad (3.3)$$

The results of a scattering experiment may be thought of as a map in momentum space, where q is the independent variable and the scattered intensity is the dependent variable. We now have the x-ray scattering amplitude from an individual electron, equation 3.3. Using the kinematical approximation, by simply summing the scattering amplitude from each electron, we arrive first at the scattering from an individual atom, then from one unit cell of the crystal, and finally from the entire macroscopic crystal.

In summing the scattering amplitudes from each electron in an atom, it is necessary to represent the electrons by their density distributions, as described by their wave-functions. This summation then becomes an integration:

$$\begin{aligned}
A_2 &= A_0 \frac{e^2}{mc^2} \frac{1}{R_0} \int_{-\infty}^{\infty} \rho(r') \exp(iq \cdot (R_n + r_j + r')) d^3r' \\
&= A_0 \frac{e^2}{mc^2} \frac{1}{R_0} f(q) \exp(iq \cdot (R_n + r_j))
\end{aligned} \tag{3.4}$$

where

$$f(q) = \int_{-\infty}^{\infty} \rho(r') \exp(iq \cdot r') d^3r' \tag{3.5}$$

The atomic form factor, $f(q)$, is defined as the Fourier transform of the electron density for a single atom. Also, $f(q)$ is a complex number and somewhat energy dependent because the x-ray can excite atomic transitions. The third step of the assembly is to add up the atoms inside one unit cell of the crystal. The atoms may not all be the same chemical element so they must be distinguished by assigning separate form factors, $f_j(q)$. If there are N_c atoms in the unit cell, then

$$\begin{aligned}
A_3 &= A_0 \frac{e^2}{mc^2} \frac{1}{R_0} \sum_{j=1}^{N_c} f_j(q) \exp(iq \cdot (R_n + r_j)) \\
&= A_0 \frac{e^2}{mc^2} \frac{1}{R_0} F(q) \exp(iq \cdot R_n)
\end{aligned} \tag{3.6}$$

where

$$F(q) = \sum_{j=1}^{N_c} f_j(q) \exp(iq \cdot r_j). \tag{3.7}$$

The function $F(q)$ which is the sum over all the atoms within one unit cell, is called the structure factor. Now, we add up all the unit cells to make the whole crystal. This is where the scattering becomes strongly focused into beams along certain directions and is then called diffraction. Assuming the crystal to be block-shaped with N_1 , N_2 and N_3 unit cells along the three crystal axes defined by the vectors, a_1 , a_2 and a_3 . We add up phase factors for the positions of the origin of each unit cell,

$$A_4 = A_0 \frac{e^2}{mc^2} \frac{1}{R_0} F(q) \sum_{n_1=0}^{N_1-1} \sum_{n_2=0}^{N_2-1} \sum_{n_3=0}^{N_3-1} \exp(iq \cdot (n_1 a_1 + n_2 a_2 + n_3 a_3)). \quad (3.8)$$

which can be simplified in the following form.

$$A_4 = A_0 \frac{e^2}{mc^2} \frac{1}{R_0} F(q) \left(\frac{1 - \exp(iN_1 a_1 q)}{1 - \exp(i a_1 q)} \right) \left(\frac{1 - \exp(iN_2 a_2 q)}{1 - \exp(i a_2 q)} \right) \left(\frac{1 - \exp(iN_3 a_3 q)}{1 - \exp(i a_3 q)} \right) \quad (3.9)$$

For x-ray diffraction intensity for a thin film deposited on a semi-infinite crystalline substrate can then be written as:

$$R = \left| \sum_{n=0}^N A_n \exp\left[i \left(\sum_{j=0}^n a_j \right) q_z\right] + A_s \frac{1 - \exp(iM a_s q_z)}{1 - \exp(i a_s q_z)} \right|^2 \quad (3.10)$$

where the first term is for the epitaxial multilayer stack having N layers. a_j is the lattice parameter of the j^{th} unit cell counting from the top of the film and

A_n is the scattering amplitude of the n^{th} unit cell. The second term represents the contribution from the substrate with a_s and A_s representing lattice parameter and scattering amplitude, respectively, for the substrate and M being the total number of unit cells.

Basics of X-ray Scattering

The propagation of radiation through any medium can be described by the optical formalism which depend upon the refractive index of the medium. For example, a ray of light propagating in air changes direction when it enters glass, water or any transparent material and this bending depends on the refractive index of the particular material. Hence, using Snell's law one can predict what will happen at the interface or how the interaction of electromagnetic radiation with matter will occur. The refractive index depends on the frequency of light.

The index of refraction of matter for visible light is always greater than unity. However for x-rays, it is slightly less than unity and is given as

$$n = 1 - \delta + i\beta \quad (3.11)$$

where δ and β are the quantities which depend on the electron density (ρ_e) and the absorption coefficient (μ) of the scattering material. These quantities are defined as follows:

$$\delta = \frac{\lambda^2 r_e \rho_e}{2\pi} \quad (3.12)$$

$$\beta = \frac{\lambda\mu}{4\pi} \quad (3.13)$$

where $r_e = 2.815 \times 10^{-5} \text{ \AA}$ is the classical electron radius, λ is the wavelength of the x-rays. Since, the refractive index of materials is less than unity for x-rays, the beam impinging on matter can be totally externally reflected given the incident angle is less than a critical angle θ_c . Critical angle can be determined using a Snell's law with $\cos(\theta_{tr}) = 1$. Thus,

$$\cos(\theta_c) = n = 1 - \delta \quad (3.14)$$

for small angles, above equation can be approximated as:

$$\theta_c^2 = 2\delta \quad (3.15)$$

The total external reflection is observed at very low incidence angles with $\theta < 0.5^\circ$. At larger angles, as the penetration of x-rays increases, the reflectivity decreases considerably. It is near to the critical angle that x-rays can probe both in-plane and out-of-plane structures at the surfaces/interfaces of thin films and several measurement techniques are thus developed for this which are collectively known to be Grazing Incidence X-ray Scattering (GIXS) techniques. Fig. 3.2 shows the schematic of the GIXS scattering geometry. The incident X-ray beam has momentum vector k_i and the elastically scattered x-rays from the sample has a momentum vector k_f with $|k_i| = |k_f| = k_0 = 2\pi/\lambda$; where λ is the wavelength of

x-rays. Thus, the wavevector transfer, $q = k_f - k_i$ depends upon the incident and exit angles. The different components of wavevector transfer are given as:

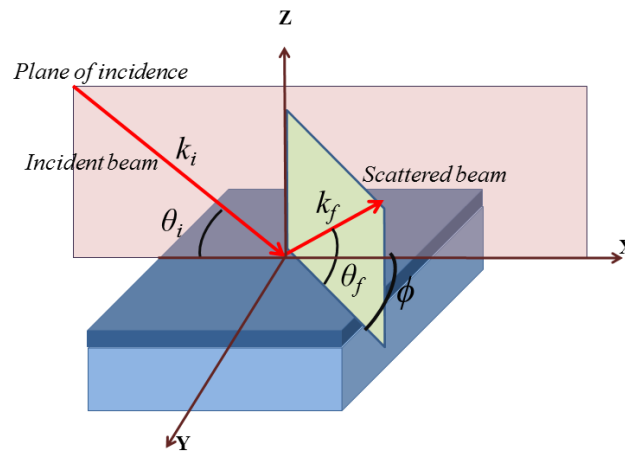


Figure 3.2: Schematic showing the GIXS scattering geometry.

$$q_x = k_0(\cos(\theta_f)\cos(\phi) - \cos(\theta_i)) \quad (3.16)$$

$$q_y = k_0\cos(\theta_i)\sin(\phi) \quad (3.17)$$

$$q_z = k_0(\sin(\theta_f) + \sin(\theta_i)) \quad (3.18)$$

where X-Z is the plane of incidence and the detector is placed at an angle ϕ out of this plane in Y direction.

3.2 X-ray Reflectivity

In X-Ray Reflectivity (XRR) technique, x-ray beam is allowed to incident on a sample surface at a grazing incidence θ_i and the reflected intensity is recorded in the plane of incidence at an angle θ_f . If the angle of incidence of impinging x-rays is sufficiently small (less than θ_c), the penetration depth and the scattering is limited to the near surface region. Reflectivity data is generally taken at angles considerably larger than the critical angle of total external reflection and therefore penetration depth is of the order of hundreds of nanometers. The necessary angular conditions maintained during the measurements are $\theta_i = \theta_f$ and $\phi = 0$ (refer to Fig. 3.2). With these angular conditions the reflected intensity is only a function of out-of-plane wave transfer vector q_z and $q_x, q_y = 0$. Thus, XRR provides us with structural information along the out-of-plane direction of the surfaces and interfaces.

3.2.1 Parrat Formalism

An electromagnetic plane wave represented by its electric field $E(\mathbf{r}) = E_0 \exp(i\mathbf{k}_i \cdot \mathbf{r})$, which penetrates into a medium having an index of refraction $n(\mathbf{r})$, propagates according to the Helmholtz equation given by:

$$(\nabla^2 + k^2 n^2(\mathbf{r}))E(\mathbf{r}) = 0 \quad (3.19)$$

where k is the wave-vector of the x-rays given by $k = 2\pi/\lambda$. In vacuum, the

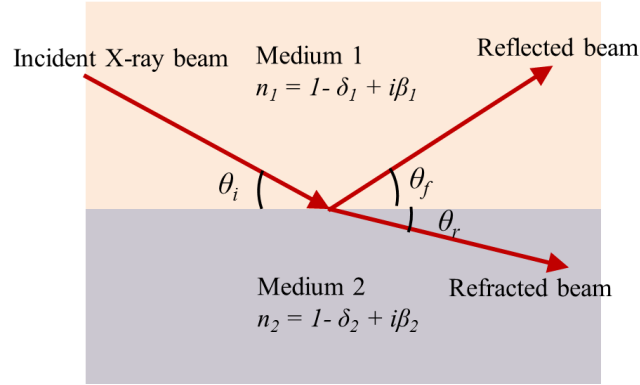


Figure 3.3: Schematic showing reflection and refraction of incident X-rays for Vacuum-Medium interface.

z-component of the momentum transfer vector, normal to the surface, is given by

$$q_{z,0} = \frac{2\pi}{\lambda} (\sin(\theta_i) + \sin(\theta_f)) \quad (3.20)$$

for specular reflectivity, $\theta_i = \theta_f$, hence one can write: $k_{z,0} = q_{z,0}/2 = 2\pi \sin(\theta_i)/\lambda$. By Snell-Descartes' law of refraction for the single interface shown in Fig. 3.3,

$$\frac{\cos(\theta_i)}{\cos(\theta_r)} = \frac{n_1}{n_2} = \frac{1 - \delta_1 + i\beta_1}{1 - \delta_2 + i\beta_2} \quad (3.21)$$

As the values of δ and β for any material for x-rays are of the order of 10^{-6} and 10^{-7} respectively, equation 3.21 can be expanded as follows by ignoring the higher order terms.

$$\begin{aligned}
\frac{\cos(\theta_i)}{\cos(\theta_r)} &= 1 - (\delta_1 - \delta_2) + i(\beta_1 - \beta_2) \\
&= 1 - \frac{\lambda^2 r_e}{2\pi} \Delta\rho_e + i \frac{\lambda}{4\pi} \Delta\mu
\end{aligned} \tag{3.22}$$

Thus, using equation 3.22, one can define the critical angle for any interface as follows:

$$\theta_c = \sqrt{2(\delta_1 - \delta_2)} \tag{3.23}$$

and the critical wave-vector can be given as

$$q_c = \frac{4\pi}{\lambda} \sin(\theta_c) \tag{3.24}$$

Depending on the critical wave-transfer vector $q_{c,i}$ of i^{th} medium with respect to that of vacuum the wave-transfer vector along z in that medium can be written as $q_{z,i} = \sqrt{q_{z,0}^2 - q_{c,i}^2}$. By applying proper boundary conditions for the electric field and its derivative, at the interface of two media, we can write the Fresnel formulas for the reflection and transmission coefficients as follows:

$$r_{1,2} = \frac{q_{z,1} - q_{z,2}}{q_{z,1} + q_{z,2}} \tag{3.25}$$

and

$$t_{1,2} = \frac{2q_{z,1}}{q_{z,1} + q_{z,2}} \quad (3.26)$$

Then, the x-ray reflectivity expression for an interface separating two media can be written as follows:

$$\begin{aligned} R &= r_{1,2} r_{1,2}^* \\ &= \left| \frac{\sqrt{(q_{z,0}^2 - q_{c,1}^2)} - \sqrt{(q_{z,0}^2 - q_{c,2}^2)}}{\sqrt{(q_{z,0}^2 - q_{c,1}^2)} + \sqrt{(q_{z,0}^2 - q_{c,2}^2)}} \right|^2 \end{aligned} \quad (3.27)$$

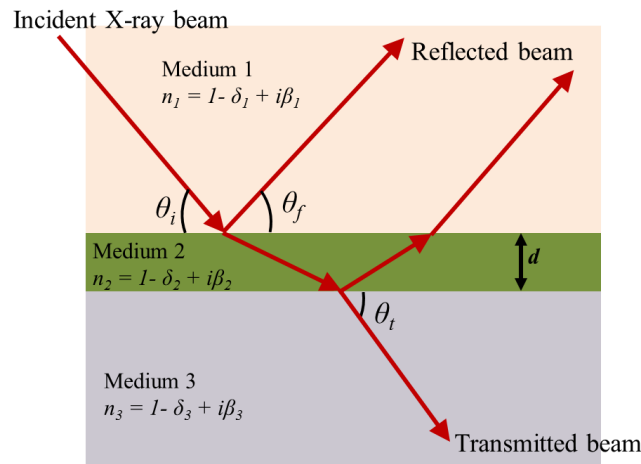


Figure 3.4: Schematic showing reflection and transmission of incident X-rays for a thin film sandwiched between two media.

In the case of a thin film of finite thickness 'd' as shown in Figure 3.4, we have to solve the wave equations at two interfaces. It is interesting to note that the continuity condition at $z = d$ will generate an extra factor, which in turn will give us reflectance at the film-substrate interface as

$$r_{2,3} = \frac{q_{z,2} - q_{z,3}}{q_{z,2} + q_{z,3}} \exp(-iq_{z,2}d) \quad (3.28)$$

By simple calculations and noting the fact that $r_{21} = -r_{12}$, we can write the reflectance from the thin film sand-witched between two media as

$$r_0 = \frac{r_{1,2} + r_{2,3}}{1 + r_{1,2}r_{2,3}} \quad (3.29)$$

We can easily extend the above calculation to the case of reflectivity for a system having N such thin films (stratified media), having smooth interfaces. We denote the thickness of each film by d_n : A set of simultaneous equations similar to Equation 3.29 can be solved and one can arrive at a recursive formula given by

$$r_{n-1,n} = \frac{r_{n,n+1} + F_{n-1,n}}{1 + r_{n,n+1}F_{n-1,n}} e^{-iq_{z,n}d_n} \quad (3.30)$$

where

$$F_{n-1,n} = \frac{q_{z,n-1} - q_{z,n}}{q_{z,n-1} + q_{z,n}} \quad (3.31)$$

To obtain the specular reflectivity of the system having N layers one solves the above recursive relations from the bottom layer with the knowledge that $r_{N,N+1} = 0$, since the thickness of the $(N + 1)^{th}$ medium (normally the substrate) can be taken as infinite. The detailed calculation for the reflectivity from multilayers can be found in several reviews and texts [37–40].

As we measure intensity of reflected x-ray beam, not its amplitude and phase, the determination of the electron density profile (EDP) from the reflectivity profile becomes non-trivial. Normally, one assumes a priori distribution of EDP across the thin film and calculates specular reflectivity profile by approximating this EDP by a series of slabs having constant electron densities using a recursive technique starting at the substrate/film interface. The calculated reflectivity profile is then fitted to the experimental data by varying some of the parameters such as the electron density of each slab, thickness of the slabs and roughness of interfaces. This conventionally used technique works well for systems in which actual EDP is close to the a priori assumption of EDP with which the non-linear fitting process is started and only a few parameters are involved in fitting. Due to the recursive non-linear relationship between real space parameters, e.g. thickness and electron density of each slab and reflectivity profile, determination of parameters by fitting becomes problematic when initial guess of real space parameters are far away from the actual solution.

3.2.2 Scheme based on Distorted Wave Born Approximation

In this scheme, we treat the EDP of a thin film as $\rho_0 + \Delta\rho(z)$, where ρ_0 is the average electron density over the total thickness of the film and $\Delta\rho(z)$ is the variation of electron density as a function of the film depth 'z' (the film surface is taken as $z = 0$, with z positive into the substrate). We are interested in finding $\rho(z)$. In our method, we have considered the film to be composed of a number of thin slices or

boxes of equal thickness 'd' with ρ_i (given by $\rho_0 + \Delta\rho_i$) as the electron density of the i th box. We can then write $\Delta\rho(q_{fz})$ as

$$\begin{aligned}\Delta\rho &= \int_{-\infty}^{\infty} \Delta\rho(z) \exp[iq_{fz}] dz \\ &= \Delta\rho_1 \int_0^d \exp[iq_{fz}] dz + \dots + \Delta\rho_N \int_{(N-1)d}^{Nd} \exp[iq_{fz}] dz \quad (3.32)\end{aligned}$$

Rewriting the above equation gives:

$$\Delta\rho = \frac{i}{q_{fz}} \left[\left(\sum_{j=2}^{j=N} (\Delta\rho_j - \Delta\rho_{j-1}) \exp[iq_{fz}(j-1)d] \right) + \Delta\rho_1 + \Delta\rho_N \exp(iq_{fz}Nd) \right] \quad (3.33)$$

where N is the total number of boxes used to represent the total film of thickness $D = Nd$. In the above expression, $q_{fz} = q^2 - q_c^2$ is the z-component of momentum transfer vector in the film, q_c being the critical wavevector for the average film of electron density ρ_0 . The above expression of $\Delta\rho(q_{fz})$ to calculate the specular reflectivity, given in the DWBA [71, 72] by

$$R(k) = \left| ir_0(k) + \frac{2\pi b}{k} (a^2(k)\Delta\rho(q_z) + b^2(k)\Delta\rho^*(q_z)) \right|^2 \quad (3.34)$$

where $r_0(k)$ is the specular reflectance coefficient of the multilayer film with AED ρ_0 , $a(k)$ and $b(k)$ are the coefficients for the transmitted and reflected amplitudes in the average film and are given by:

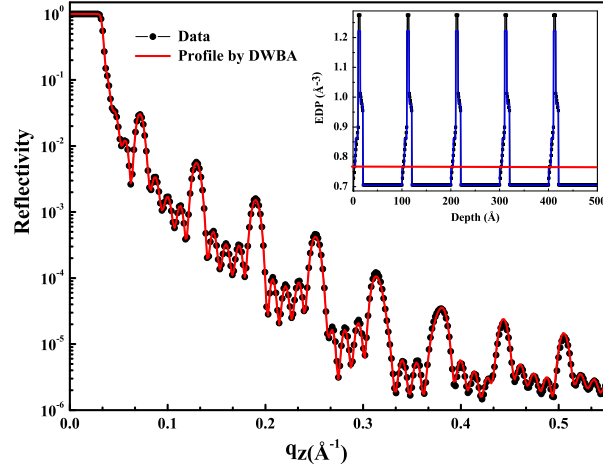


Figure 3.5: Specular reflectivity of the test 5 bilayer Si/Ge system. Black filled circles represent the ‘Data’ and red line the profile obtained from DWBA formalism. The inset shows the EDP used to generate Data (black symbols) and EDP obtained by fitting (blue line), using DWBA formalism. The horizontal (red) line in the inset shows the value of AED, ρ_0 .

$$a(k) = \frac{1 + r_{12}}{1 + r_{12}r_{23}} \quad (3.35)$$

$$\text{and } b(k) = a(q_z)r_{23}$$

The applicability of the method discussed here was checked by making test simulations of several Si/Ge bilayer systems on Si substrate and result of a five bilayer film is presented here. The thicknesses of Si and Ge for this simulation were taken as 80 Å and 20 Å and ED as 0.7095 Å⁻³ and 1.27527 Å⁻³ respectively. The Si-Ge interfaces were taken as linearly graded to mimic the inter-diffusion observed in our sample. The X-ray reflectivity profile for this system was generated using Parrat formalism [40] as discussed in section 3.2.1, which is represented by ‘Data’ in Fig. 3.5 and the corresponding EDP is shown in the inset (black sym-

bol). The AED, ρ_0 , value taken here is represented by red horizontal line in the inset. Accordingly, the values of $\Delta\rho_i$ were assigned in the initial guess of EDP assuming that position of Ge layers are known and interfaces are abrupt. The box size, d , was taken to be 5 Å. It is interesting to note that linear interfacial profile used to generate ‘Data’ comes out correctly from this DWBA fitting (see Fig. 3.5). By carrying out similar analysis on a variety of ‘test’ samples, we concluded that this method is quite sensitive and small features of EDP could be detected successfully.

3.3 X-ray Diffuse Scattering

Specular reflectivity is sensitive to the average density profile along the normal to a sample surface. Very often, one would also like to determine the statistical properties of surfaces or interfaces (i.e. the ‘lateral’ structures in the plane). The diffuse x-ray scattering experiments allow the determination of the lateral lengths of surface morphologies and of the correlations between buried interfaces over more than 5 orders of magnitude i.e., from Å to tens of microns in plane. The manner in which surface/interface roughness gives rise to off-specular diffuse scattering is best discussed in terms of differential scattering cross section $d\sigma/d\Omega$. Under Born Approximation, the differential scattering cross-section can be written as:

$$\frac{d\sigma}{d\Omega} = r_e^2 \left| \int dr \rho(r) \exp[i.q.r] \right|^2 \quad (3.36)$$

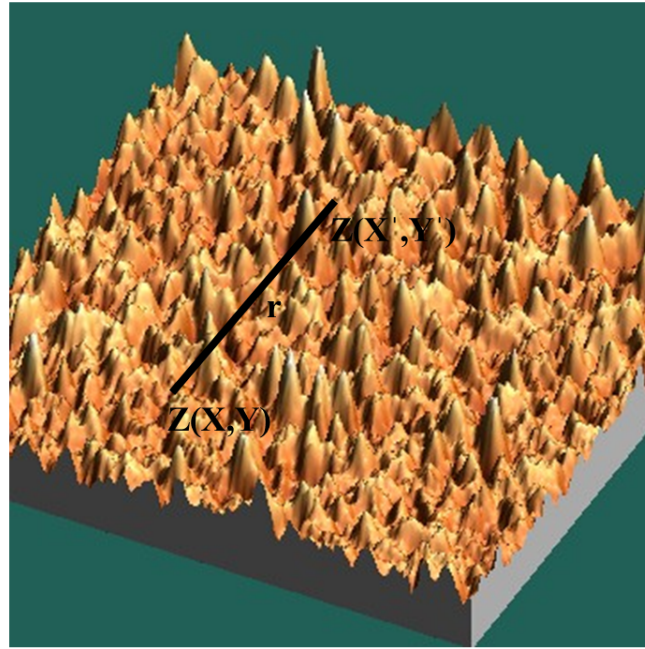


Figure 3.6: A typical rough surface. For an isotropic rough surface the height correlation functions depends on r , irrespective of the location of the points (x, y) and (x', y') .

Considering a typical rough surface as shown in Fig. 3.6 defined by its height fluctuations $z(x, y)$, the differential cross-section can be written as:

$$\frac{d\sigma}{d\Omega} = r_e^2 \rho^2 \left| \int_{-\infty}^{z(x,y)} dz \exp[iq_z z] \int_{-\infty}^{+\infty} dx \exp[iq_x x] \int_{-\infty}^{+\infty} dy \exp[iq_y y] \right|^2 \quad (3.37)$$

The above equation can be simplified to

$$\frac{d\sigma}{d\Omega} = \frac{r_e^2 \rho^2}{q_z^2} \left| \int_{-\infty}^{\infty} dx dy \int_{-\infty}^{\infty} dx' dy' \exp[iq_z(z(x, y) - z(x', y'))] \times \exp[iq_x(x-x')] \exp[iq_y(y-y')] \right| \quad (3.38)$$

To proceed further, we need to formulate a geometrical description of a rough surface. It has been found that description of surface geometry can be done conveniently using the concept of fractals. Assuming the difference in heights for the interface at two different positions (x, y) and (x', y') , $U = z(x, y) - z(x', y')$ to be a Gaussian Random Variable, one can define a height difference correlation function as

$$g(X, Y) = \langle [z(x, y) - z(x', y')]^2 \rangle \quad (3.39)$$

with $X = x - x'$ and $Y = y - y'$ and the average denotes an ensemble average over all possible configurations of the surface. For a commonly observed type of rough surface, the rms roughness scales as a self-affine fractal. Since statistically $g(X, Y)$ is equivalent to σ^2 , for isotropic self-affine rough surfaces $g(X, Y)$ can be written as

$$g(X, Y) = g(r) = Ar^{2\alpha} (0 < \alpha < 1) \quad (3.40)$$

where $r = \sqrt{(X^2 + Y^2)}$. Using the definition of $g(X, Y) = g(r)$ in equation 3.39 we can write

$$\begin{aligned} g(r) &= \langle z(0) \rangle^2 + \langle z(r) \rangle^2 - 2 \langle z(0)z(r) \rangle \\ &= 2\sigma^2 - 2C(r) \end{aligned} \quad (3.41)$$

Here $\langle z(0) \rangle^2 = \langle z(r) \rangle^2 = \sigma^2$. This is valid only under the assumption of stationarity of U. $C(r) = \langle z(0)z(r) \rangle$ is defined as the height-height correlation of the surface. The height-height correlation can have several different forms but the form that is used most commonly is

$$C(r) = \sigma^2[1 - \exp(-r/\xi)^{2\alpha}] \quad (3.42)$$

Accordingly, a configuration average has to be performed over all possible configurations of the interface to calculate the scattering cross-section. By performing appropriate change of variables one can write equation 3.42 as

$$\frac{d\sigma}{d\Omega} = \frac{r_e^2 \rho^2}{q_z^2} A \left| \int_{-\infty}^{\infty} \int_{-\infty}^{\infty} dX dY \exp[-q_z^2 g(X, Y)/2] \exp[iq_x X + iq_y Y] \right| \quad (3.43)$$

where A is the area of the surface illuminated by the incident beam. Using equation 3.41, scattering cross-section can be written as:

$$\frac{d\sigma}{d\Omega} = \frac{r_e^2 \rho^2}{q_z^2} A e^{-q_z^2 \sigma^2} \left| \int_{-\infty}^{\infty} dX dY e^{q_z^2 C(X, Y)} e^{-i(q_x X + q_y Y)} \right| \quad (3.44)$$

The above equation can be split into two parts: specular and diffuse. The specular component yields the specular reflectivity as follows:

$$R = \frac{16\pi^2 \rho^2 r_e^2}{q_z^4} e^{-q_z^2 \sigma^2} \quad (3.45)$$

Thus, the diffuse intensity, I_d can be written as

$$I_d = I_0 \frac{r_e^2 \rho^2}{q_z^2 \sin \theta_i} e^{-q_z^2 \sigma^2} \left| \int \int dX dY (e^{q_z^2 C(X,Y)} - 1) e^{-i(q_x X + q_y Y)} \right| \quad (3.46)$$

3.4 Grazing Incidence Diffraction

Grazing Incidence Diffraction (GID) is a special scattering technique used to study the surfaces as x-rays are not intrinsically surface selective probe. Availability of high brilliance synchrotron sources has also made it easier to obtain surface information simply by observing the deviations from ideal bulk scattering and attributing these deviations to the surface. This method is highly efficient when the bulk is a single crystal as then the scattering from it is largely limited to Bragg peaks. Thus, the scattering apart from the Bragg peaks can be attributed to the reconstructed surface or an adsorbed monolayer.

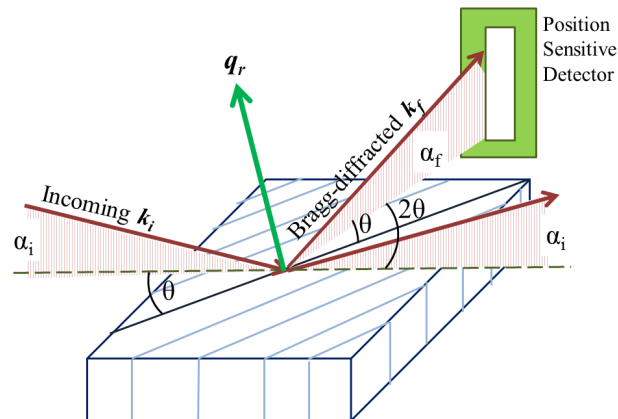


Figure 3.7: Schematic showing the GID scattering geometry.

To study the nanostructures or surfaces grazing incidence diffraction (GID) geometry becomes extremely significant to find out information of the composition, strain and morphology. GID is based on the fact that the refractive index of most materials is slightly smaller than 1. According to Snells law an angle of total external reflection is present at the interface between e.g. a crystal surface, and vacuum or air both of which have a refractive index equal to 1. This angle of total external reflection depends on the material and the x-ray energy, as explained earlier. At this angle, however, the substrate is not completely invisible to x-rays, but only an evanescent wave penetrates into and scatters from it but maximum scattering occurs from the surface as needed. For the GID experiments as performed in this work, grazing incidence and exit conditions were chosen for the incident and exit angles α_i and α_f . The intensity distribution along the exit angle α_f was recorded using a position sensitive detector (PSD), which was mounted perpendicular to the surface. This geometry gives access to Bragg reflections that lie in the surface plane. This geometry is sketched in Fig. 3.7. With $\alpha_{i,f}$ small, q_z is close to zero, so that grazing-incidence diffraction is sensitive only to the in-plane lattice parameter, and not to lattice parameters and strains in the growth direction. In this scattering geometry the crystal has to be rotated into diffraction condition. Hence grazing-incidence diffraction combines diffraction at lattice planes perpendicular to the sample surface with reflection of the incoming beam from the surface. Most of the x-ray beam is specularly reflected at the surface leading to a huge reduction in the scattering from the surface. Hence for most grazing-incidence diffraction

experiments, synchrotron radiation needs to be used.

Scans along the reciprocal lattice vector $G(hkl)$ are performed by turning the sample around its surface normal by an angle θ and the detector arm supporting the PSD by $\phi = 2\theta$ around the same axis. These scans are called radial scans as they cross a Bragg reflection on the radial path that points from the origin to the Bragg point. The momentum transfer achieved in radial direction in such a scan is given by

$$q_r = |k_f - k_i| = 2|k|\sin(\phi/2) = \frac{4\pi\sin(\theta)}{\lambda} \quad (3.47)$$

The angular scan or rocking scan considers a simple rotation of the sample around its surface normal at a fixed detector angle ϕ . It is to be noted here that only the angular momentum transfer ($q_a = (4\pi/\lambda)\sin(\theta - \phi/2)$) changes in these scans while the radial momentum remains constant. q_{rad} and q_{ang} are perpendicular directions in reciprocal space.

In the case of uncapped QDs with large lattice mismatch, to a good approximation it is possible to evaluate the strain and (to a certain extent) composition distribution with the so-called ‘isostrain scattering’ model. In this approximation, the strain is a monotonic function of the height above the surface, thus the GID signal scattered from the islands can be decomposed into slices with constant strain, at a certain height. The scattering signal from each slice is a spectrum centered at $q_r \propto 2\pi/a_{slice}$ along q_r , with a width proportional to the slice diameter along q_a . Thus, the island width as a function of lattice parameter can be estimated. Be-

sides, the intensity distribution along q_z presents a maximum related to the height of the slice, due to the interference between beams scattered within the island and reflected at the sample's surface. Finally the chemical composition as a function of lattice parameter can be estimated from radial scans for a weak and a strong reflection, such as (200) and (400). Thus, island width, strain and composition can be mapped as a function of island height.

3.5 Anomalous X-ray Scattering

In anomalous diffraction, the x-ray energy dependence of the atomic scattering factor of one element is exploited. The goal is again to evaluate an intensity ratio but this time of only one Bragg reflection measured at different x-ray energies. Schulli et al [98] showed that anomalous x-ray diffraction can indeed be used to obtain the necessary chemical sensitivity for a direct determination of composition profiles in SiGe islands. It is a well established technique to tune the x-ray energy close to an absorption edge to enhance the sensitivity for a particular element. In the SiGe system, the only edge which allows for an x-ray wavelength that can be used for diffraction is the Ge K edge. In general, the energy and momentum dependency of the atomic scattering factor is expressed by $f(Q, E) = f_0(Q) + f'(E) + if''(E)$ with $f'(E)$ and $f''(E)$ being the real and imaginary parts of the energy dependent correction that become important close to an absorption edge.

The Q dependency of the form factor originates from the non-negligible spatial distribution of the electrons of an atom, as it represents the Fourier transform of

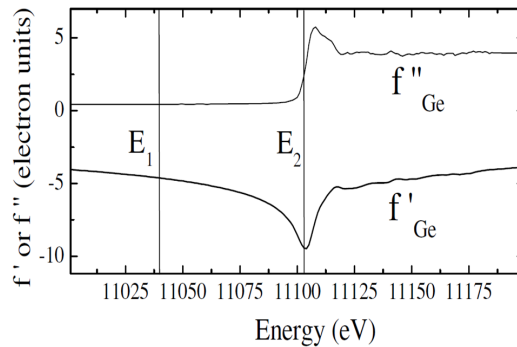


Figure 3.8: Anomalous corrections f' and f'' for Ge in the vicinity of the K-absorption edge. [Ref: [98]]

the electron distribution. Therefore f_0 equals the total number of electrons Z for forward scattering, but decreases for higher momentum transfer Q . This decrease is generally neglected in the correction terms f' and f'' , based on the argument that the inner electron shells that are responsible for these terms are very localized in space. Thus the anomalous scattering effects can be enhanced considerably by measuring Bragg reflections for high momentum transfers and hence improve the sensitivity for the composition in the SiGe system. f' and f'' are presented in Fig. 3.8 as a function of energy. The two probed energies $E_1 = 11\,043$ eV and $E_2 = 11\,103$ eV are indicated.

Chapter 4

MBE growth of Si-Ge Multilayers

This chapter deals with the growth and characterization of MBE grown epitaxial Si/Ge multilayers. The Si/SiGe heterostructures are of particular importance as quantum dots (i.e. Ge quantum dots in Si matrix) having size of the order of nanometer may get embedded at the interfaces during growth process. The composition and size of these dots vary with the deposition conditions [42]. A uniform spatial distribution of these quantum dots is required for their possible use in technological applications. It was shown earlier [43] that such spatial uniformity of quantum dots can be obtained by growing Si/SiGe multilayer structures. Such self-assembled Ge quantum dots in multilayer structure [44, 45] show optoelectronic properties and are used in the fabrication of photodetectors such as Mid Infra Red photodetector [46] and QWIPs. Recently, Si/SiGe superlattice structures have exhibited electroluminescence in the frequency close to 3THz [47].

Crosssectional Transmission Electron Microscopy (XTEM) is used extensively

to provide a direct picture of the superlattice structures. XTEM however presents a very localized information about the system. Thus, X-ray scattering techniques such as x-ray reflectivity (XRR) and x-ray diffraction (XRD) are employed to determine the out-of-plane compositional profile of these SL structures which give us quite an accurate information about average interfacial intermixing. Raman spectroscopy is used to characterize these SL structures as well. Like XRD, it is also a fast, accurate and non-destructive method. Depending upon the position, intensity and width of Raman lines due to Ge-Ge, Ge-Si and Si-Si modes, one can obtain information about the composition, strain and confinement with in the SiGe SL structures.

A method for the morphological and structural characterization of the multilayer system using X-ray reflectivity and diffraction techniques is discussed in detail. and XRR is a powerful technique to find out the average electron density profile of the buried layers in a film as a function of depth. XRD is useful in characterizing the inter-diffusion, strain and composition of a film at the atomic level [48]. The analysis schemes described in the present work are based on Distorted Wave Born Approximation (DWBA) and Born Approximation (BA) for XRR and XRD respectively. By considering a typical multilayer system, it is demonstrated that the electron density profile (EDP) obtained from XRR can be used efficiently to extract composition and strain profile as a function of depth through fitting of XRD data.

Due to the 4% lattice mismatch between Si and Ge, the Si/SiGe (Si/Ge) mul-

tilayer structures witness strain at the interfaces which propagate in the respective layers. The strain relaxation can occur through elastic relaxation by 3D island formation or inelastic (plastic) relaxation by misfit dislocations. The mode of relaxation depends highly on the growth conditions and the thicknesses of the constituent layers in the multilayer system. However, the interdiffusion at interfaces leads to some strain relaxation. It is reported earlier that during Ge deposition on Si, apart from Ge diffusing on surface, underlying Si atoms also participate in the diffusion process by moving to the surface and hence leading to intermixing. Intermixing also leads to the change in composition of the Ge or SiGe layers in the multilayer structure. This intermixing effect influences the shape and depth of the potential wells for electronic excitations and their phonon spectra. XRD technique is a very sensitive method for studying interdiffusion in superlattice structures and intermixing at the interfaces directly influences the intensity of superlattice satellite peaks [49].

A typical Si/Ge multilayer sample is grown by alternate deposition of Si and Ge on the substrate. During deposition, the Si substrate is kept at a desired temperature in the range of 300-800°C. First of all, a thick Si buffer layer of around 100 nm is deposited. This is done because the substrate surface becomes rough due to the chemical cleaning and thus Si buffer layer provides an atomically smooth surface for the preparation of desired structure. After buffer layer, alternate Ge and Si layers are deposited by choosing suitable temperature for the Ge effusion cell (to control the Ge deposition rate) and Si deposition rate is controlled by the

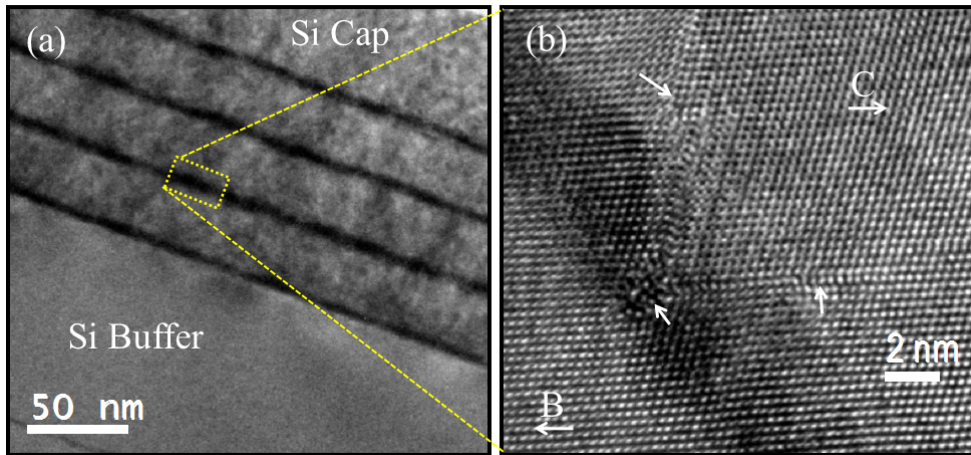


Figure 4.1: XTEM images (a) of a 4 bilayer Si/Ge multilayer sample and (b) its High resolution TEM micrograph. The presence of misfit dislocations is evident and are indicated by arrows.

quartz crystal monitor [50].

4.1 Si/Ge multilayers showing plastic relaxation

Fig. 4.1(a) shows cross-sectional TEM micrograph of a multilayer sample consisting of 4 Si/Ge bilayers deposited on Si(001) substrates. The Si buffer layer and Si cap layers are indicated. The dark region in the image corresponds to the Ge layer and the light gray region to the presence of Si. During growth, Si and Ge deposition rates were chosen to be 1 Å/sec. Substrate temperature and rotation speed were 500°C and 3 rotations per minute during deposition. The base pressure of the growth chamber was 2×10^{-11} Torr. Fig. 4.1(b) shows the high resolution XTEM image of the same sample. The Si/Ge layer thicknesses were chosen to be 300/50 Å respectively. Presence of misfit dislocations can be observed easily in the layers (marked by arrows in the figure). This plastic relaxation present in the

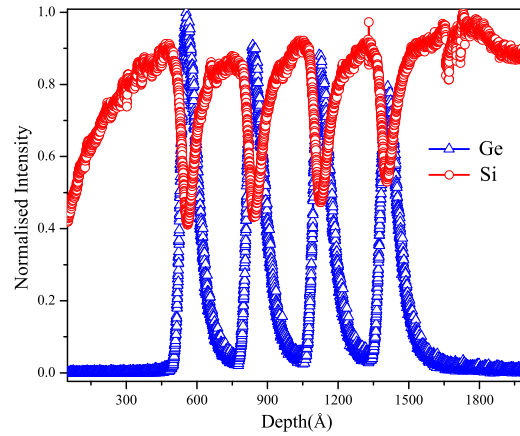


Figure 4.2: SIMS depth profile of the four bilayer sample. The profiles for Si and Ge are indicated. Separate layers of Si and Ge can be observed as the presence of Ge (peak in Ge profile) leads to absence of Si (dip in Si profile).

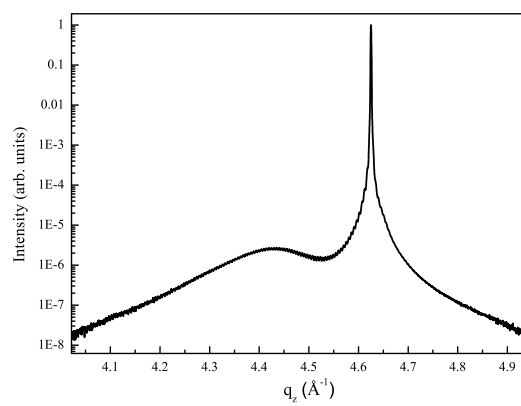


Figure 4.3: X-ray diffraction profile of the four bilayer sample. The sharp peak corresponds to Si and the broad one is due to the presence of Ge in almost relaxed state.

multilayers can be attributed to the thickness of Ge layer which is way higher than the critical thickness (refer Fig. 1.4).

In order to measure the average individual Si/Ge layer thickness of the grown multilayer samples, SIMS depth profile measurements were carried out. Secondary ion mass spectrometry (SIMS) studies were performed using a quadrupole mass spectroscopy-based SIMS instrument (HIDEN Analytical Ltd., UK) with a high-performance triple quadrupole filter and a 45° electrostatic sector-field energy analyzer. Samples were bombarded with 1.5 keV Cs⁺ primary ions at an angle 20° with respect to the surface normal. Primary ion current was kept fixed at 60 nA. The beam was rastered over an area of 1000 × 1000 μm and secondary negative ions were collected from the central 200 × 200 μm area in order to avoid the edging effect. Fig. 4.2 shows the SIMS depth profile measurements of the sample. The respective thicknesses of Si and Ge layers were found to be 30 nm and 5 nm which match with the values obtained from XTEM measurements. X-ray diffraction measurements were also carried out at an energy of 11.4 keV at PF, Japan. Fig. 4.3 shows the XRD profile of this multilayer sample. The sharp peak corresponds to the Si(001) substrate and the Si layers in the sample and the lower intensity broad peak corresponds to the Ge layers. This XRD profile lacks the satellite peaks as are generally observed in the superlattice structures. This is due to the presence of huge dislocations in the system which reduce the single-crystallinity of the system.

4.2 Si-Ge Superlattices

4.2.1 XTEM Study

Fig. 4.4-4.9 show cross-sectional TEM images of the various superlattice (SL) samples considered here. These superlattices are deposited by alternate deposition of Si and Ge (or SiGe alloy). The layer thicknesses and layer compositions were chosen in such a manner as to prepare nanostructures in the layers and also to observe pseudomorphic growth according to Fig 1.4. Details of each sample such as Ge layer composition depending upon the nominal deposition conditions, growth temperature (T_G), rate of deposition employed for Si, the thickness of the superlattice period and the nominal thicknesses of the layers consisting of superlattice are provided in Table 4.1. In all the crosssectional images, 'B' and 'C' represent the Si buffer and Si cap locations. All the samples were grown on Si(001) substrates. First of all, a thick Si buffer layer is deposited on Si(001) substrate which can be seen in XTEM images. A few misfit dislocations can be observed at the junction of Si buffer layer and substrate. However, Si buffer layer is grown thick enough so that these dislocations die out and a smooth Si surface is obtained before the deposition of SL structure. High resolution TEM images are also provided for each sample in order to showcase the quality of heterostructures so formed.

Fig. 4.4 & 4.6 represent the XTEM images of SG7 & SG16 respectively which are prepared by alternate deposition of Si and pure Ge at growth temperatures of

Sample	Bilayers	$T_G(^{\circ}\text{C})$	Dep. Rate	$x(\text{Ge})$	Si:Ge thickness
SG7	Si/Ge	400	0.5Å/s	1	70:20 Å
SG16	Si/Ge	550	1Å/s	1	110:20 Å
SG5	Si/SiGe	750	0.6Å/s	0.57	90:60 Å
SG6	Si/SiGe	750	0.4Å/s	0.34	260:150 Å
SG8	Si/SiGe	750	1Å/s	0.48	175:100 Å

Table 4.1: Table contains the Growth Parameters for the various multilayer samples.

400°C and 550°C (refer Table 4.1) respectively. Both the samples show strain relaxation by the formation of Ge-huts which are observed to be ‘inverted’. Stacking of these quantum huts in various layers is also evident. This quantum hut ordering in various layers allow elastic strain relaxation in these epitaxial layers. In SG16, the lowest four Ge layers are almost smeared out due to the intermixing occurring at a higher growth temperature of 550°C while in SG7, no such intermixing is observed.

Fig. 4.7, 4.8 and 4.9 show XTEM images of SG5, SG6 and SG8 respectively which are grown by alternate deposition of Si and SiGe alloy at 750°C with different deposition rates. As can be observed, these layers are highly uniform, completely pseudomorphic and do not show any kind of elastic or plastic relaxation. However, the strain relaxation in the form of interdiffusion at the interfaces cannot be denied. This will be further investigated by XRD study.

4.2.2 Raman scattering

Raman spectra were registered in backscattering geometry using Horiba Jobin Yvon 800 micro-Raman spectrometer. Measurements were performed at room

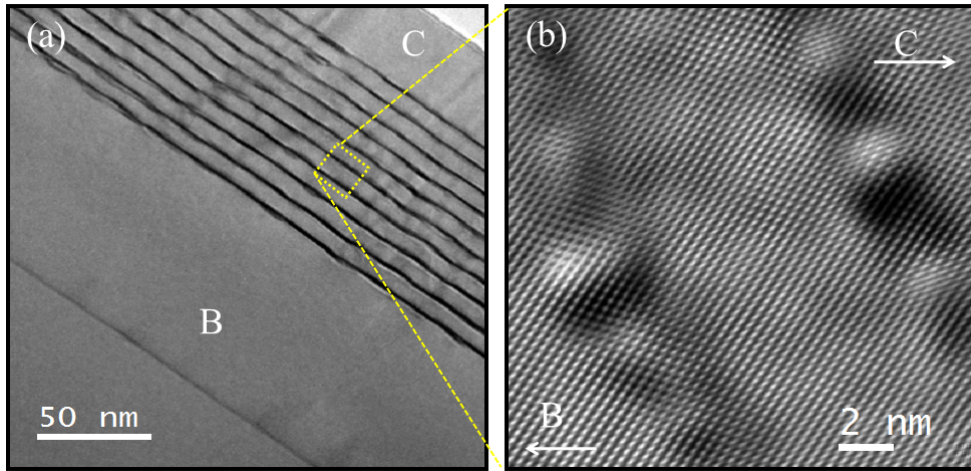


Figure 4.4: (a) and (b) XTEM and high resolution XTEM images for SG7. Dark lines correspond to the presence of pure Ge and lighter portion corresponds to Si.

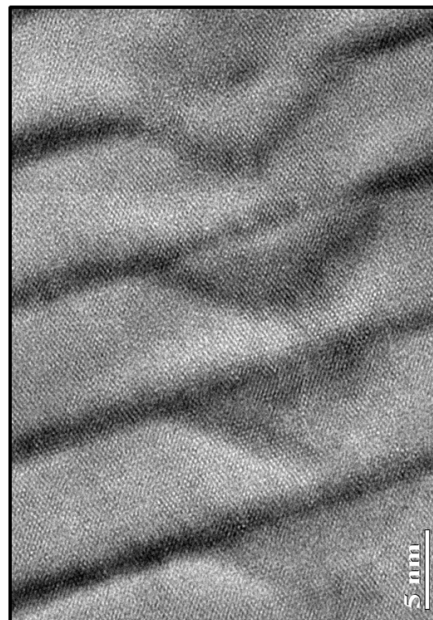


Figure 4.5: High resolution XTEM image of SG7 showing formation of inverted quantum huts.

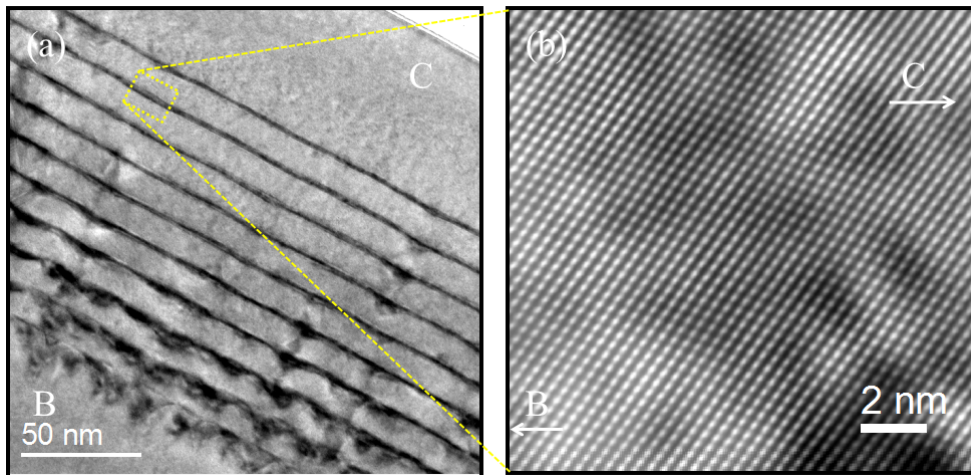


Figure 4.6: XTEM image for SG16. Lower Ge layers can be seen to have undergone large intermixing with the Si layers leading to strain relaxation in them. However, the upper layers do not show much intermixing. The superlattice sample consists of inverted Ge-huts which are stacked over one-another in various Ge-layers. Quantum hut stacking allows elastic strain relaxation in these epitaxial layers.

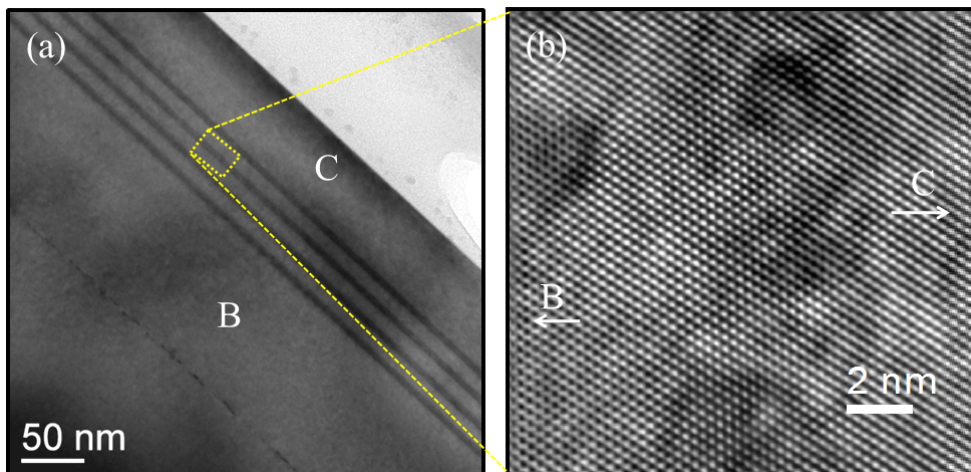


Figure 4.7: XTEM image for SG5. This sample consists of alternate Si and SiGe alloy ($x_{Ge} = 0.57$) layer. There is clearly no sign of elastic or plastic relaxation in these layers.

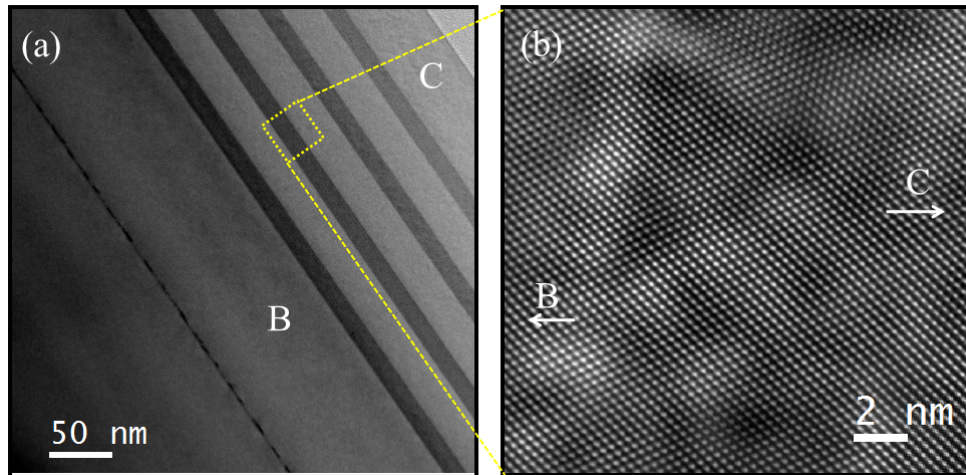


Figure 4.8: XTEM image for SG6. This sample consists of alternate Si and SiGe alloy ($x_{Ge} = 0.34$) layer. There is clearly no sign of elastic or plastic relaxation in these layers.

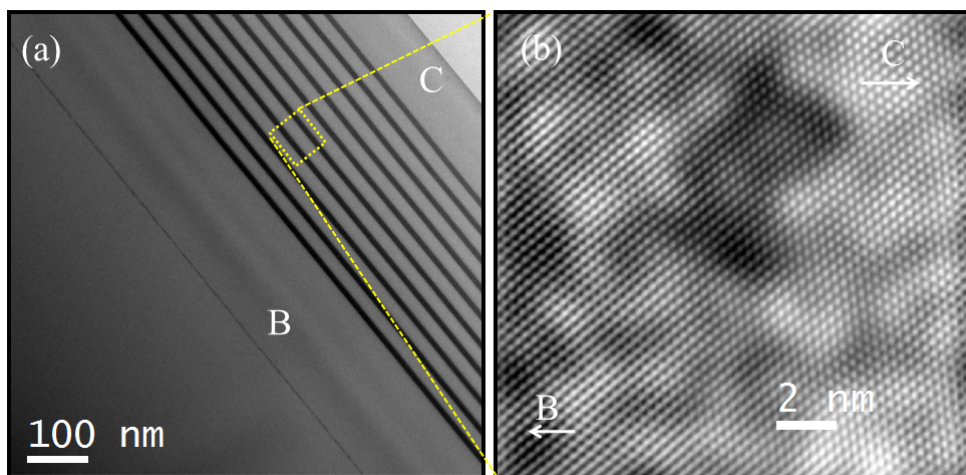


Figure 4.9: XTEM image for SG8. This sample consists of alternate Si and SiGe alloy ($x_{Ge} = 0.48$) layer. These are highly commensurate layers with no visible form of elastic or plastic relaxation.

temperature using an Ar^+ laser with a wavelength of 488 nm. The laser power was set at 6 mW so as to reduce the heating of the sample and the confocal-hole diameter was chosen to be $100 \mu\text{m}$. Each spectrum was taken for 60 s with 10 repetitions.

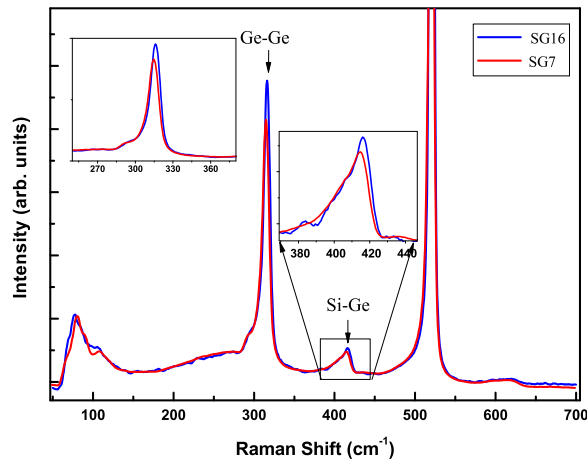


Figure 4.10: Raman spectra for pure Si/Ge superlattices. Insets show the zoomed-in peaks for Ge-Ge and Si-Ge modes.

Fig. 4.10 & 4.11 show the Raman spectra for Si/Ge and Si/SiGe superlattices respectively. The sharp peak at 520 cm^{-1} has the same frequency as that of the optical phonon peak in bulk Si. This suggests that this Si phonon peak originates from the Si substrate and the Si layers which are not strained. This peak presumably overshadows the Si mode at the $\sim 482 \text{ cm}^{-1}$ which is attributed to the localized Si-Si vibration in the neighborhood of one or more Ge atoms. The frequency of Ge-Ge mode for SG7 and SG16 is much larger than that of the optical phonon in bulk Ge (301 cm^{-1}). This can be explained by the presence of high strain in the Ge layers [51]. The Ge optical phonon frequency depends linearly

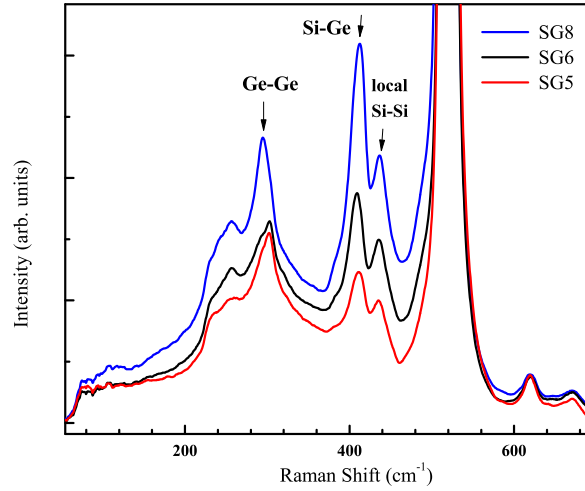


Figure 4.11: Raman spectra for Si/SiGe superlattices. The Si-Ge mode peak is highly pronounced due to very high alloy content in these superlattices.

on the deformation or on strain value. The strong peak around 415 cm^{-1} is the Si-Ge mode [52] attributed to the SiGe alloy which is formed at the layer interfaces. Apart from these three strong peaks, various other peaks are also observed, viz. at $\sim 435\text{ cm}^{-1}$, $\sim 595\text{ cm}^{-1}$ and $\sim 616\text{ cm}^{-1}$. The peak at 435 cm^{-1} is associated with scattering involving phonons along and near Σ for pure Si while that at $\sim 616\text{ cm}^{-1}$ is attributed to the combination of acoustic and optic phonons in Σ direction for Si [53]. The peak at $\sim 595\text{ cm}^{-1}$ is related to the second-order Ge-Ge mode [54, 55]. Since the intensity and frequency of this second-order Ge-Ge mode depends on the Ge content, it can be concluded that SG7 & SG16 contain high amount of pure Ge [51].

The compressive strain in the Ge layer causes the Raman shift frequency to move towards higher values. For full biaxial strain in Ge layer, the frequency

Constant	Value
a_{Si}	5.43095
a_{Ge}	5.64613
p	$-4.7 \times 10^{27} s^{-2}$
q	$-6.167 \times 10^{27} s^{-2}$
C_{11}	1288 kbar
C_{12}	482.5 kbar
ω_o	$0.564 \times 10^{14} s^{-1}$

Table 4.2: Table contains the values used for various constants during the strain calculation.

Sample	Ge-Ge peak	Ge peak width	Si-Ge peak	$\epsilon_{ }$	ϵ_{\perp}
SG7	314.6 cm^{-1}	9.78 cm^{-1}	415.02 cm^{-1}	-3.2%	2.39%
SG16	316.92 cm^{-1}	6.96 cm^{-1}	416.92 cm^{-1}	-3.6%	2.847%

Table 4.3: Table contains the Raman shift peak positions for Ge-Ge mode, Si-Ge mode, Ge-Ge mode peak width and the biaxial and longitudinal strain values.

of Ge-Ge phonons increases by 16 cm^{-1} which corresponds to the biaxial deformation $\epsilon = -0.04$ in the growth plane. The shift in Ge optical-phonon frequency induced by biaxial strain is given by [56–58]:

$$\Delta\omega_{strain} = \frac{p\epsilon_{\perp} + q(\epsilon_{xx} + \epsilon_{yy})}{2\omega_o} \quad (4.1)$$

where ω_o is the optical phonon frequency of the crystalline bulk Ge, p and q are the deformation potentials of the optical phonon in Ge and ϵ_{ii} are the diagonal elements of the strain tensor. The biaxial strain in the pseudomorphically grown Ge (or $\text{Si}_{1-x}\text{Ge}_x$) layers is given by:

$$\epsilon_{xx} = \epsilon_{yy} = \epsilon_{||} = \frac{a_{Si} - a_{Ge}}{a_{Ge}} \quad (4.2)$$

Sample	Ge-Ge peak	Si-Ge peak
SG5	302 cm ⁻¹	410.5 cm ⁻¹
SG6	303.3 cm ⁻¹	409.2 cm ⁻¹
SG8	294.7 cm ⁻¹	410.9 cm ⁻¹

Table 4.4: Table contains the Raman shift peak positions for Ge-Ge mode, Si-Ge mode for the alloy samples.

Strain in the z direction is related to the biaxial strain by: $\epsilon_{\perp} = -2C_{12}\epsilon_{\parallel}/C_{11}$ where C_{12} and C_{11} are components of the fourth rank elastic (stiffness) tensor. The numerical values of the various constants used in the calculations are given in Table 4.2.

A large shift in the Ge-Ge optical phonon frequency is obtained for the pure Si/Ge multilayers which signifies that the Ge layers in these samples are highly strained. However, for full biaxial strain the Ge-Ge phonon frequency is reported to be at 317 cm⁻¹ [59–61], it is found to be 314.6 cm⁻¹ and 316 cm⁻¹ for SG7 and SG16 respectively. The observed 1-3 cm⁻¹ less frequency shift signifies that the Ge layer is partially relaxed probably because of the alloy formation at the interfaces or nucleation of Ge to form islands (quantum dots). The observed shifts correspond to the biaxial deformation $\epsilon = -0.032$ and $\epsilon = -0.036$ for SG7 and SG16 respectively in the growth plane. This Ge-Ge mode peak in SG7 and SG16 have a peak width of ~ 9 cm⁻¹ and ~ 7 cm⁻¹ and ratio of the peaks of Ge-Ge mode to Si-Ge mode ($\Gamma_{Ge-Ge}^{peak}/\Gamma_{Si-Ge}^{peak}$) is ~ 7 . This shows that the two samples have a high Ge content in the layers. The very low peak width for Ge-Ge mode indicates that the variation in strain between different dot layers is small. A small shoulder (~ 295 cm⁻¹) has been observed for the Ge-Ge mode in both the Si/Ge

multilayers. This can be attributed to the SiGe intermixing at the layer interfaces or due to the relaxation of the Ge layer. Also, the Si-Ge mode peak around 410 cm^{-1} is seen to be larger for SG16 as compared to SG7. This indicates larger intermixing at the interfaces for SG16 as is also observed from XRD and XTEM study.

For Si/SiGe multilayers, the Ge-Ge mode peaks are found to be broad and near 301 cm^{-1} i.e. at 302 cm^{-1} , 303 cm^{-1} and 295 cm^{-1} for SG5, SG6 and SG8 respectively as tabulated in Table 4.4. A slightly higher Ge-Ge mode frequency for SG5 and SG6 signifies presence of low strain in the alloy layers, while 295 cm^{-1} value for SG8 represents complete relaxation of alloy layers. Due to the large presence of alloys in the samples, the Si-Ge alloy mode peak is seen to be significantly high.

4.2.3 XRD Study

XRD measurements were performed on all the pseudomorphic $\text{Si}_{1-x}\text{Ge}_x$ superlattice structures. The X-ray diffraction experiments were performed at the Indian Beamline, BL-18B at Photon Factory (PF), Japan. X-ray beam from the bending magnet of the PF storage ring was first focused horizontally with a focusing mirror and then monochromatized using a double crystal monochromator. The wavelength of the monochromatic X-ray used is 1.08887 \AA . The beam was then further collimated with a set of beam defining slits having horizontal opening of 1 mm and 0.1 mm in vertical direction. Sample was mounted on to an 8 circle goniome-

ter (Huber, Germany) at the focal point of the focusing mirror of the beamline. The sample was mounted horizontally and the scattered beam was collected by a single channel scintillation detector mounted at a distance of 380 cm on to the 2θ arm of the goniometer. A slit of 1.5 mm (horizontal) by 0.25 mm (vertical) was mounted just before the detector to increase the signal to background ratio. The slit settings were kept same for all the reflectivity, diffuse scattering and diffraction experiments. Fig. 4.12- 4.16 show the XRD profiles of the various samples around the Si(004) peak. These XRD profiles have been theoretically calculated using the Born Approximation method detailed in Section 3.1. While calculating the diffraction profile, the whole multilayer stack was considered to be divided into a number of layers having thicknesses equal to the lattice parameter at that point in the film. The lattice parameter varies in a multilayer stack according to the presence of either Si or Ge or SiGe alloy that form due to possible inter-diffusion. The obtained EDP for the multilayer stack from the XRR calculations can be decomposed to Ge and Si profiles where the fraction 'x' (Ge content) as a function of depth can be identified. Hence, for a $\text{Si}_{1-x}\text{Ge}_x$ system, the lattice constant can be calculated using the modified Vegard's law [62] given by:

$$a = xa_{\text{Ge}} + (1 - x)a_{\text{Si}} - 0.007((2x - 1)^2 - 1) \quad (4.3)$$

For calculating the XRD profiles of these multilayer samples, initial inputs are taken from the MBE growth parameters i.e. the nominal thicknesses of the various layers and the fraction (x) of Ge in the alloy layers. Then, the fitting of

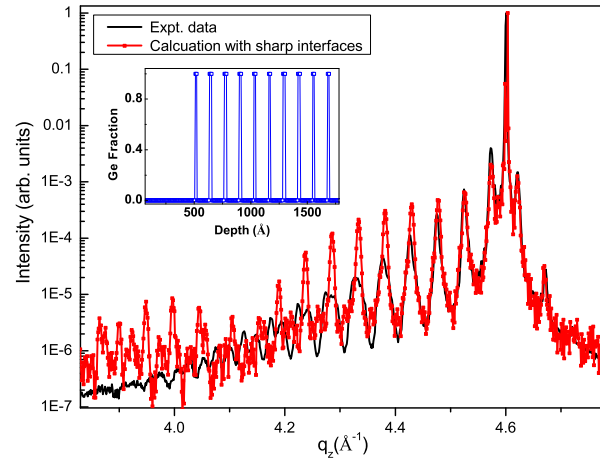


Figure 4.12: The black curve is experimental XRD profile of SG16 and red curve is the calculated diffraction profile by taking sharp interfaces i.e., no interfacial alloying. Inset shows the variation of Ge content with depth. Clearly, the calculation doesn't fit the experimental data.

the experimental XRD profile is performed by varying the layer thicknesses and introducing alloy layers with linearly varying Ge concentration at the interfaces. The obtained final structural profile i.e., fraction of Ge content as a function of depth, is shown in the respective insets. The various fitting parameters for all the profiles are given in Table 4.5. It is to be noted here that SL period in a sample is not perfectly constant over the whole multilayer stack, but a variation of 0.5-1 nm is observed.

By MBE growth, the interfaces are generally considered to be atomically sharp, however this is not the case as interfacial alloying always takes place at the growth temperatures usually used for sample preparation. To check the effect of alloying on the fitting profile, we did the XRD profile fit calculations by two ways.

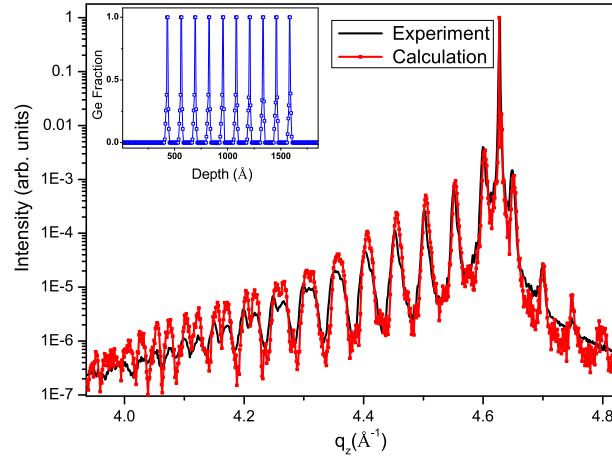


Figure 4.13: Experimental and calculated x-ray diffraction profile for SG16. Inset shows the Ge content as a function of depth. The interfaces are taken to as intermixed with a linear variation in the Ge content.

First we did not take the alloying into consideration and tried to do the XRD profile fit. Fig. 4.12 shows the XRD profile of SG16 along with the simulated profiles in which no alloying was considered at the various Si/Ge interfaces. The nominal thicknesses of 100 and 20 Å for Si and Ge layers respectively were used for the calculations. It can be seen that the calculated profile doesn't match with the data. Then, we did the same XRD profile fit by taking account of the intermixing at the various interfaces which is shown in Fig. 4.13. An alloy layer of thickness 22 Å was inserted at the Si-on-Ge interface (which is represented by t_1) where the Ge fraction was taken to be varying linearly having a slope of 0.015 (represented by m_1). The average Ge concentration of this intermediate alloy layer is found to be $x = 0.2043$. For the Ge-on-Si interface, an alloy layer of thickness (t_2) varying from 11 to 20 Å was inserted for the various layers where the Ge fraction varied linearly with a slope of ($m_2 =$) -0.0225. The average Ge concentration of this

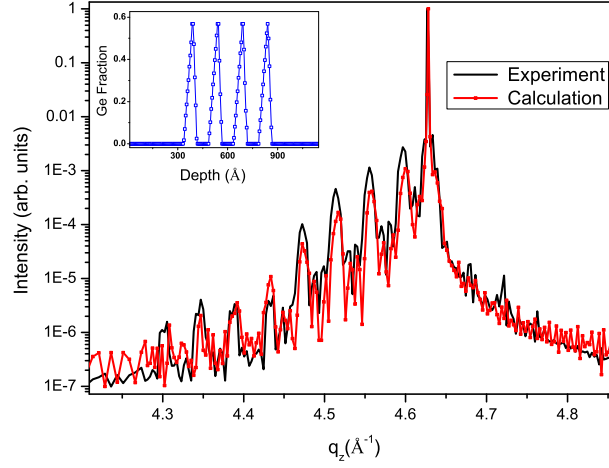


Figure 4.14: Experimental and calculated x-ray diffraction profile for SG5. Inset shows the Ge content as a function of depth.

intermediate alloy layer is found to be $x = 0.22$. Subsequently, the Si and Ge layer thicknesses changed to 90 and 8 Å respectively in order to accommodate the alloy layers. All these details have been tabulated in Table 4.5. It can be clearly seen that consideration of alloyed interfaces give a good fit to the data. Hence, intermixing at the Si/Ge interfaces does occur.

Similarly, XRD profiles were fit for the Si/SiGe alloy multilayer samples SG5, SG6 and SG8 as shown in Fig. 4.14, 4.15 and 4.16 respectively. SG5 and SG6 consist of 4 Si/Si_{1-x}Ge_x bilayers while SG8 has 10 Si/Si_{1-x}Ge_x bilayers. These alloy superlattice structures were grown at high temperature ($\sim 750^\circ\text{C}$) and the composition of SiGe alloy layers are Si_{0.43}Ge_{0.57}, Si_{0.66}Ge_{0.34} and Si_{0.52}Ge_{0.48} for SG5, SG6 and SG8 respectively. The nominal alloy-layer/Si-layer thicknesses for these superlattice samples were 60/90 Å, 150/260 Å and 100/175 Å respectively. For XRD profile calculation, intermixing at the various interfaces was taken into

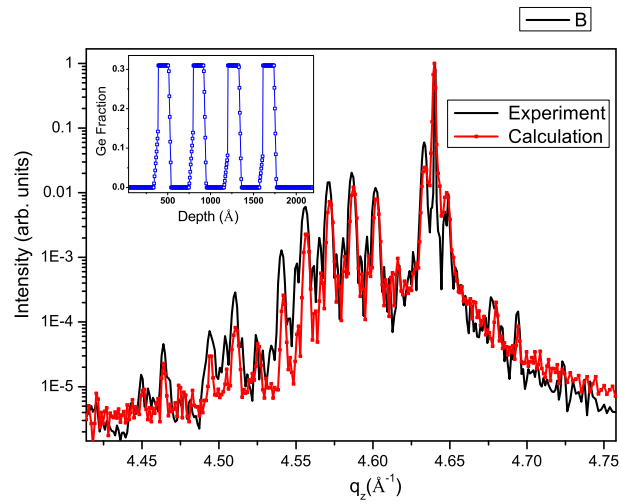


Figure 4.15: Experimental and calculated x-ray diffraction profile for SG6. Inset shows the Ge content as a function of depth.

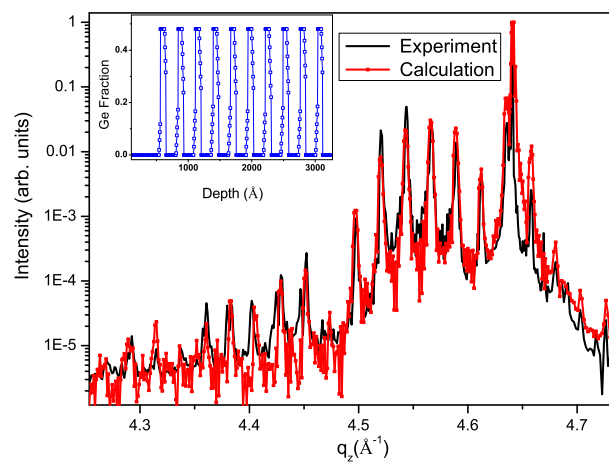


Figure 4.16: Experimental and calculated x-ray diffraction profile for SG8. Inset shows the Ge content as a function of depth.

account and it was observed that the Si-on-Ge interface shows intermixing upto 50 Å with average Ge fractions of ($x =$) 0.25 and 0.076 for SG5 and SG6 while it is 30 Å with ($x =$) 0.098 for SG8. For the Ge-on-Si interface, the intermixing upto 20, 30 and 25 Å with average Ge fractions of ($x =$) 0.28, 0.17 and 0.348 were observed for SG5, SG6 and SG8 respectively.

Sample	Si:Ge(Å)	t1, t2(Å)	m1, m2	x_{Ge} (Si-on-Ge)	x_{Ge} (Ge-on-Si)
SG16	90:8	22,11-20	0.015, -0.022	0.20	0.22
SG5	70:10	50,20	0.006, -0.015	0.25	0.28
SG6	210:120	50,30	0.002, -0.006	0.08	0.17
SG8	155:65	30,25	0.004, -0.005	0.1	0.35

Table 4.5: Table contains the Growth Parameters for the various multilayer samples and the fitting parameters used for XRD simulation. T_G is the growth temperature for various samples. t1 & t2 and m1 & m2 are the alloy thicknesses and the slope of linear profile considered (for the concentration of Ge variation in alloy) at the Si-on-Ge interface and Ge-on-Si interface respectively. The alloy layer thicknesses (t1 and t2) are excluded from Si and Ge layer thicknesses.

4.3 Interfacial intermixing and strain

X-ray scattering techniques can provide us information regarding chemical composition and strain [76] distribution of such heterostructures non-destructively [63, 65, 67–70, 98, 142].

The Si/Ge multilayer sample taken first for detailed study here has a stack of 10 bilayers and a Si(001) substrate, shown schematically in Fig. 4.17. The sample is represented by name ‘SG7’. Its XTEM image is shown in Fig. 4.4(a). From high resolution XTEM image [shown in Fig. 4.4(b)], it can be observed that the multilayer sample is free from any plastic dislocations and the multi-

layer system shows relaxation in the form of 3-D islanding (which is very low in number density). The X-ray reflectivity, diffuse scattering and the diffraction experiments were performed at the Indian Beamline, BL-18B at Photon Factory (PF), Japan. The experimental conditions were the taken to be same as described in section 4.2.3.

4.3.1 Electron density profile

The analysis of X-ray reflectivity data of Si/Ge multilayer samples were done using DWBA technique [71, 72]. In this DWBA formalism, we consider the EDP of a multilayer stack as $\rho_0 + \Delta\rho(z)$ where ρ_0 is the average electron density (AED) of the multilayer film (including the cap layer at the top and part of the buffer layer at the bottom) and $\Delta\rho(z)$ is the perturbation in electron density (ED) of the film as a function of z . $\Delta\rho(z)$ takes positive and negative values at Ge and Si positions respectively. The total multilayer film thickness is divided into N thin boxes of equal thickness d and the parameter to be determined is $\Delta\rho_i$, where i corresponds to the i^{th} box from the top, $z = 0$. Then, the fourier transform of $\Delta\rho(z)$ can be written as (refer section 3.2.2):

$$\Delta\rho(q_z^{mf}) = \int_{-\infty}^{\infty} \Delta\rho(z) \exp(iq_z^{mf}z) dz \quad (4.4)$$

After expanding in terms of $\Delta\rho_i$ noting $\Delta\rho(z) = \sum_{i=1}^N \Delta\rho_i$

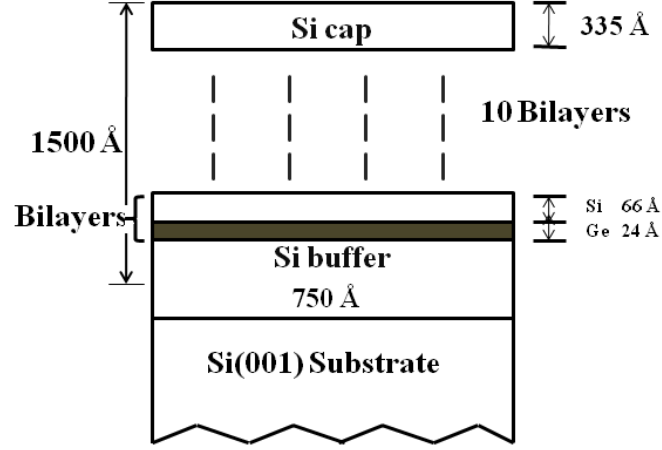


Figure 4.17: Schematic representation of the Si/Ge 10 bilayer superlattice on Si(001). The thicknesses are nominal as obtained from the MBE growth conditions. The total thickness of the multilayer structure was taken as 1500 Å for XRR analysis.

$$\Delta\rho(q_z^{mf}) = \frac{i}{q_z^{mf}} \left[\left(\sum_{j=2}^{j=N} (\Delta\rho_j - \Delta\rho_{j-1}) \exp(iq_z^{mf}(j-1)d) \right) + \Delta\rho_1 - \Delta\rho_N \exp[iq_z^{mf}Nd] \right] \quad (4.5)$$

where q_z^{mf} is the z-component of momentum transfer in the multilayer film and is given as $2(k^2 - k_c^2)^{\frac{1}{2}}$. Here, $k = 2\pi \sin\theta/\lambda$ is the wave vector for the angle θ and k_c is the critical wave vector at critical angle θ_c for the average film with AED ρ_0 .

The above expression for $\Delta\rho(q_z^{mf})$ is used to calculate specular reflectivity by Distorted Wave Born Approximation given by [71, 72]

$$R(k) = \left| ir_0(k) + \frac{2\pi b}{k} (a^2(k)\Delta\rho(q_z) + b^2(k)\Delta\rho^*(q_z)) \right|^2 \quad (4.6)$$

where $r_0(k)$ is the specular reflectance coefficient of the multilayer film with AED ρ_0 , $a(k)$ and $b(k)$ are the coefficients for the transmitted and reflected amplitudes in the average film. While analyzing the specular X-ray reflectivity data, the diffuse background (measured through longitudinal diffuse scans) was subtracted to obtain true specular reflectivity. Fig. 4.18 shows the measured and fitted X-ray reflectivity profiles for the 10 bilayer sample. Here, the total thickness of multilayer stack was taken as 1500 Å which includes the top cap layer and part of the buffer layer. This total thickness was divided into 300 boxes, each having a thickness of 5 Å. Taking average electron density (ρ_0) as 0.73, these 300 boxes were then given an initial approximation of $\Delta\rho(z)$ according to the nominal profile (refer Fig. 4.17) expected from MBE growth parameters of the 10 bilayer sample. The profile $\Delta\rho(z)$, was allowed to vary to fit the measured data using a computer program based on the DWBA method. The EDP obtained from this fitting process is shown in the inset of Fig. 4.18 which shows a clear signature of ten Si/Ge bilayers. The presence of higher electron density structure in the EDP of capping layer indicates Ge-segregation occurring during capping process, as observed earlier [73]. A dip in the electron density at the interface between buffer layer and multilayer stack can also be observed. This can be due to the presence of residual vacancies present at this interface. As X-ray reflectivity provides statistical information over large area, these vacancies may play a role in the electron density lowering.

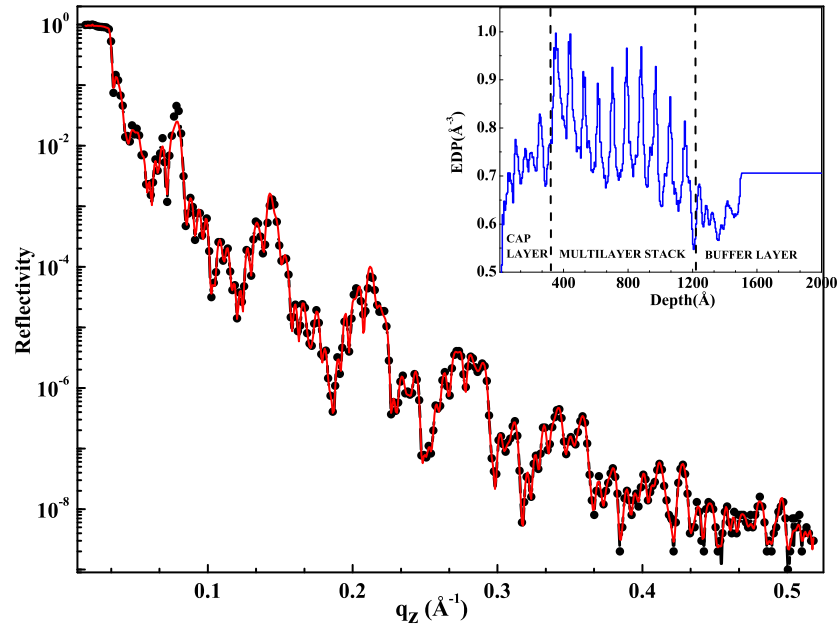


Figure 4.18: The measured X-ray reflectivity curve of the Si/Ge 10 bilayer stack is shown by black filled circles. The red line represents the fitted reflectivity curve obtained by DWBA method. Inset shows the obtained EDP of the studied Si/Ge multilayer system containing 10 bilayers.

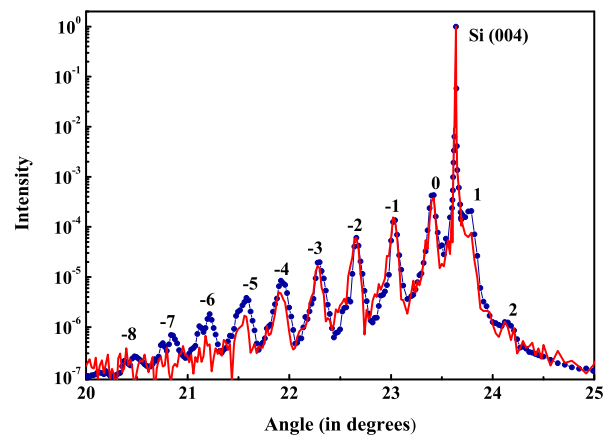


Figure 4.19: The measured X-ray diffraction profile of the sample is shown in black filled circles and the red line shows the generated profile obtained by Born's Approximation. The highest peak corresponds to the substrate Si(004). The numbers represent the order of superlattice satellite peaks.

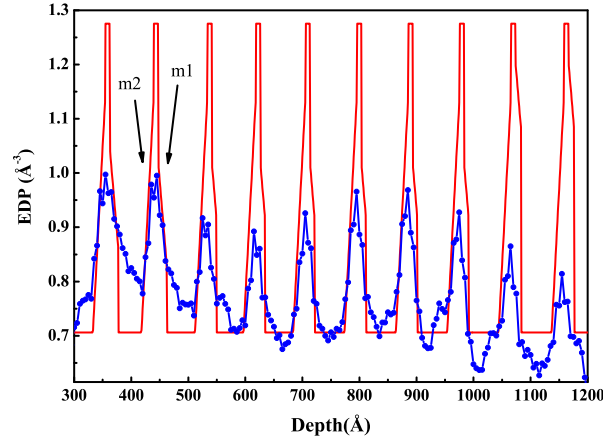


Figure 4.20: Figure shows the electron density variation in the multilayer stack. The blue curve shows the EDP obtained from X-ray reflectivity calculations and red curve shows the structural profile obtained from the fitting of XRD data.

4.3.2 Strain profile

Fig. 4.19 shows the X-ray diffraction profile of the sample around the Si(004) peak of the substrate. The satellite peaks (-8, -7, ..., -1, 0, 1, 2) arise due to the superlattice structure (Si/Ge multilayer stack) having a finite periodicity. The satellite marked '0' is the average superlattice peak and rest are the higher-order satellite peaks. The lattice parameter corresponding to the '0th' satellite peak is 5.479 Å which leads to an average +0.88% strain in the superlattice structure [74]. A strong asymmetry can be seen in the diffraction pattern showing stronger satellite peaks on the lower angle side of the Si(004) peak. This asymmetry can be attributed to the positive integrated strain in the superlattice structure [75]. The superlattice periodicity can be easily calculated using the simple relation $D = 2\pi/\Delta q_z$, where Δq_z corresponds to the spacing between the adjacent satellite peaks. For

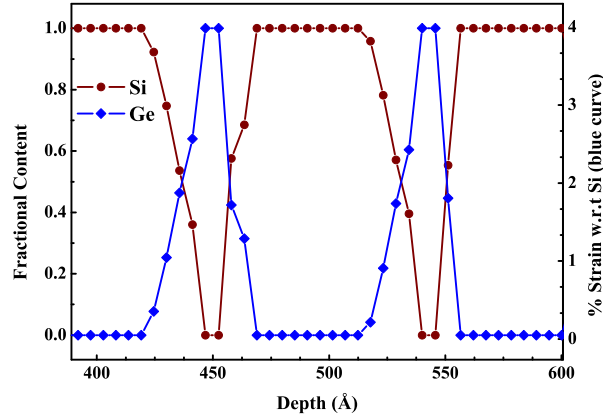


Figure 4.21: Left axis shows the variation in fractional content of Si and Ge in the second and third bilayers. Fractions of Si and Ge have been represented by red and blue curves respectively. The right axis shows the % strain with respect to Si (consider blue curve) in the second and third bilayers of the superlattice stack.

the present sample, this bilayer periodicity is found to be $\sim 90\text{\AA}$ (refer schematic Fig. 4.17).

For calculating XRD pattern (refer Eqn. 3.10) shown in Fig. 4.19, the EDP obtained from XRR measurements was used. From this EDP, the fraction of Ge was calculated (using the Vegard's law) and hence, lattice parameter for the Si-Ge alloy was obtained by modified Vegard's law (Eqn. 4.3). In this way, the whole multilayer stack was divided into boxes having thicknesses equal to the lattice parameters as a function of depth. The scattering amplitude for each of these boxes was taken as the weighted average of scattering amplitudes of Si and Ge. It is to be noted here that EDP obtained from XRR analysis include X-Y averaged information of Si-Ge layers and presence of interfacial roughness and miscut steps [77] make the contrast between electron density of Ge and Si much weaker. We

assumed that peak positions of electron densities in EDP correspond to a layer of Ge in the initial guess of structural profile to fit XRD data. The obtained final structural profile is shown in red in Fig. 4.20 along with EDP obtained from XRR. It is interesting to note that we obtained pure Ge layer of 8 Å in each bilayer. Interfacial profile was approximated by linear functions (refer Fig. 4.20). The slope (m1) of Ge-over-Si was found to be 0.0125 and slope (m2) of Si-over-Ge was found to be 0.02. It is observed that the diffusion at Si-over-Ge interface is higher as compared to Ge-over-Si. The thickness of Si-over-Ge interface was found to be 22 Å. The width of Ge-over-Si interface was varied keeping 'm1' constant. We have found that top two Ge-over-Si interfaces are about 15 Å thick as compared to 8 Å thickness of the similar buried interfaces. The obtained chemical composition (fractional content of Si and Ge) and strain profile of deposited Ge layers (with respect to Si lattice parameter) obtained from the structural profile (refer Fig. 4.20) is shown in Fig. 4.21.

4.3.3 Summary of results

The growth of Ge on Si (and vice versa) leads to alloy formation at the interfaces. This alloying reduces the misfit between the lower layer and the deposited material. Interfacial alloying mainly depends upon the chosen growth conditions, viz. growth temperature, deposition rate and composition of deposited material. From the Table 4.5, it can be seen that the Si on Ge interface consists of thicker alloy layer as compared to the Ge on Si interface. This can be attributed to the fact

that Si has lower mobility than Ge i.e. Ge can diffuse to larger distances than Si. When Si is deposited on the Ge layer, a fairly good amount of intermixing is seen which is mainly due to the Ge segregation [78]. The Ge segregation phenomenon varies with the growth temperature, being maximum at 450°C and lower at other temperatures. It is also inversely dependent upon the rate of deposition of Si layer on Ge i.e. higher Si deposition rate leads to lower Ge segregation and hence lower intermixing [78].

From the Table 4.5, it can be seen that Si on Ge interface has same thickness for both SG7 and SG16. However, SG7 has lower interfacial alloy layer thickness of 8 Å for Ge on Si interface as compared to SG16 whose alloy layer thickness varies from 11 to 20 Å for different Ge on Si interfaces. Also, alloy composition is seen to be different for the two samples, which is due to different growth conditions. SG16 was grown at higher temperature (550°C) than SG7 (growth temperature 400°C) and deposition rate was also kept to be higher for SG16. Due to high growth temperature for SG16, a large amount of interfacial alloying is observed mainly in the lower layers. A much larger interfacial mixing is observed for the alloy multilayers as compared to the pure Si/Ge samples as alloy layer thickness for Si-on-Ge interface is seen to be of the order of 30-50 Å and that for Ge-on-Si interface being 20-30 Å. These alloy multilayers were grown at same temperature of 750°C with a variation in deposition rate. As observed from Table 4.5, these multilayers have quite high intermixing at the interfaces, the layers have relaxed elastically and can be considered as perfectly epitaxial with almost

no plasticity or dislocations present. Whereas the thickness of Ge on Si interface is almost similar (20-25 Å) in all the three alloy multilayers, Si on Ge interfacial alloy thickness shows a sharp fall to 30 Å (from 50 Å for SG5 & SG6) for SG8. This may be attributed to the higher deposition rate for SG8.

4.4 Conclusion

The dependence of interdiffusion and mode of strain relaxation in Si/Ge superlattices on the growth parameters has been studied in detail. A variety of MBE grown Si/Ge and Si/SiGe superlattice structures to determine the intermixing at various interfaces in a sample. These samples were prepared at different growth conditions. Hence, this study provides a dependence of intermixing on the growth parameters. It is shown that how by choosing proper growth conditions, one can move from Si/Ge multilayer system which consists of large misfit dislocations to a Si/Ge superlattice system with negligible plastic dislocations. Cross-sectional TEM study provides us with the information on the mode of strain relaxation acquired by the superlattices with variation in growth conditions. Raman scattering from these superlattices leads to the information about the average strain present in the Ge layers in the system.

Although, XTEM gives a local picture of the system, X-ray diffraction provides statistically averaged information about the alloying at the various interfaces. This interfacial intermixing is found to increase with the growth temperature and decrease as the deposition rate is increased. X-ray reflectivity and X-ray

diffraction techniques are used together for the morphological and structural characterization of the Si/Ge multilayer system. The EDP obtained from the reflectivity and compositional (and associated strain) profile obtained from diffraction are in good agreement. Grazing incidence diffraction study of (400) and (800) peaks to understand the nature of quantum dot structures in these type of multilayer structure will be presented next. Nevertheless, consistent analysis of specular reflectivity and specular diffraction profile presented here provided us valuable structural information as a function of depth.

Chapter 5

Quantum Structures in SiGe

Superlattice

Ge quantum structures embedded in Si-Ge superlattice systems have already exhibited remarkable photoluminescence properties [17, 84–87, 109]. The developments in electron microscopy and synchrotron x-ray scattering techniques have enabled us to understand the growth mechanism by which these Ge quantum structures form in each Si-Ge interface over the Ge wet-layer with the apex pointing towards the top surface and get ordered vertically in a Si-Ge superlattice due to propagation of strain. This chapter deals with the study of the formation of Inverted Quantum Hut (IQH) structures which form in the SiGe superlattice structure at low growth temperatures. Consistent results of XTEM, GID and out-of-plane XRD provide a simple model to explain the growth mechanism of these IQH.

5.1 Formation of Inverted Quantum Huts

Although Si and Ge can form alloys in any molar ratio, it is well known that Ge deposited on Si(001) surface grows layer by layer for around three monolayers in a typical temperature range of 450-750°C, which is used for molecular beam epitaxy (MBE) growth, as barriers to interdiffusion are sufficiently high [88–90]. By scanning tunneling microscopy studies, it has been shown that after one monolayer (ML) of Ge deposition, surface dimerization introduces nonuniform stress fields in the subsurface regions [88, 138]. Hence, the sites, which are under compressive stress, would prefer Si occupancy while those under tensile stress would favor Ge. Thus, given sufficient kinetic energy, Ge tends to move to the tensile sites which lie in the third or fourth subsurface layers in order to lower the overall surface energy [88]. In this temperature regime of MBE growth, the Ge interdiffusion into the Si layer, even with added driving force of stress, is negligible. For two monolayer coverage of Ge, less than one-fourth of a layer goes in the underlying Si(001) lattice [17, 88–90, 138]. After a critical thickness of three monolayers of Ge, quantum hut structures are formed on top of this Ge wet layer with the tip pointing towards the top surface.

It is expected that as the growth temperature is reduced ($\leq 500^\circ\text{C}$) the interdiffusion of Ge into the underlying Si lattice will become even lower. But on the contrary, it was observed recently by electron microscopy studies that surprisingly large length-scale interdiffusion of Ge occurs in the underlying Si layers at low growth-temperatures ($\sim 450^\circ\text{C}$), provided the deposited Ge layer thickness is

kept in between 22 to 38 Å [92–94, 138]. This enigmatic interdiffusion of Ge in the underlying Si lattice at lower growth-temperature ($\leq 500^\circ\text{C}$) leads to the formation of quantum hut structures within the Si sub-layer below the Ge wet layer with the apex pointing down towards the Si substrate.

It is shown that the deposited Ge layer relaxes strain by uniform intermixing with the previously deposited lower Si layer to form a $\text{Si}_{0.6}\text{Ge}_{0.4}$ wet layer exhibiting an out-of-plane lattice parameter of 5.64 Å and an in-plane lattice parameter close to the Silicon value of 5.43 Å. The IQH structure forms with its base just below the wet layer. The anomalous x-ray scattering measurements show interesting composition variation of IQH structure from base to tip. A simple model calculation showed that the in-plane structure of IQH can be understood as a stack of layers with each layer having a constant in-plane lattice parameter with laterally varying [95] composition. Compositional variation over large length-scale was observed near the base of the IQH structure with in-plane and out-of-plane lattice parameters around 5.44 Å and 5.57 Å respectively. The rim of the IQH structure approaches an alloy composition of $\text{Si}_{0.7}\text{Ge}_{0.3}$ in all the isostructural stacks of layers from base to tip having in-plane lattice parameters varying from 5.44 to 5.52 Å. Near the tip region of the IQH structures both in-plane and out-of-plane lattice parameters become 5.52 Å. This value of the out-of-plane lattice parameter in the rim and tip region of the IQH is around 1.66% higher than the Si(001) lattice parameter and can get accommodated in the surrounding Si-lattice as the critical thickness [17] of such lattice parameter on Si can be around 100 Å, which

is higher than the Si-layer thickness used here.

5.2 Experimental Details

In anomalous x-ray scattering measurements, two data sets are collected away from and at the x-ray absorption edge of a particular material to increase the sensitivity of the x-ray scattering technique. In this study, measurements at the Ge K-edge (11 103eV) and away from it (11 043 eV) to determine shape, composition and strain of Ge IQH structures embedded in a Si-Ge superlattice [98–100] were carried out. X-ray measurements were performed both at beamline [101] P08 of the synchrotron radiation source PETRA III, DESY, Germany and at the Indian beamline [102] BL-18B, Photon Factory, KEK, Japan. The monochromatic beam in BL-18B at Photon Factory, was collimated with a set of beam defining slits having horizontal opening of 1 mm and 0.1 mm in vertical direction and data collection was done by a Cyberstar scintillation detector. For all the diffraction measurements a slit of 1.5 mm (horizontal) by 0.25 mm (vertical) was mounted just before the detector to improve the signal to background ratio. At beamline P08 of Petra III, a beam-defining slit setting of dimension 50 by 300 μm was used in vertical and horizontal direction respectively and the data was collected by a position sensitive linear Mythen detector. For grazing incidence diffraction (GID) measurements, the intensity of all the channels was integrated to obtain the data presented here, whereas for XRD measurements a central region of interest (40 pixels) was integrated. During GID measurements the incident angle was kept to

be 0.2° , slightly above the critical angle for Si, to allow the x-ray beam to penetrate the Si cap layer for probing the underlying Si-Ge superlattice. Radial and angular scans were taken around two in-plane diffraction peaks i.e. around (400) and (800). The XTEM investigations were carried out using a FEI, Tecnai G2 F30, S-Twin microscope operating at 300 kV. HAADF-scanning TEM was employed here using the same microscope, which was equipped with a scanning unit and a HAADF detector from Fischione (Model 3000). Cross-sectional TEM specimens were prepared using mechanical thinning down to $20\ \mu\text{m}$ followed by 2kV Ar-ion milling.

5.3 Results and Discussion

Fig. 5.1(a) shows a typical high-angle annular dark field scanning/ transmission electron microscopy (STEM-HAADF) image of a representative superlattice sample (SG7 as shown in section 4.3) and the line across the layers (over the IQH stack) is the profile path for STEM-energy dispersive x-ray (EDX) measurements. The Si and Ge profiles along the line from the Si buffer (top) to the cap layer (bottom) are shown in Fig. 5.1(b). It can be easily observed that the variation of Si concentration as a function of depth is exactly opposite to that of the Ge concentration as expected. Fig. 5.1(c) shows the same Ge EDX profile using bars of equal thickness ($\sim 13\ \text{\AA}$) over the lowest three Si-Ge bilayers. Since on average four bars are present on the buffer side while only two are on the cap side, obviously the slope of the Ge concentration on both sides of the wet layer are different.

The observed small slope of the Ge-over-Si interface is due to the presence of IQH structures. It is to be noted that during the occurrence of all this diffusion, proper epitaxy of the heterostructure is maintained and high resolution TEM studies have revealed the absence of any plastic relaxation in the system. Hence, even though the Ge diffusion is not random and occurs making a slope with the wet layer to form the observed IQH structure, the theory of elasticity applies in this system.

It is known that the Ge wet layer on a Si(001) surface has an inherent biaxial compressive strain in the growth plane that leads to tensile strain in the out-of-plane direction [17]. The anomalous GID measurements around the (800) and (400) diffraction peaks provide us direct information regarding strain in the in-plane lattice with respect to the Ge composition profile [98]. The composition and strain information obtained from these GID measurements was used in the analysis [102] of the out-of-plane diffraction data to obtain detailed knowledge about the composition-strain profile of these superlattice systems.

5.3.1 In-plane Structure

Radial and angular scans in the GID measurements were carried out. Radial scans are intensity measurement by varying the incidence angle (θ) to the in-plane lattice and the detector angle (Φ) position by keeping $\Phi = 2\theta$. The measured x-ray intensity can be directly related to the in-plane lattice parameter ($a_{||}$) as $a_{||} = \lambda\sqrt{h^2 + k^2 + l^2}/(2\sin(\Phi/2))$, where (h,k,l) are the Miller indices of the nearest Bragg reflection. In angular scans θ is varied by keeping Φ (detector position)

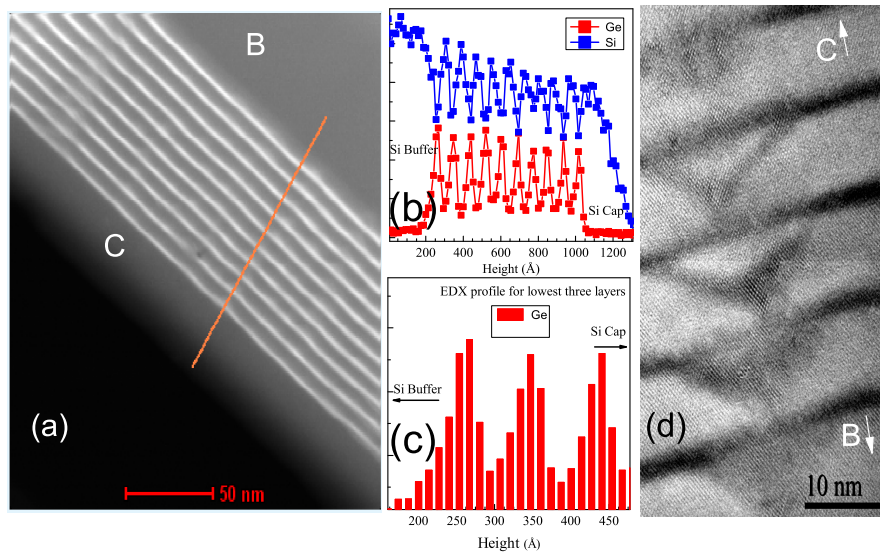


Figure 5.1: (a) STEM-HAADF image of the superlattice structure. Brighter lines correspond to Ge layers while the gray portions are Si. Buffer (B) and cap (C) layers are indicated. (b) STEM-EDX line profile along the line shown in (a). The line profile is taken over the IQH stack in various layers. (c) Ge EDX profile using bars of equal thickness (~ 13 Å) for the lowest three Si-Ge bilayers. (d) High-resolution XTEM micrograph of self-organized IQH structures formed in a Si-Ge superlattice sample. 'B' and 'C' indicate the location of buffer and cap layer respectively.

value constant and the measured x-ray intensity gives the size of the region in the sample having a fixed in-plane lattice parameter corresponding to the fixed Φ position [$q_r = (4\pi/\lambda)\sin(\Phi/2)$]. It is to be noted here that only the angular momentum transfer [$q_a = (4\pi/\lambda)\sin(\theta - \Phi/2)$] changes in these scans while the radial momentum remains constant. Fig. 5.2(a) and (b) show typical GID two-dimensional radial scans of the superlattice sample shown in Fig. 5.1(a) at two energies around (800). At the Ge K-edge, the contribution of the Ge atomic scattering factor in the diffracted x-rays is much less [98–100] as compared to this contribution when the x-ray measurement is done away from the Ge K-edge. The reduction in Ge scattering at the x-ray edge leads to the reduction in the intensity of the diffraction peak as can be seen in radial scans of Fig. 5.2(c). Hence, by taking the ratio of intensities measured at two energies $E_1 = 11\,043\text{eV}$ (away from the Ge K-edge) and $E_2 = 11\,103\text{eV}$ (at Ge K-edge), one can calculate the Ge concentration corresponding to a lattice parameter ($a_{||}$) using the formula [98]

$$x = \left[1 + \frac{f_{Ge_2}\sqrt{I_1} - f_{Ge_1}\sqrt{I_2}}{f_{Si}(\sqrt{I_2} - \sqrt{I_1})}\right]^{-1} \quad (5.1)$$

where I_1 and I_2 are the scattered intensities and f_{Ge_1} and f_{Ge_2} are the atomic scattering factors at the energies E_1 and E_2 respectively and f_{Si} is the atomic scattering factor of Si that remains almost same at the two x-ray energies considered here. Ge composition from the analysis of the two radial scans for (800) as a function of the in-plane lattice parameter ($a_{||}$) and the result is plotted in Fig. 5.2(d). To determine the in-plane strain [$\varepsilon_{||} = (a_{||} - a(x))/a(x)$], one has to compare

the lattice parameter (a_{\parallel}) with $a(x)$ calculated from the Ge composition obtained from Vegard's law (refer Fig. 5.2(d)). In Fig. 5.2(e) the in-plane strain profile thus obtained as a function of a_{\parallel} is shown and from this plot we calculated (refer Fig. 5.2(f)) the out-of-plane lattice parameter a_{\perp} , using the Poisson's relation $a_{\perp} = -\frac{2C_{12}}{C_{11}}(a_{\parallel} - a(x)) + a(x)$ where C_{11} and C_{12} are the known components of fourth rank strain tensor related as $\varepsilon_{\perp} = -2\varepsilon_{\parallel}C_{12}/C_{11}$ [17]. It is to be noted here that the value of the ratio C_{12}/C_{11} changes from 0.385 to 0.372 as one use tabulated values of Si ($C_{11} = 1.66$ Mbar, $C_{12} = 0.64$ Mbar) and Ge ($C_{11} = 1.29$ Mbar, $C_{12} = 0.48$ Mbar). We have used values of Ge to extract the out-of-plane lattice parameter a_{\perp} approximately here as the measured data in out-of-plane direction was not found to be sensitive to this small variation. The sharp feature near the Si peak position (5.43 Å) was not used here for the composition and strain analysis as this portion of data is very sensitive to sample alignment and provide information primarily about the Si cap and Si buffer layers [103].

The in-plane and out-of-plane lattice parameters corresponding to the broad peak of Ge-concentration shown in the regions I and II of Fig. 5.2(d) represent the Ge wet layer. The peak composition of the wet layer is found to be close to $\text{Si}_{0.6}\text{Ge}_{0.4}$ with in-plane strain of around -2% as the a_{\parallel} becomes close to the Si lattice parameter (5.43 Å) and a_{\perp} approaching the value of 5.62 Å. Analysis of the out-of-plane diffraction data, which will be presented next, clearly shows that the thickness of this wet layer with $a_{\perp} = 5.62$ Å is around 15 Å. The interface of regions II and III ($a_{\parallel} = 5.44$ Å) represent the base of the IQH structure below

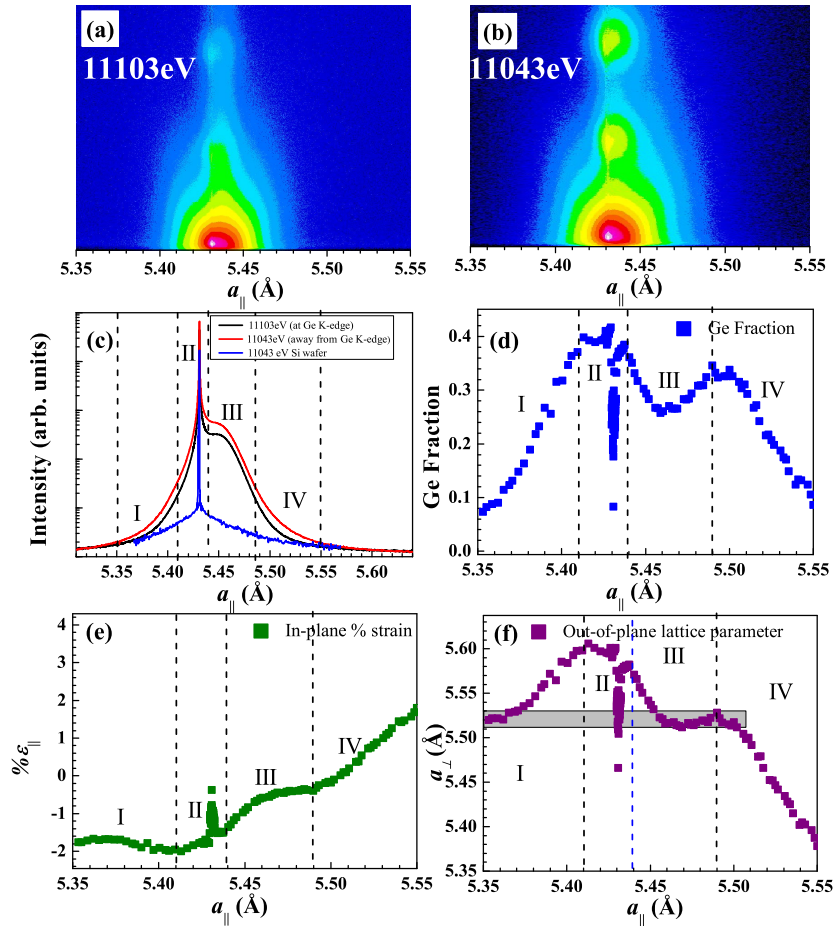


Figure 5.2: (a) and (b) show two-dimensional GID data of the superlattice sample shown in Fig. 5.1(a) at the Ge K-edge (11 103 eV) energy and away from it (11 043 eV) respectively around (800). (c) The extracted radial scans for the superlattice structure at the two energies as indicated, around (800). This plot is generated by integrating the counts on Mythen detector for each a_{\parallel} . Also shown is the (800) profile for Si substrate for comparison. (d), (e) and (f) Variation of Ge concentration, in-plane strain and out-of-plane lattice parameter respectively with the in-plane lattice parameter as obtained from (800) radial scans. Refer text for details about the shaded region in (f).

the wet layer and the second composition peak of Ge concentration $\text{Si}_{0.7}\text{Ge}_{0.3}$ [refer interface of regions III and IV of Fig. 5.2(d)] represent the tip of IQH. From Fig. 5.2(c) and 5.2(d), it can be seen that the Ge concentration becomes small as we approach a_{Ge} ($= 5.65\text{\AA}$) implying that pure Ge has not precipitated here. It shows that all the Ge atoms present in the system have intermixed with Si to form SiGe alloys. It is also clear from Fig. 5.1(a) and 5.1(d) that apart from the wet layer, Ge in alloy form is present only in the IQH structure and from the contrast of the TEM data it is apparent that the Ge concentration is higher in the rim area and tip portion of the IQH structure. It is to be noted here that a similar composition was detected in the rim and in the tip of IQH, in an earlier TEM study [92]. It is also clear from Fig. 5.2(f) that apart from regions II and I that represent the wet layer having peak composition of $\text{Si}_{0.6}\text{Ge}_{0.4}$ the out-of-plane lattice parameter a_{\perp} remains almost constant at the value of around $5.52 \pm 0.01 \text{\AA}$ (shown in shaded region) though the in-plane lattice parameter a_{\parallel} is changing from 5.35 to 5.52\AA . This shaded region can be attributed to the entire IQH structure. From the base of the IQH to its tip, the in-plane lattice parameter (a_{\parallel}) varies from 5.44 to 5.52\AA keeping the out-of-plane lattice parameter (a_{\perp}) constant at 5.52\AA . At the end of this shaded region, in the tip portion of the IQH, the composition becomes $\text{Si}_{0.7}\text{Ge}_{0.3}$ and the value of the in-plane lattice parameter a_{\parallel} also becomes close to 5.52\AA . This structure of the tip region of the IQH has nearly zero strain value [refer the interface of region III and IV of the in-plane strain profile shown in Fig. 5.2(e)]. The out-of-plane lattice parameter (a_{\perp}) of 5.52

Å in the tip and rim-structure helps accommodating the IQH in the Si-lattice with around 1.66% strain as compared to Si-lattice. It should be noted that the critical thickness for SiGe heterostructures with 1.66% strain is around 100 Å [17]. Very small amount of Ge present at the beginning of region I in Fig. 5.2(d) represents the Si-lattice in the vicinity of the IQH structure that match the out-of-plane lattice parameter 5.52 Å giving rise to $a_{||} = 5.313$ Å for Si. The Si lattice near the tip of the IQH structure needs to match the in-plane lattice parameter of 5.52 Å and that in turn requires $a_{\perp} = 5.36$ Å. This is because of the reason that formation of IQH structures leads to the tensile strain in the Si lattice in its vicinity and hence the in-plane lattice parameter increases which in turn leads to a decrease in the out-of-plane lattice parameter due to Poisson's law. This lattice is represented towards the end of region IV. However, for simplicity we have not used such an out-of-plane lattice parameter to fit the (004) data presented in the next section. An in-plane lattice parameter lower than that of Si (a_{Si}) was also observed earlier in a system consisting of pits [103]. From the strain profile of Fig. 5.2(e) it can be seen that with increasing $a_{||}$, the strain in $\text{Si}_{1-x}\text{Ge}_x$ moves from negative to positive values through zero and this represents different portions of the IQH structure. A similar behavior for strain i.e. changing from compressive to tensile for $a < a_{Si}$ and $a > a_{Si}$ respectively was observed in other SiGe quantum dot systems as well [103]. Propagation of such an oscillatory strain profile probably ensures that IQH structures get located on top of each other [refer Fig. 5.1(d)].

5.3.2 Out-of-plane Structure

The out-of-plane diffraction measurements allow to check consistency of the strain-composition profile obtained from the GID analysis and we show here the results of a typical analysis of data around the silicon (004) diffraction peak. Fig. 5.3(a) shows such XRD data taken at 11043eV along with the theoretically calculated profile [102], obtained with the Born approximation. For this calculation, a profile for a_{\perp} and a corresponding $\text{Si}_{1-x}\text{Ge}_x$ composition as obtained from GID measurements [refer Fig. 5.2(f) and 5.2(d)] was used. Thus, depending upon the composition, each lattice site was assigned with a scattering amplitude which was the weighted average of the scattering amplitudes of Si and Ge. The fitting of the experimental XRD profile is performed by varying the layer thicknesses and by introducing alloy layers at the interfaces through an iterative process. The final profile of a_{\perp} and the associated strain, defined as $\varepsilon_{\perp} = (a_{\perp} - a(x))/a(x)$, and the corresponding $\text{Si}_{1-x}\text{Ge}_x$ composition obtained from this fitting of the XRD data are shown in Fig. 5.3(b), 5.3(c) and 5.3(d), respectively. An expanded profile of one bilayer in the inset of each figure is also shown for clarity. The average out-of-plane lattice parameter, strain and composition of a typical Ge-Si bilayer are shown in these insets. The beginning of wet layer and end of the IQH structure is marked with arrows. The values obtained here are consistent with those obtained from the analysis of the in-plane GID data. The obtained profiles presented in these figures represent the data well. The top 330 Å of Si cap layer is completely relaxed with lattice parameter a_{Si} as expected from growth conditions.

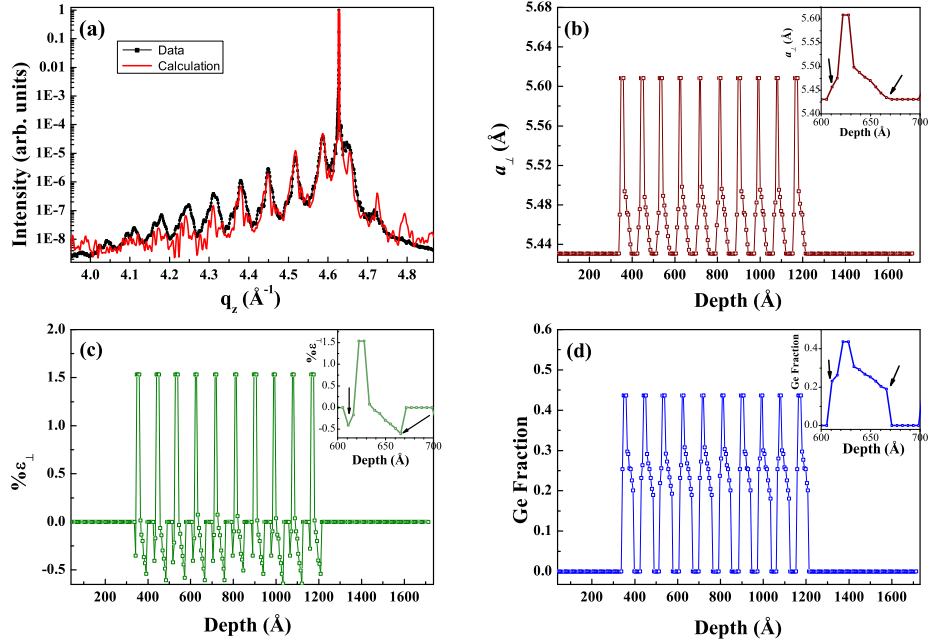


Figure 5.3: (a) Experimental data and calculated XRD profile of the superlattice structure. (b), (c) and (d) Variation in lattice parameter, out-of-plane strain (ε_{\perp}) and Ge fraction (x) respectively with depth as obtained from the XRD data analysis. Insets in (b), (c) and (d) show the expanded version of one bilayer for clarity.

The wet layer of the SiGe alloy has a thickness of around two to three unit cells (~ 15 Å) at all the interfaces and a large diffusion of up to five to six unit cells is seen below the wet layer. The Ge content (x) was found to vary (refer Fig. 5.3(d)) from zero for the Si cap and spacer-layers to around ($x = 0.4$) for the wet layer and the SiGe alloy composition in the IQH was found to be in between $\text{Si}_{0.7}\text{Ge}_{0.3}$ and $\text{Si}_{0.8}\text{Ge}_{0.2}$. Different regions in Ge layers are seen to be under both positive and negative out-of-plane strain [refer Fig. 5.3(c)] - these values were found to be consistent with the in-plane strain values obtained from the analysis of GID data [refer Fig. 5.2(e)].

5.3.3 Growth Mechanism

The analysis of the in-plane and out-of-plane x-ray data clearly shows that IQH structures embedded in Si-lattice have the following three distinct features, namely (a) the base of the IQH structure is just below the wet layer that has a $\text{Si}_{0.6}\text{Ge}_{0.4}$ composition with an out-of-plane (in-plane) lattice parameter of around 5.6 Å (5.4 Å) (b) the IQH structure has a rim and a tip both having a composition of $\text{Si}_{0.7}\text{Ge}_{0.3}$ and (c) the average out-of-plane (in-plane) lattice parameters just below the IQH structure and above the wet layer [marked as arrows in inset of Fig. 5.3(b)] are 5.43 Å (5.52 Å) and 5.46 Å (5.51 Å) with low Ge (< 0.2) concentration. Since the wetlayer has higher Ge content as compared to the base of IQH, the SiGe alloy lattice in IQH base tries to be commensurate with the wetlayer and hence suffers tensile strain in in-plane direction leading to higher lattice parameter in the in-plane direction as compared to the out-of-plane direction. In the growth model proposed here, it is assumed that the entire quantum structure of Ge from the wet layer to the IQH-tip, which almost touch the next wet layer below, is composed of in-plane iso-structural domains with increasing in-plane lattice parameter from region I to IV [refer Fig. 5.2(f)]. The domain size of the wet layer was found to be very large (~ 6000 Å) from the angular scan and the in-plane lattice parameter of the wet layer range from 5.375 Å to 5.435 Å [region I and II of Fig. 5.2(f)].

Fig. 5.4(a) and (b) show the typical angular scans taken with 11 043 eV and 11 103 eV x-ray beam around the (400) diffraction peak at various fixed radial positions corresponding to different in-plane lattice parameters $a_{||}$ as indicated in

each profile. The IQH structure can be considered to be consisting of a stack of disks with diameters, $D(a_{||}) (= 2R)$, having equal in-plane lattice parameter ($a_{||}$). Following the contrast of the XTEM image [refer Fig. 5.1(d)] and an earlier study [95] it is assumed here that in each of the disk the composition is not uniform laterally. Hence, during calculation a parabolic composition profile was assumed over the disk radially for the inner part and a constant Ge concentration ($\text{Si}_{0.7}\text{Ge}_{0.3}$) of thickness 20 \AA was taken for the rim structure. Thus, the x-ray scattering profile can be given as [95]:

$$I(q_a, R) = \frac{I_0}{\pi^2 R^4 |\langle f_{SiGe} \rangle|^2} \left| \int_0^{2\pi} \int_0^R e^{-iq_a r \cos(\theta)} f_{SiGe}(r) r dr d\theta \right|^2 \quad (5.2)$$

where f_{Ge} and f_{Si} are the atomic scattering factors for Ge and Si respectively. $f_{SiGe}(r)$ represents the scattering factor of the SiGe alloy at r and $\langle f_{SiGe} \rangle$ is the average scattering factor of the disk. The parabolic variation of the Ge fraction in the inner part is taken as:

$$C_{Ge}(r) = C_{Ge}(0) + [C_{Ge}(R) - C_{Ge}(0)]r^2/R^2 \quad (5.3)$$

The composition profiles for the different disks are shown in Fig. 5.4(c). It is to be noted that only the disk at the tip of the IQH has the maximum Ge-content ($\text{Si}_{0.7}\text{Ge}_{0.3}$) at the center and it decays as a parabola towards the edge of the disk. All other four disks have maximum Ge content ($\text{Si}_{0.7}\text{Ge}_{0.3}$) at the rim and mini-

mum at the center. The same model was used to fit the data collected at the two x-ray energies, at the Ge-edge and away from the edge. However, it was apparent from the XTEM images that there are variations of sizes particularly in the base portion of the IQH structure. Four profiles were used for the base region ($a_{||} = 5.44 \text{ \AA}$), each having the same composition profile but radii and relative strength (indicated in parenthesis) with respect to first one are as follows: 220 \AA (1), 116 \AA (0.35), 75 \AA (0.16) and 43 \AA (0.06); for $a_{||} = 5.46 \text{ \AA}$: 140 \AA (1), 87 \AA (0.55) and 58 \AA (0.25); for $a_{||} = 5.47 \text{ \AA}$: 120 \AA (1), 80 \AA (0.75) and 42 \AA (0.3); for $a_{||} = 5.49 \text{ \AA}$: 60 \AA (1) and 30 \AA (0.35); for $a_{||} = 5.51 \text{ \AA}$: 40 \AA . These different discs with same in-plane lattice parameter but different scattering strength implies variation in IQH sizes, which is expected in self-organized structures. The scattering strength can be related to the frequency or the number density of these discs in the system and also the scattering volume associated with them. It is to be noted that these profiles and our simple model could fit the data set measured at two energies.

The variation of the size of the iso-strain region corresponding to different $a_{||}$ as obtained from the fits of the angular scans are shown in Fig. 5.4(d). It is interesting to note that the iso-strain region is largest (around 440 \AA) near the base of the IQH structure below the Ge wet layer as is apparent in the TEM image shown in Fig. 5.1(d). The size of the iso-strain region decreases as $a_{||}$ increases, and from the angular scan in the vicinity of the zero-strain region with $a_{||}$ ($= a_{\perp} = 5.52 \text{ \AA}$), a value of around 80 \AA [refer to Fig. 5.4(d)] is obtained representing the

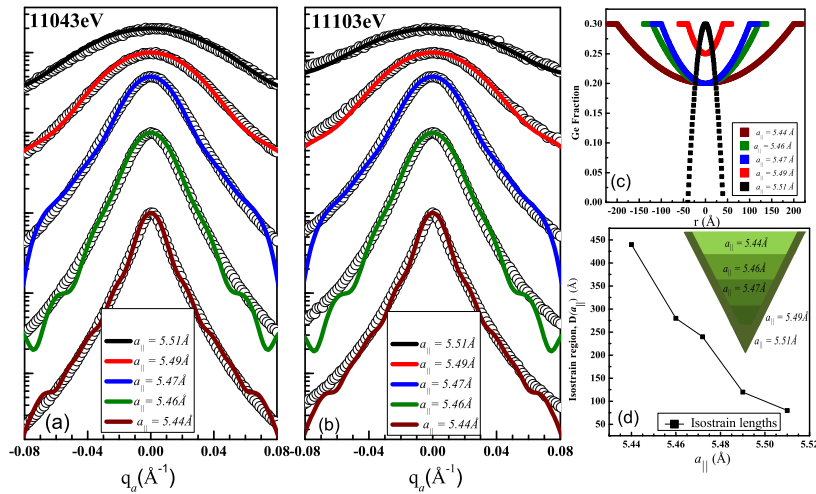


Figure 5.4: (a) and (b) Angular scans around (400) of the superlattice sample measured at 11 043eV and 11 103eV respectively. Each scan is associated with a different $a_{||}$ as indicated in the plot. The solid lines show fits assuming IQH composed of five disks having same in-plane lattice parameter. (c) the Ge fraction variation over the disk radially used for fitting. (d) Variation of the isostrain region with $a_{||}$ as obtained from the fits. Inset shows the schematic (not upto scale) of the IQH being divided into disks of isostrain region. The dark border represents the rim area having higher Ge concentration as observed in the XTEM images and also included in the calculation of fitted curves (refer text for further details).

tip area of IQH. This is consistent with the inverted pyramidal shaped quantum huts observed in XTEM data with higher Ge contrast at the tip of the IQH [refer to Fig. 5.1(d)].

5.4 Conclusion

In conclusion, it is shown that the IQH structure form in Si lattice through enigmatic large-scale diffusion of Ge through formation of $\text{Si}_{1-x}\text{Ge}_x$ alloys that minimize the variation of the out-of-plane lattice parameter. In this model the IQH structure is composed of a few stratified layers having a constant in-plane lattice parameter with varying composition to represent the rim of the IQH. As we approach the tip of the IQH from the base, in-plane lattice parameter approaches the out-of-plane lattice parameter to produce a zero-strain cubic lattice having $\text{Si}_{0.7}\text{Ge}_{0.3}$ composition.

Formation of IQH structures is indeed an interesting "growth model" problem and we believe with our experimental data some theoretical work will be done. Earlier theoretical models assume that at high growth temperature in-plane motion of deposited Ge is very high and there is very low diffusion of Ge across Si(001) surface [138]. At lower temperature in-plane diffusion is hindered. Out-of-plane diffusion and formation of inverted-hut of particular composition variation reported here is apparently lowering the free energy - theoretical/simulation work is required to understand the phenomena but this is not within the scope of this thesis work.

Chapter 6

Excitation-power independent

Photoluminescence in

Inverted-Quantum-Hut Structures

The electronic properties of nanoscale materials are variedly different from their bulk counterparts. In indirect-gap materials, the momentum wave-vectors of the conduction band minima and valence band maxima are different, which causes the electron-hole recombination in them to be mediated by either emission or absorption of phonons, in order to conserve momentum. Due to this indirect recombination, these materials show poor light emission properties. However, direct carrier recombination in such indirect-gap materials can be induced by utilizing the zone-folding effects which are predicted to occur in their superlattice structures [1,2]. Also, in their nanostructures such as quantum dots, a huge difference

in the electronic band-structure is observed i.e. the electronic states modify from being energy-bands to discrete energy states akin to atoms. Although for sufficiently large nanostructures, zone folding can be applied but it depends upon the extent of the fourier component of the envelop function of the charge carriers. Thus, such nanostructures play a very significant role in improving the optical emission properties of indirect-gap materials and hence, it is imperative to study their electronic band-structure in order to enhance their efficiency. Several spectroscopic techniques such as Raman spectroscopy, UV-Vis absorption spectroscopy and Photoluminescence have been employed to study the electronic band-structure of nanostructures. In any material system, photoexcitation can lead to the formation of electron-hole pair. The interaction between this pair can either be negligibly small or may have coulombic attraction depending upon the extent of their respective wavefunctions. Such interacting electron-hole pairs are known as excitons. Thus, the size of nanostructures governs the electronic properties such as exciton binding energy and the band-gap of the system. Photoluminescence is one of the principal techniques to investigate the excitons present in nanostructures which provide an understanding of the collective absorption and redistribution of excitation energy in them. This chapter deals with the photoluminescence study of inverted quantum huts with high Ge content formed below Ge-on-Si interfaces in the SiGe superlattice structure. Unlike conventional Ge quantum dots these structures exhibit excitation-power independent photoluminescence energy.

6.1 Introduction

Following huge abundance, the whole electronics industry is based on Silicon which shows inferior optical properties due to the indirect band-gap. However, self-assembled Si-Ge nanostructures in Si matrix offer a means to realize the Si-based optoelectronics. The pseudomorphic growth of Ge quantum dots on Si leads to the presence of an inherent strain in them. This inherent strain is responsible for the energy-band alignment and the confinement of carriers in these nanostructures and allows direct optical transitions in otherwise indirect band-gap semiconductors i.e. Si and Ge. Thus, Ge quantum dots in Si are of great importance as they ensure a route towards band-gap engineering in the already well-developed Si very large scale integration (VLSI) technology.

The self-assembled SiGe nanostructures (quantum dots) in Si matrix can be neatly grown by advanced deposition techniques such as molecular beam epitaxy (MBE) and chemical vapor deposition (CVD) where the excitons get spatially confined and lead to many interesting physical properties. These Ge quantum dots in Si are relatively simple structurally i.e. they contain only one kind of atoms, are structurally ordered due to the epitaxial growth in Si and can be controlled to produce uniform sizes by employing patterned Si substrates [109]. Epitaxial growth of Ge on Si takes place by Stranski-Krastonov growth mode i.e. during deposition the first few monolayers are in complete registry with the lower Si substrate and form a wet-layer. After three monolayer deposition, sufficient strain energy builds up in the wet-layer which leads to the formation of 3-D nanostructures i.e.

quantum dots (QD) to relax strain [17]. These quantum dots are then overgrown by Si capping in order to avoid oxidation and surface recombination of excitons. The Si in the vicinity of these relaxed Ge QD and the wetting layer suffers biaxial tensile strain. This tensile strain in Si lifts the degeneracy of the sixfold conduction band minimum and it is split into $\Delta(2)$ and $\Delta(4)$ bands. The strain gradient at the interface of Si and Ge creates a notch potential in the tensile Si where electrons are confined. Due to large offset in the valence band, the holes are confined inside the Ge QDs. Thus, the strain present in Si/Ge heterostructures defines the band-alignment at their interface. The spatial separation of electrons and holes in the system imply type II band-alignment in the highly strained Si-Ge nanostructures. The strain in the surrounding Si can be reduced by the alloying of Ge in the quantum dots which will reduce its lattice parameter to near to that of Si and hence the strain in vicinal Si will be lowered. This low strain in Si/SiGe system leads to a change in band-alignment from type II to type I. It has been reported previously that the $\text{Si}_{1-x}\text{Ge}_x/\text{Si}$ wetting layers having low x value show type I band alignment [110]. Annealing of Ge quantum dots at high temperature have also shown a transition of band-alignment from type II to type I [111]. Hence, band-gap in $\text{Si}_{1-x}\text{Ge}_x$ nanostructures depends upon their composition profile and strain present in them [17,112]. The optical efficiency of this system can be highly improved by producing uniform nanostructures. One possible route to attain uniformity is by preparing Si/Ge multilayers where Ge quantum dots form and stack one over the other in various layers due to strain propagation and obtain uniform

size [43, 115]. Recently, low temperature growth of Si/Ge multilayers has shown the formation of inverted quantum hut (IQH) structures below the Ge wet-layer with their apex pointing towards Si substrate [116, 117]. During the formation of such IQH structures, the deposited Ge atoms intermix with the lower Si layer in order to reduce strain and form stacks in the various multilayers. In this chapter, a type I band alignment occurring in the alloyed IQH structures and also in the wet-layer is studied. It is found that the confinement of carriers occurs mainly in the tip region of IQH which gives a strong PL signal. A uniform alloying in the wet-layer gives rise to no-phonon and its TO-replica corresponding to SiGe mode.

6.2 Experimental Details

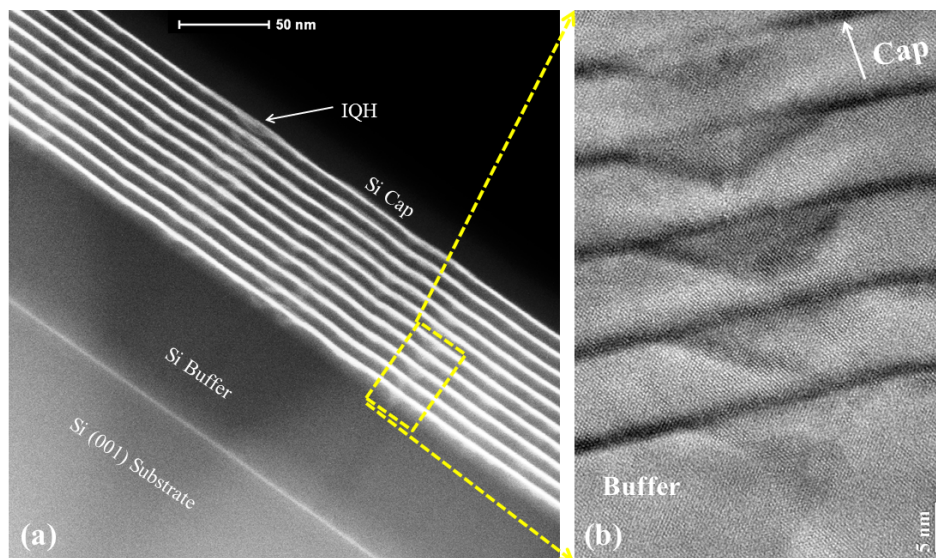


Figure 6.1: (a) HAADF image of IQH embedded superlattice structure. Stacking of IQH in various layers is evident. (b) High resolution XTEM image of self organized IQHs embedded in the superlattice structure.

PL study of IQH embedded Si/Ge superlattice under varying temperature and excitation power conditions has been presented. The 10 bilayer Si/Ge superlattice structure was deposited in a solid-source molecular beam epitaxy (MBE) system at a growth temperature of 400 °C. First a thick Si buffer layer of 100 nm was deposited on Si (001) substrate, then the 10 bilayer Si/Ge superlattice structure with nominal thicknesses of 70 /20 Å respectively were grown followed by a Si cap layer of 300 Å. Fig. 6.1(a) is a cross-sectional high angle annular dark field (HAADF) image showing the Si/Ge superlattice consisting of IQH structures. The dark region in the HAADF image signifies the presence of Si while the lighter ones represent the presence of Ge. Fig. 6.1(b) shows the high resolution cross-sectional transmission electron microscope (XTEM) image of IQH structures which are self-organized one over the other. It can be observed that the inverted quantum hut structures are formed with their base just below the wet-layer and apex pointing towards Si buffer layer. The vertical alignment of the IQH structures in the various layers of Si/Ge superlattice is also evident.

The process of the formation of IQH structures has already been studied and it was shown that the deposited Ge layer relaxes strain by uniform intermixing with the previously deposited lower Si layer to form a $\text{Si}_{0.6}\text{Ge}_{0.4}$ wet-layer and IQH structure form below it [refer Chapter 5]. X-ray scattering measurements were done which are sensitive to the average size of the IQH structures. These IQH structures are completely epitaxial and do not consist of any misfit dislocations as can be confirmed from Fig. 6.1(b). Hence, the IQH can be considered to be

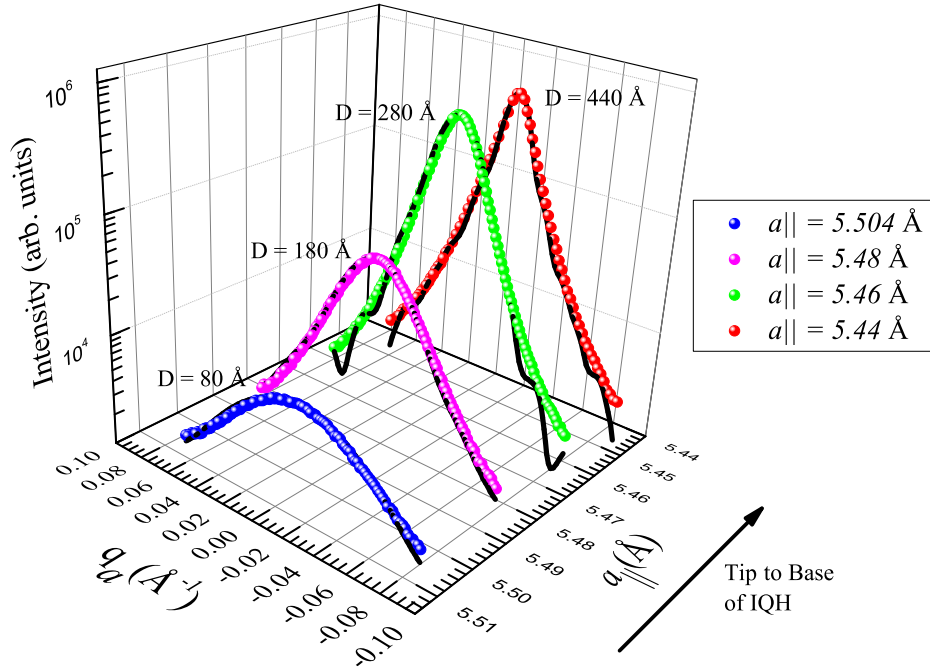


Figure 6.2: Angular scans around (400) of the IQH embedded superlattice structure measured at 11043 eV. Each scan is associated with a different $a_{||}$. The solid lines show fits assuming the IQH to be composed of five disks having same in-plane lattice parameter. The diameter of the disks for different $a_{||}$ is indicated.

made up of circular disks with disk-diameter increasing as one move from the base to the tip of the IQH. Each disk is assigned to a different in-plane lattice parameter ($a_{||}$) depending upon the composition and strain relaxation at that position within the IQH. Although, the XTEM measurements provide direct information about the size of the IQH present in system, but these details are localized as this study covers a very small portion of the sample. Hence, x-ray scattering was used to study the average size, composition and strain profile of the IQH structures. Since, the density of the IQHs present in the superlattice system is very low [refer Fig. 6.1(a)] and we intend to find the lateral size of these IQH, grazing incidence diffraction technique was used as surface sensitivity is highly improved in this

geometry. The x-ray experiments were performed at P08 beamline of Petra III, Germany. The x-ray energy used was 11043eV and the incident angle was fixed at 0.1° . Fig. 6.2 shows the angular scans in the vicinity of Si(400) diffraction peak. The z-axis is related to the measured intensity and the two in-plane axes (x & y) correspond to angular momentum transfer and the in-plane lattice parameter respectively. The various scans are sensitive to different $a_{||}$ and hence each scan corresponds to a particular disk in our model. The line profiles plotted with each angular scan data (represented by spheres) are the theoretical fits which provide the lateral extent (or diameter) of each disk. The details of the measurement and fitting procedure have already been discussed in detail [119]. As can be observed from the low magnification HAADF image [refer 6.1(a)], there is a variation in the size of various IQHs. Thus, during the fitting of these angular profiles, disks of different diameters were required, each having a different contribution (weightage) towards the fit [119]. The diameters of the various disks with their relative weightage (indicated in parenthesis) used to fit the angular scans corresponding to different $a_{||}$ are as follows: for $a_{||} = 5.44\text{\AA}$: 440\AA (1), 232\AA (0.35), 150\AA (0.16) and 86\AA (0.06); for $a_{||} = 5.46\text{\AA}$: 280\AA (1), 180\AA (0.55) and 120\AA (0.25); for $a_{||} = 5.483\text{\AA}$: 180\AA (1), 120\AA (0.75) and 64\AA (0.3); for $a_{||} = 5.504\text{\AA}$: 80\AA (1). The disk diameter having highest contribution is indicated with each profile [refer Fig. 6.2]. The $a_{||}$ near to Si lattice parameter ($a_{Si} = 5.43 \text{\AA}$) is located close to the wet layer and the higher $a_{||}$ corresponds to the region towards the IQH tip (as indicated in Fig. 6.2). From the fits, the diameter of the tip region was found to be

nearly 80 Å. Also, an interesting composition variation within IQH structure was observed from base to tip. The rim and tip region of the IQH structure were found to approach an alloy composition of $\text{Si}_{0.7}\text{Ge}_{0.3}$.

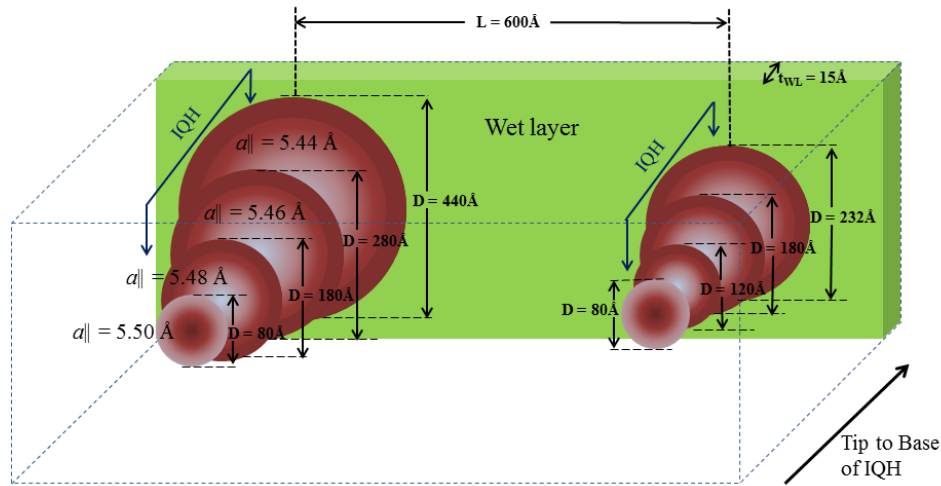


Figure 6.3: Schematic showing a typical bilayer consisting of IQH structures. The various dimensions (as indicated) represent the results as obtained from the analysis of x-ray data.

The primary results obtained from x-ray analysis are shown schematically in Fig. 6.3. As can be observed from the low magnification HAADF image [refer Fig. 6.1(a)], there is a variation in the size of various IQHs and we have indicated this with two sizes of IQH in Fig. 6.3. The wet layer thickness obtained from x-ray analysis was found to be around 15 Å. The IQHs are shown to be made up of circular disks each corresponding to a particular in-plane lattice parameter. Two nearest IQHs are represented, separated by 600 Å as obtained from the XTEM results. The average diameters of the various disks as obtained from the x-ray study are also indicated. The $\text{Si}_{1-x}\text{Ge}_x$ composition gradient in each of these

disks is shown by the color gradation. The dark color at the rim and tip regions correspond to the presence of higher Ge content ($\text{Si}_{0.7}\text{Ge}_{0.3}$) as compared to the central lighter region having a rather lower Ge content ($\text{Si}_{0.8}\text{Ge}_{0.2}$). It was shown that the intriguing composition variation within IQH lead to a very low strain value of 1.66% between the rim structure and the vicinal Si [119].

Temperature and excitation power dependent PL measurements were performed in a closed-cycle helium cryostat whose temperature ranges from 10 to 300 K, with a 980 nm semiconductor laser. The PL spectra were recorded by a liquid nitrogen cooled InGaAs detector using standard lock-in technique.

6.3 Results and Discussion

Fig. 6.4(a) shows the temperature dependent PL spectra taken at an excitation power of 40 mW. The PL signal is observed to be very broad even at low temperatures. The PL spectra from 10 to 50 K has been fit using three Gaussian as are shown by the dash-dot lines for the 10 K spectrum in Fig. 6.4(a). Thus, a combined contribution from three different PL peaks having their centers positioned around 0.81, 0.87 and 0.92 eV leads to a broad PL intensity. The PL emission peak at 0.81 eV can be attributed to the confinement of charge-carriers in the IQH structure while the peaks at 0.92 and 0.87 eV are the no-phonon (NP_{WL}) and its transverse-optic (TO_{WL}) replica respectively which occur due to the confinement in the wet-layer [118]. This peak position for wet-layer corresponds to a thickness of around 4.5ML [118] which matches with the thickness of nearly 15 Å [119] of

the present sample. These peaks are ~ 49 meV apart and hence correspond to Si-Ge optical phonon energy peak [121]. The temperature dependence of the three peaks is shown in Fig. 6.4(b). The peak positions of wet-layer related PL remain invariant with the rise in temperature from 10 K to 50 K and this emission quenches for higher temperatures.

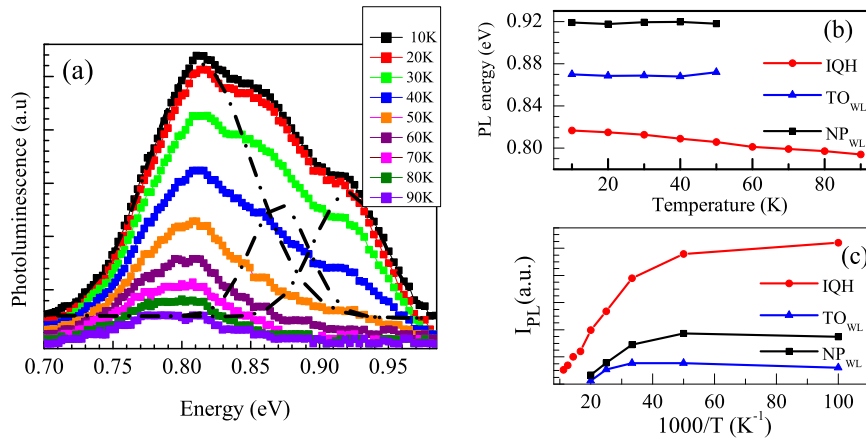


Figure 6.4: (a) Temperature dependence of the IQH embedded superlattice PL spectra. The PL spectra at low temperature can be fit using three gaussians as indicated by three dash-dot curves for 10 K spectrum. (b) and (c) Temperature dependence of PL peak positions and IPL respectively of the three peaks corresponding to IQH, TO_{WL} and NP_{WL} . At higher temperatures (60 K and above) only IQH related PL is observed.

Fig. 6.4(c) shows the variation of integrated PL intensities (I_{PL}) with the change in temperature for the three peaks. The integrated PL intensities (I_{PL}) for all the three peaks are seen to decrease with rise in temperature. This shows that bound-excitons attain thermal energy to escape the bound-state and recombine non-radiatively as the temperature increases.

Excitation power dependent measurements were done at 10 K and are shown in Fig. 6.5(a). A shift in the emission peak or absence of it depends upon the type

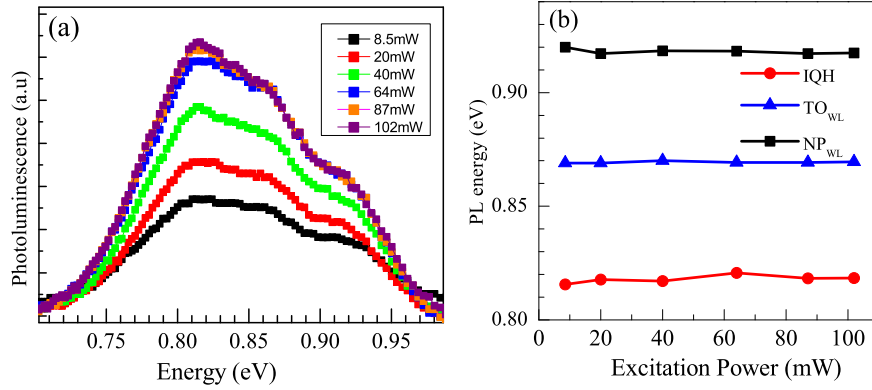


Figure 6.5: (a) The excitation power dependent PL spectra at 10 K. (b) and (c) show the power dependence of the PL peak energies and the I_{PL} respectively for the three Gaussians at 10 K.

of band lineup present in the system. For type II band-alignment or the spatially indirect transitions, carriers are trapped in the notch potential of Si/Ge interface with holes inside the Ge and electrons inside the Si region. These spatially separated charge carriers build up an electrostatic potential which bends the energy-bands [124]. As the carrier concentration increases with the increased excitation power, the Si conduction band bending shifts the electrons to higher energies due to increased confinement in the notch potential and hence leads to a blueshift in the PL emission energy.

With the variation in pump power, the peak positions of all the transitions are observed to remain unaltered as can be seen in Fig. 6.5(b). This infers that the transitions related to these PL peaks corresponding to the IQH and the wet-layer are type I and no band-bending is induced with the increase in excitation power. Previous studies [125] have shown that at high excess carriers concentration, an increase in Ge content leads the carriers to recombine via fast recombination chan-

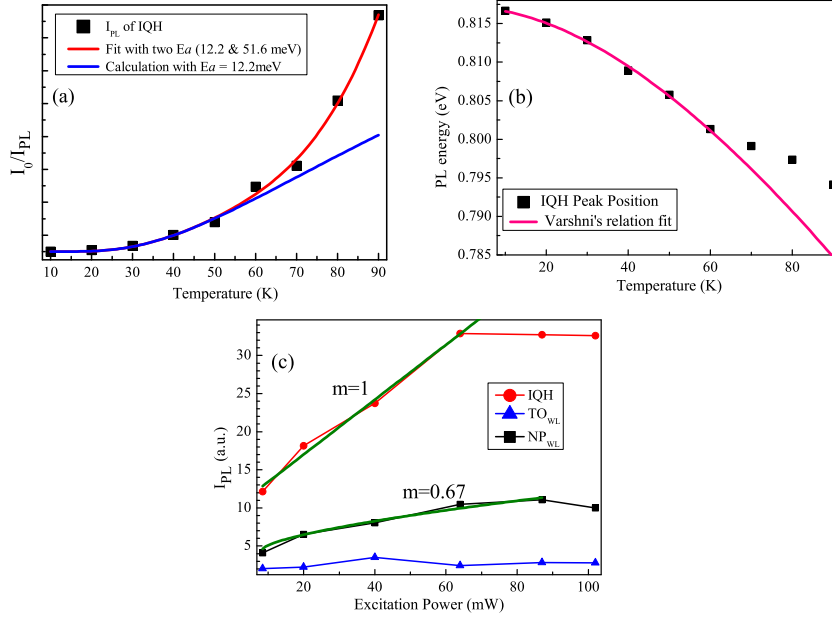


Figure 6.6: (a) I_0/I_{PL} versus temperature plot for IQH related emission. The line profile represents the fit considering two activation energies (12.2 and 51.6 meV). Also, calculation of the intensity variation is shown for activation energy of 12.2 meV. (b) Temperature variation of PL peak position and fit by Varshni's relation for IQH related emission. (c) Variation of integrated PL intensity for the three peaks with excitation power. The line profiles represent the power law ($I \propto P^m$) fit for the IQH and NP_{WL} peaks. The corresponding power exponents are indicated.

nels which signify the presence of Type-I energy band-alignment.

Fig. 6.6(a) shows the variation of IQH related integrated PL intensity. The thermal activation energy for the IQH related and wet-layer related peaks can be calculated by following equation [122]:

$$I_0/I_{PL}(T) = 1 + C_1 e^{-E_1/kT} + C_2 e^{-E_2/kT} \quad (6.1)$$

where I_0 is the maximum intensity, E_1 and E_2 are the thermal activation energies,

C_1 and C_2 are fitting parameters and k is Boltzmann's constant. Fig. 6.6(a) shows the curve fitting for variation of I_0/I_{PL} related to IQH emission with temperature using Equation 6.1 and the activation energies are found to be 10 and 49 meV. These activation energies can be related to the confinement of carriers in the base and tip regions respectively of the IQH. It is interesting to note that the activation energy of 49 meV corresponds to a carrier confinement dimension of 70 Å [123] which is nearly the size of the tip of IQH structures as obtained from the XTEM and x-ray studies. Thus, the PL peak around 0.81 eV originates mainly from the confinement of excitons in the tip region. As the temperature increases, the bound excitons dissociate into free or non-correlated pairs of electron and holes which leads to a decrease in the PL intensity. From XTEM and x-ray studies, it is known that the density of IQH in the superlattice system is very low and only 15% of total Ge resides in them while rest of the Ge belongs to the wet layer. Despite the very low Ge content, the IQH show very high PL emission which is due to the confinement of excitons in these structures.

The PL peak originated from IQH shifts the energy position from 0.81 to 0.79 eV as the temperature is raised from 10 to 90 K. The temperature dependence of this band-gap related emission can be approximated by Varshni's equation [120] given by $E(T) = E_g - \alpha T^2 / (T + \beta)$ as shown in Fig. 6.6(b), where $\alpha = 0.0012$ eV/K and $\beta = 210$ K. E_g is band-gap approximation at 0 K and is found to be 0.82 eV. It should be noted that the IQH peak follows Varshni's relation only in the low temperature region and at high temperatures, the IQH indicate higher band-gap

than expected by Varshni's relation. It is to be noted here that atom-like levels expected in quantum structures are not expected to show variation of 'band-gap' with temperature.

Fig. 6.6(c) shows the variation of integrated PL intensity (I_{PL}) with the excitation power for the three emissions. According to the formula $I \propto P^m$, where 'I' represents the PL intensity and 'P' the excitation power, the exponent 'm' is found to be 1 and 0.67 respectively for the IQH related and NP_{WL} peaks. The sub-linear powers and saturation of I_{PL} are generally attributed to the Type-II band alignment (which is confirmed by the PL peak blue-shift with energy). However, the PL peak energy positions do not shift with the excitation power [refer Fig. 6.5(b)] for both IQH and NP_{WL} peaks. We need to carry out further studies to show that the band-gap alignment is Type-I for the IQH structure presented here. The saturation of the peak intensities can be attributed to the filling of finite density of states in the IQH and wet layer as the excitation energy used here was not high enough.

6.4 Conclusion

Results of a photoluminescence study of MBE grown SiGe superlattice structures having inverted quantum huts with high Ge content formed below Ge-on-Si interfaces have been presented. Unlike conventional Ge quantum dots formed above Ge-on-Si interfaces, the presented quantum structures exhibit excitation-power independent photoluminescence energy. The presented results may be very influ-

ential to develop silicon based optical materials.

Chapter 7

Extraction of structure and composition of InAs quantum dots grown on GaAs substrate as a function of in-plane dot separation

So far, this thesis work is primarily concerned with SiGe nanostructures, in this last chapter, we have shown that the techniques developed by us in this thesis can also be applied to other semiconductor nanostructures i.e. InAs quantum dots on GaAs which also follow Stranski-Krastonov growth mode. InGaAs quantum dots are very important for technological applications [126] and we show here that the developed methods in this thesis can be used in these III-V systems to tune structure-spectroscopy relationship. Self-assembled InAs/GaAs quantum

dots are finding novel applications [127] in several optoelectronic technologies such as lasers, quantum dot infrared photodetector (QDIP) and single-photon sources [128]. Several studies have been done on such quantum dots to obtain the bound-state energy levels of electrons confined in them [129]. It has been pointed out recently that the In-Ga intermixing within the self-assembled quantum dots strongly influences intensity and polarization of emitted photons [130] as the confinement length of the carriers within quantum dots depend mainly upon the In composition profile within a quantum dot (QD) and not just on the size [131]. By systematic measurements using grazing incidence diffraction (GID) techniques and atomic force microscopy (AFM) techniques, correlation in composition and morphology including in-plane structure across the length of an average QD can be determined. This in turn will enable us to understand and tune the energy-spread of the emitted PL from the individual quantum dots deposited on a substrate.

7.1 Introduction

Strained layer heteroepitaxy through Stranski-Krastonov (S-K) growth mode for InAs/GaAs system provides a direct route to produce self-assembled quantum dots. In this growth mode, first a 2D wet-layer of InAs is formed upto 1.7 monolayer (ML) deposition which is followed by the formation of coherent QD on the surface [132]. This classical S-K growth mode is followed only at lower growth temperatures (around 350°C) i.e. after wet-layer formation, additional

InAs forms QD. However, at higher growth temperatures of 420°C and more, it is observed that the volume of QD so formed is much higher than the deposited additional InAs which provides a direct evidence of considerable migration and intermixing [133,134] of In and Ga. Substantial intermixing of In and Ga was also observed in thickening of wet layer after formation [135]. High resolution transmission electron microscopy measurements [136] and scanning tunneling electron microscopy studies [137, 138] have indicated segregation of In towards the center and tip of the QD above the wet-layer. It is essential now to understand role of various growth conditions, like the deposition rate and temperature, to tune the size and composition of these QD for obtaining desired electronic structure and optical properties [129, 139].

Systematic GID measurements of InAs QD deposited on GaAs substrate were carried out as a function of in-plane dot separation that happens due to local substrate temperature variation. The presented results indeed show that the In-composition profile extracted from GID data within InAs QD depends on the local growth temperature. The statistically averaged information obtained from GID study was found to be consistent with the local information obtained from the AFM measurement. The information of the In-Ga intermixing obtained from this study was found to be important to understand the energy-spread and the position of the PL peak obtained from these quantum dots.

7.2 Experimental Details

The InAs quantum dots studied here were grown on 4 inch-diameter GaAs substrate using Molecular Beam Epitaxy technique. Depending upon the specifics of the Indium effusion cell in the MBE chamber, there is a radial variation in the deposition of InAs on the substrate surface, which leads to highest deposition at the center of the substrate and approximately 10% less deposition at the edges of the wafer. The sample holder arrangement used here leads to a variation in the temperature from the center to the edge region; as the retaining clips cause heat sinking that lower the temperature at the edge. The substrate is rotated azimuthally during deposition to provide circular symmetry on the surface and this arrangement helped us to create the variation in separation between the dots due to variation of local growth temperature from center to the edge of the substrate. A thin InAs layer of 0.86 nm thickness was deposited on GaAs at a growth temperature of 515°C. It was then covered by a 10 nm GaAs layer cold-cap at the same temperature followed by a growth interrupt during which the temperature was raised to 580°C. At 580°C, a 200 nm thick buffer of GaAs is deposited followed by lowering of growth temperature to 515°C and deposition of InAs QD layer having same thickness as earlier. It should be noted here that GID and AFM data presented here are from the top QD layer of InAs and PL data comes from the buried InAs QD layer. We plan to carry out GID and PL measurements from same InAs QD layer by reducing the thickness of GaAs buffer layer from 200 nm to about 20 nm. For the present study, we concentrate more on structural as-

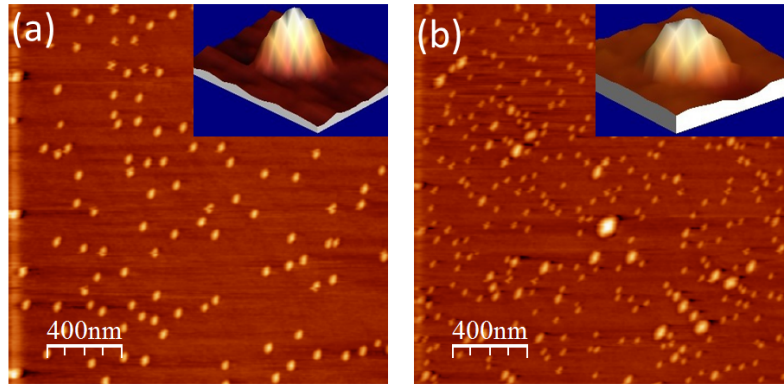


Figure 7.1: (a) and (b) AFM images of InAs quantum dots formed on the top surface of the substrate at centre and edge respectively. Insets show the 3-D view of a single QD in the respective low and high density regions.

pect and present only representative PL data with the assumption that buried QD layer is conformal to the top QD layer. AFM, GID and PL studies have been performed on this sample at different positions corresponding to different in-plane QD densities. By AFM measurements, we obtain a direct estimate of the QD size distribution along with their density. The GID measurements provide significant insight into the In-composition profile in an average QD and also provide valuable information regarding the strain profile as a function of height within an average QD. PL measurement results presented here provided us information regarding optical properties of the buried QD layer as a function of in-plane QD density.

AFM measurements of the InAs QD present on the top surface of the sample at the center and edge positions exhibiting different in-plane QD densities are shown in Figs. 7.1 (a) and (b) respectively. The QDs at both the positions on the sample

surface are seen to be elongated in shape. QDs towards the edge of the substrate surface are observed to have diameters roughly 31 and 50 nm in the two mutually perpendicular directions and height 17 ± 4 nm. Also, presence of very few dome sized islands could be seen. As one moves toward the center of the substrate having higher growth temperature, QDs with diameters of around 38 ± 2 nm and 60 ± 3 nm in the two mutually perpendicular directions and height of 25 ± 2 nm are observed. The QDs in this region are seen to be of uniform size and the dome sized islands are completely absent here. This can be understood by the fact that at higher temperature, the adatoms have higher kinetic energy on the sample surface which leads to the self-sizing of the QDs [140]. The higher volume of the QDs at the center may be attributed to the higher InAs deposition [141] at the central region of the substrate surface. This higher mobility of the adatoms on the central region of substrate surface leads to a lowering of the QD in-plane density from 100 per μm^2 at the edge to 50 per μm^2 at the center. Thus, the central portion of the substrate surface will now be referred as low QD density region and edge portion as high QD density region in the rest of the paper. Insets of Fig. 7.1(a) and 7.1(b) show the 3-D view of a representative single QD in the low and high QD density regions, respectively. Fig. 7.2(a) and 7.2(b) show the size distribution of QD in the low and high density regions respectively.

GID measurements [refer Fig. 3.7 for the geometry] were performed at the two different QD density regions on the sample surface to study their size, strain profile and the amount of In-Ga intermixing as a function of height. GID ex-

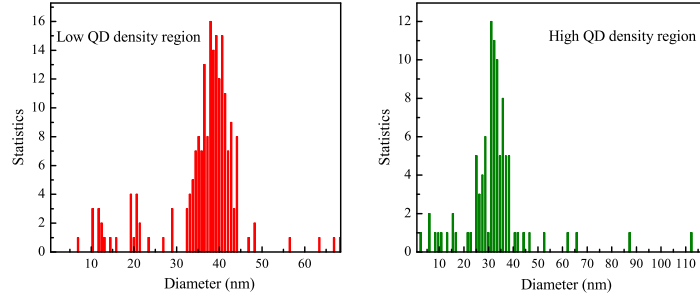


Figure 7.2: (a) and (b) Size distribution of the QD in the respective low and high QD density regions as obtained from the AFM analysis software WSxM.

periments were performed at Beamline P08 of Petra III synchrotron in DESY, Germany at energy of 11.103 keV. A beam-defining slit setting of dimension 50 by 300 micron was used in vertical and horizontal directions, respectively and the data was collected by a position sensitive linear Mythen detector. For grazing incidence diffraction (GID) measurements, the intensity of all the channels was integrated to obtain the data presented here. During GID measurements the incident angle was kept to be 0.1° which is lower than the critical angle for GaAs, to keep the x-ray beam onto the surface of the sample and hence to study the InAs QD present at the top surface. Radial and angular scans were taken around two in-plane diffraction peaks i.e. around (400) and (200).

7.3 Results and Discussion

We have carried out radial and angular scans in the GID geometry. Radial scans are simple intensity measurements in which incidence angle to the planes in the sample surface (θ) and detector angle (ϕ) are varied following $\phi = 2\theta$. The inten-

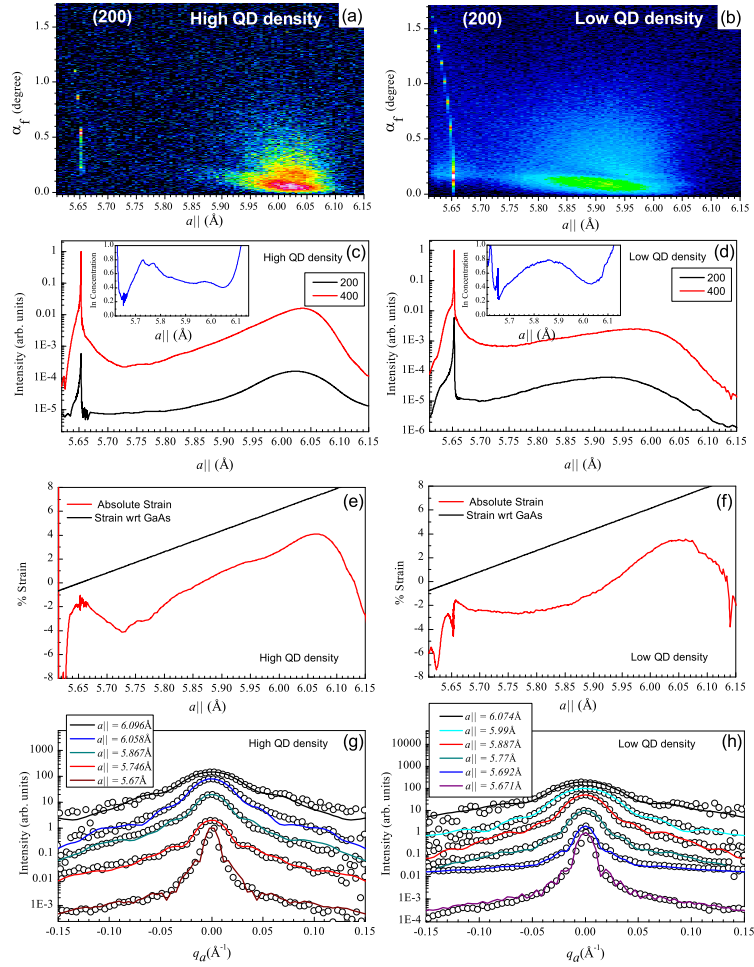


Figure 7.3: (a) and (b) Two-dimensional GID data around (200) for the high and low QD density regions respectively. Y-axis represents the exit angle in the Mythen detector. (c) and (d) Line profile of the radial scans around (200) and (400) as indicated for the high and low QD density regions respectively. These line profiles are generated by the integration of all the pixels of mythen detector. Respective insets show the variation of In concentration with $a_{||}$. (e) and (f) Profiles of the absolute strain present in the QD and strain with respect to GaAs (refer text for the method of calculation) as a function of $a_{||}$ for the high and low QD density regions respectively. (g) and (h) Angular scans around (400) corresponding to different in-plane lattice parameters as indicated for the high and low QD regions respectively.

sity measurement by this type of scan can be directly related to the in-plane lattice parameter ($a_{||}$) defined as $a_{||} = \lambda\sqrt{h^2 + k^2 + l^2}/(2\sin(\phi/2))$, where (h,k,l) are the Miller indices of the nearest Bragg reflection. In angular scans θ is varied by keeping ϕ value constant and these data give the size of the region in the sample having a fixed lattice parameter corresponding to the ϕ position ($q_r = (4\pi/\lambda)\sin(\theta - \phi/2)$). Only the angular momentum transfer ($q_a = (4\pi/\lambda)\sin(\theta - \phi/2)$) changes in such a scan and the radial momentum stays constant.

Fig. 7.3(a) and (b) show the 2-D plot of the radial scans around (200) at high and low QD density regions respectively. These plots show the scattered intensity variation with respect to the in-plane lattice parameter (along X-axis) and the exit angle in the Mythen detector (along Y-axis). In the high QD density region, the scattered intensity is concentrated over a small lattice parameter variation ($a_{||} = 5.95$ to 6.08 Å) while for low QD density region, it is observed to be diffusely scattered over large in-plane lattice parameters ($a_{||} = 5.77$ to 6.02 Å). Fig. 7.3(c) and (d) represent the radial scans around (400) and (200) diffraction peaks (as indicated) performed at the high and low QD density regions respectively. These line profiles are generated by integrating the intensity along the length of the mythen detector. Since, GaAs has zinc-blende type structure, the structure factors for (400) and (200) can be written as $F_{400} = f_{Ga} + f_{As}$ and $F_{200} = f_{Ga} - f_{As}$. The QD presented in this study are mainly composed of InAs and are deposited upon GaAs substrate at high growth temperatures which lead to In-Ga intermixing and hence the structure factors for the two reflections can be

written as $F_{400} = xf_{In} + (1 - x)f_{Ga} + f_{As}$ and $F_{200} = xf_{In} + (1 - x)f_{Ga} - f_{As}$ where x is the concentration of In present in the quantum dots. Thus, by comparing the intensity ratio around the two diffraction peaks, one can find out the In content (x) inside the $In_xGa_{1-x}As$ quantum dots as follows:

$$\frac{I_{400}}{I_{200}} = \left(\frac{xf_{In} + (1 - x)f_{Ga} + f_{As}}{xf_{In} + (1 - x)f_{Ga} - f_{As}} \right)^2 \quad (7.1)$$

which gives the In concentration ‘ x ’ as follows:

$$x = \frac{\sqrt{I_{400}/I_{200}}(f_{Ga} - f_{As}) - (f_{Ga} + f_{As})}{(f_{In} - f_{Ga})(1 - \sqrt{I_{400}/I_{200}})} \quad (7.2)$$

where I_{400} and I_{200} are the measured intensities around (400) and (200) diffraction peaks respectively, f_{In} , f_{Ga} and f_{As} are the scattering factors of Indium, Gallium and Arsenic at 11.103kV respectively. Insets in Fig. 7.3(c) and (d) show the variation of In content with respect to the in-plane lattice parameter for high and low QD density regions respectively as calculated using the method described above. The In concentration increases upto ($x =$) 0.8 with increasing in-plane lattice parameter and then reduces to ($x =$) 0.4 towards the InAs lattice parameter for both the low and high QD density regions, however there is difference in exact composition profile for the QDs in the two regions. The absolute in-plane strain present in the QD can be calculated by comparing the in-plane lattice parameter ($a_{||}$) with the lattice parameter corresponding to the In content [$a(x)$] given as $\varepsilon_{||} = [a_{||} - a(x)]/a(x)$. Also, one can calculate in-plane strain with respect to the

GaAs lattice parameter given by $\varepsilon_{||} = (a_{||} - a_{GaAs})/a_{GaAs}$. These calculated strain values are represented in Fig. 7.3(e) and (f) for high and low QD density regions respectively. The absolute strain in the QD system varies from highly compressive to tensile as the in-plane lattice parameter increases for both the QD density regions. It can be observed from the Fig. 7.3(e) that the strain value varies from -4 (compressive strain) to +4 (tensile strain) with a high slope for the high QD density region while for low QD density region it varied from -2 to +3 with the increase in lattice parameter (refer Fig. 7.3(f)). Thus, the QDs in low QD density region are more relaxed than those in the high QD density region. This is due to higher In-Ga intermixing in the low QD density region. Also, the calculated strain with respect to GaAs is shown in Fig. 7.3(e) and (f) for comparison.

Since the quantum dots under investigation are epitaxial, so towards the base of the islands, the in-plane lattice parameter would be near to that of GaAs (5.653Å) and as one move up towards the apex, the lattice would tend to be more relaxed and in-plane lattice parameter will be nearing to that of InAs (6.058Å). Thus, the lattice near the base of QD will suffer compressive strain and that near the apex of QD will experience tensile strain as due to interdiffusion, In content is lower in the apex of QD and higher in the middle region. The In concentration increases with increasing in-plane lattice parameter upto ($x \approx$) 0.8 and then reduces to ($x \approx$) 0.4 towards the InAs lattice parameter. Hence, the layers just above the GaAs substrate suffer huge compressive strain which than relaxes to a lower value in the layer above and as more and more In-Ga intermixing occurs towards a_{InAs}

which is at the apex of QDs, the strain in the QDs becomes tensile. For simplicity, we can define the QD as consisting of several disks arranged one over the other, each having a unique lattice parameter. Fig. 7.3(g) and (h) show typical angular scans at the high and low QD densities respectively around (400) diffraction peak at several fixed radial momentum positions which correspond to different in-plane lattice parameters as indicated. These angular momentum intensity plots provide us the isostrain length scales i.e. the length of the area having same in-plane lattice parameter which can be considered to be the radius of the disks in the model so considered. The contribution of each disk with radius ‘R’ in the x-ray scattering profile so obtained can be given by [142]:

$$I(q_a, R) = \frac{I_0}{\pi^2 R^4 | \langle f_{InGaAs} \rangle |^2} \left| \int_0^{2\pi} \int_0^R e^{-iq_a r \cos(\theta)} f_{InGaAs}(r) r dr d\theta \right|^2 \quad (7.3)$$

where $f_{InGaAs}(r)$ is the effective scattering factor at position ‘r’ in the disk. The line profiles in Fig. 7.3(g) and (h) show the fit of the angular momentum intensity profiles as calculated using Equation (2). Two disks having different radii with dissimilar contribution to the fit had to be considered for the calculation of profiles. Tables 7.1 and 7.2 show the several radii used to fit the angular scan intensities indicated by $a_{||}$. The ratios of the intensities corresponding to different radii used to fit the data are represented in the column ‘Respective contributions’. It should be noted that the effective scattering factor, f_{InGaAs} , was taken to be constant over the whole disk as the consideration of varied composition over the

Table 7.1: High QD density

$a_{ }(\text{\AA})$	Radii (\AA)	Respective contributions
6.096	75, 28	1, 0.3
6.058	105, 50	1, 0.24
5.867	130, 50	1, 0.2
5.746	135, 45	1, 0.11
5.67	300, 90	1, 0.06

Table 7.2: Low QD density

$a_{ }(\text{\AA})$	Radii (\AA)	Respective contributions
6.074	65, 20	1, 0.15
5.99	75, 40	1, 0.15
5.887	115, 65	1, 0.21
5.77	145, 65	1, 0.15
5.692	220, 70	1, 0.085
5.67	250, 75	1, 0.01

disk barely modified the profile. The two radii given here may be attributed to the variation in QD diameter. The scattering strength or the number density of these different diameters is represented by the values presented in the parenthesis. Hence, the contribution of the smaller diameter QD towards scattering is very low as compared to the larger diameter QDs. Thus, only QDs with larger diameter are considered for further data interpretation.

Fig. 7.4 shows the variation of the isostrain region with $a_{||}$ for the two QD density regions. It can be observed that as the in-plane lattice parameter ($a_{||}$) increases, the radii of the disks constituting the QDs decrease. This coincides with the fact that the lower $a_{||}$ values represent the base region of the QD and higher $a_{||}$ values amount to their apex. The diameter of 50nm for the base of QD in low density region matches perfectly with the average value as obtained from AFM

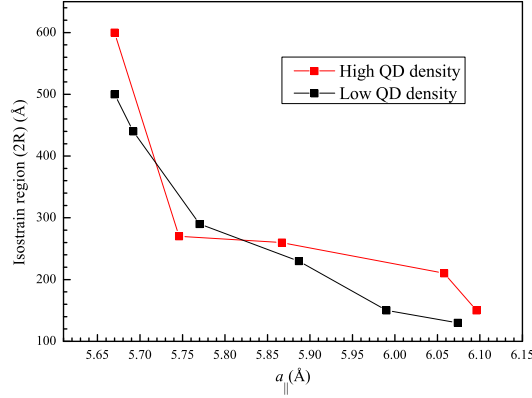


Figure 7.4: Isostrain region (2R) variation with $a_{||}$ for the two QD density regions. The larger ‘R’ value are chosen from Tables 7.1 and 7.2 for the plot as their contribution is higher.

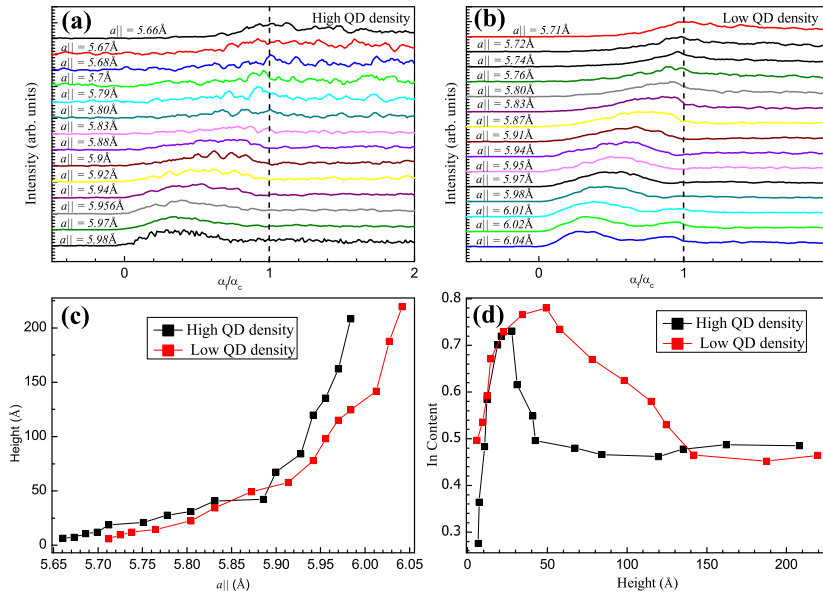


Figure 7.5: (a) and (b) Experimental exit angle (α_f) spectra corresponding to different $a_{||}$ for high and low QD density regions respectively. (c) Height with respect to the GaAs substrate (refer text for calculation) for different $a_{||}$. (d) The variation of In content with height inside the QD for the two QD densities.

measurements. However, the value of 60nm for the base diameter in the high QD density region is higher than that estimated from the AFM measurements. It should be noted here that in the high QD density region, the islands have varied sizes and occurrence of large sized domes is also evidenced. This can lead to the discrepancy in the results of the two techniques as x-ray provides statistically averaged results over large areas and AFM measurements yield essentially localized information of the surface. Also, it is to be noted that the two disc sizes arisen from this data analysis suggest presence of differently sized QDs in the system. However, terming it to be a bimodal distribution might not be correct as the contribution of lower size discs is very small.

The position of a disk, with given $a_{||}$, above the GaAs surface can be estimated from the exit angle plots of the Mythen detector. Fig. 7.5 (a) and (b) show the exit angle plots [in (400) diffraction geometry] at zero angular positions corresponding to different in-plane lattice parameters (as indicated) for the high and low QD density regions respectively. These exit angle intensity profiles can be plotted directly from the radial scans as their 2-D plots [refer Fig. 7.3(a) and (b)] show intensity variation with respect to α_f and $a_{||}$. From the position of the first maximum (α_f^{max}), the height z corresponding to any $a_{||}$ can be calculated as follows [143]:

$$z = \frac{1}{k\alpha_f^{max}} \arccos(\alpha_f^{max}/\alpha_c) \quad (7.4)$$

where k is the wave number of the x-ray beam and α_c is the critical angle for GaAs. Thus, the height of a particular isostrain region in the QD from the GaAs

surface can be calculated easily and is represented in Fig. 7.5(c). It is observed that as the in-plane lattice parameter increases, the height inside the quantum dot also increases monotonically. Thus, from base to apex of the QD, the in-plane lattice parameter increases and the diameter of the quantum dot decreases. The base radii so obtained for both the low and high density regions are comparable to the dimensions obtained from the AFM measurements. The radii corresponding to the highest in-plane lattice parameter in both the regions correspond to the apex region of the quantum dots. Also, it is observed that the apex of the quantum dots corresponding to the a_{InAs} ($= 6.05 \text{ \AA}$) is under high tensile strain for both the QD regions [refer Fig. 7.3(e) and 7.3(f)].

By comparing the in-plane lattice parameter with those in the insets of Fig. 7.3(c) and (d) respectively for the high and low QD density regions, we can find out the average In content in each of these disks represented by different angular scans. Fig. 7.5(d) shows the variation of In content within the QD as a function of height. It is observed that the In content increases from the base to the center of the QD and then again decreases towards the apex for lower in-plane density QD. This observation is consistent with the previous XTEM studies and theoretical calculations performed on InGaAs QD which show a segregation of Indium in their central region [136]. For the higher in-plane density QD, the In content increases rapidly from base and then fall rapidly within 5nm to attain a nearly constant value until the apex of QD. It is also apparent from the fact that the lower portion of QD suffer compressive strain which has higher In content and it decreases towards the

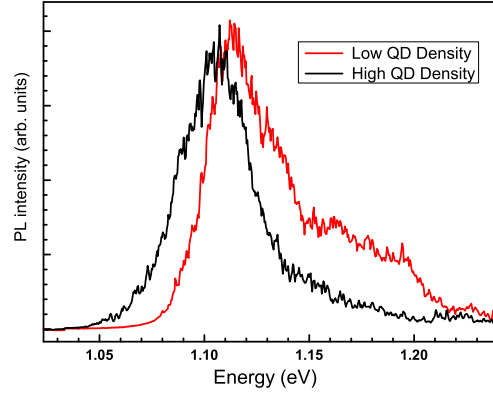


Figure 7.6: Photoluminescence spectra at the low and high QD density regions.

apex of QD and the lattice suffers tensile strain. The highest Indium content of ($x =$) 0.74 obtained near the base of the QD in high density region exhibit iso-strain radius of 13nm at a height of 3nm above the GaAs surface while that of ($x =$) 0.78 for the QD in low density region provide iso-strain radius of 11.5nm at a height of 8nm above GaAs surface. This highest In content can be attributed to the base of the QD with rest of the QD having almost constant In content up to the apex in the high QD density region, while for the low QD density region, the highest In content is present inside the QD which again decreases to attain a lower value ($x =$ 0.4) towards the tip. The observed diffuse intensity over large q -space in the measured two-dimensional GID data shown in Fig. 7.3(b) clearly indicate larger variation of In-composition within dots present in the region of low in-plane density. It is expected that lower variation of In-composition, apparent in Fig. 7.3(a) and 7.5(d), in dots present in the high density region will provide sharper PL.

Fig. 7.6 shows the PL spectra at the two QD density regions. A picoquant 785nm laser diode driven at 80MHz was used as the excitation source for collecting PL spectra at room temperature. The PL peaks are observed to be at 1.114 eV (FWHM = 0.042 eV) and 1.106 eV (FWHM = 0.040 eV) for the low and high QD density regions respectively. The peak position is observed to be shifted to lower energy giving sharper peak for the high QD density region as compared to that for low QD density region. This can be attributed to the higher In-Ga interdiffusion in the low QD density region [145, 146]. Also, the higher InAs deposition on the central portion of the substrate surface may lead to the introduction of crystal defects such as dislocations which lead to the shifting of PL peak energy to higher values [147].

7.4 Conclusion

InAs QD on GaAs surface grown at different deposition temperatures on a single wafer have been studied. AFM measurements suggest the coarsening of small QD to form uniformly sized larger QD for the higher deposition temperature. This coarsening leads to variation in In-Ga intermixing inside the QD deposited at different growth temperatures. Relatively low variation of In concentration within QD structures present in high in-plane density region exhibit sharper PL emission. Further studies are required using the techniques developed here to obtain GID and PL data from same layer of QD to develop better understanding in structure-spectroscopy relationship in these technologically important materials.

Bibliography

Bibliography

- [1] T. P. Pearsall, J. Bevk, L. C. Feldman, J. M. Bonar, J. P. Mannaerts and A. Ourmazds, *Phys. Rev. Lett.* 58, 729 (1987).
- [2] M. Kumagai, T. Takagahara and E. Hanamura, *Phys. Rev. B*, 37, 898 (1988).
- [3] G. Abstreiter, H. Brugger, T. Wolf and H-J. Jorke *Phys. Rev. Lett.* 54, 2441 (1985).
- [4] K. Ismail, F. K. Le Goues, K. L. Saenger , M. Arafa , J. O. Chu , P. M. Mooney and B. S. Meyerson *Phys. Rev. Lett.* 73, 3447 (1994b).
- [5] B. F. Levine, *J. Appl. Phys.* 74, R181 (1993).
- [6] J. Faist, F. Capasso, D. L. Sivco, C. Sirtori, A. L. Hutchinson, and A. Y. Cho, *Science*, 264, 553 (1994).
- [7] S. Fafard, K. Hinzer, S. Raymond, M. Dion, J. McCaffrey, Y. Feng, S. Charbonneau, *Science*, 274, 1350 (1996).
- [8] Z. Yuan, B.E. Kardynal, R.M. Stevenson, A.J. Shields, C.J. Lobo, K. Cooper, N.S. Beattie, D.A. Ritchie, M. Pepper, *Science*, 295, 102 (2002).
- [9] A. Morello, *Nature Nanotech.* 8, 233 (2013).
- [10] N. Hrauda, J. Zhang, E. Wintersberger, T. Etzelstorfer, B. Mandl, J. Stangl, *Nanolett.* 11, 2875 (2011).
- [11] *Semiconductors and Semimetals: Robert Hull, John C. Bean*, 56 (1999).
- [12] D. J. Eaglesham and M. Cerullo, *Phys. Rev. Lett.* 64, 1943 (1990).
- [13] V. T. Bubelik, S. S. Gorelik , A. A. Zaitsev and A. Y. Polyakov *Phys. Status Solidi b*, 66, 427 (1974).
- [14] K. Brunner, J. Zhu, C. Miesner, G. Abstreiter, O. Kienzle and F. Ernst, *Physica E*, 7, 881 (2000).
- [15] J. Tersoff and F. K. LeGoues, *Phys. Rev. Lett.* 72, 3570 (1994).
- [16] F. Liu, F. Wu and M. G. Lagally, *Chem. Rev.* 97, 1045 (1997).

-
- [17] K. Brunner, *Rep. Prog. Phys.* 65, 27 (2002).
- [18] J. W. Matthews and A. E. Blakesley, *J. Cryst. Growth* 27, 118 (1974).
- [19] B. W. Dodson and J. Y. Tsao, *Appl. Phys. Lett.* 51, 1325 (1987).
- [20] C. Priester and M. Lannoo, *Phys. Rev. Lett.* 75, 93 (1995).
- [21] Y. Chen and J. Washburn, *Phys. Rev. Lett.* 77, 4046 (1996).
- [22] J. L. Liu, J. Wan, K. L. Wang and D. P. Yu, *J. Cryst. Growth* 251, 666 (2003).
- [23] J. Tersoff, C. Teichert and M. G. Lagally *Phys. Rev. Lett.* 76, 1675 (1996).
- [24] J. M. Baribeau, X. Wu, N. L. Rowell and D. J. Lockwood, *J. Phys.: Condens. Matter*, 18, R139 (2006).
- [25] H. Lichtenberger, M. Muhlberger and F. Schaffler, *Appl. Phys. Lett.* 86, 131919 (2005).
- [26] H. Lichtenberger, M. Muhlberger, C. Schelling and F. Schaffler, *J. Cryst. Growth*, 78, 278 (2005).
- [27] R. People, *J. Appl. Phys.* 59, 3296 (1986).
- [28] R. Hull, J. C. Bean, F. Cerdeira, A. T. Fiory, J. M. Gibson, *Appl. Phys. Lett.* 48, 56 (1986).
- [29] G. Jin, J. L. Liu, K. L. Wang, *Appl. Phys. Lett.* 76, 3591 (2000).
- [30] *Epitaxy: Physical Principles and Technical Implementation*, Springer-Verlag, 2003.
- [31] *Molecular Beam Epitaxy: Application to Key Materials*, Noyes Publications, USA, 1995.
- [32] *Growth Processes and Surface Phase Equilibria in Molecular Beam Epitaxy*, Springer, 1999.
- [33] *Transmission Electron Microscopy: Vol 1, 2, 3 & 4*, Plenum Publishing Corporation, New York, USA. 1st Ed.
- [34] F. Schaffler, *Semicond. Sci. Technol.* 12, 15151549 (1997).
- [35] R. People and J. C. Bean, *Appl. Phys. Lett.*, vol. 48, 538 (1986).
- [36] C. G. V. Walle and R. M. Martin, *Phys. Rev. B*, 34, 5621 (1986).
- [37] T. P. Russell, *Materials Science Reports*, 5, 171 (1990).

- [38] J. Daillant and A. Gibaud, editors. *X-ray and Neutron Reflectivity: Principles and Applications*, Springer, Berlin / Heidelberg, 1999.
- [39] M. Tolan, *X-ray Scattering from Soft Matter Thin Films: Material Science and Basic Research*, Springer, Berlin / Heidelberg, 1999.
- [40] L. G. Parrat, *Physical Review*, 95, 359 (1954).
- [41] B. E. Warren, *X-Ray Diffraction*, Dover Publications, Inc., New York (1990).
- [42] M. Tomitori, K. Watanabe, M. Kobayashi and O. Nishikawa, *Appl. Surf. Sci.* 76/77, 322 (1994).
- [43] J. Tersoff, C. Teichert and M. G. Lagally, *Phys. Rev. Lett.* 76, 1675 (1996).
- [44] C. Teichert, M. G. Lagally, L. J. Peticolas, J. C. Bean and J. Tersoff, *Phys. Rev. B*, 53, 16334 (1996).
- [45] F. Liu, S. E. Davenport, H. M. Evans, and M. G. Lagally, *Phys. Rev. Lett.*, 82, 2528 (1999).
- [46] D. Bougeard, K. Brunner and G. Abstreiter, *Physica E*, 16, 609 (2003).
- [47] G. Matmon, D. J. Paul, L. Lever, M. Califano, Z. Ikonik, R. W. Kelsall, J. Zhang, D. Chrastina, G. Isella, H. von Kanel, E. Muller and A. Neels, *J. Appl. Phys.* 107, 053109 (2010).
- [48] D. B. Aubertine, N. Ozguven, and P. C. McIntyre, S. Brennan, J. O. Chu and P. M. Mooney, *J. Appl. Phys.* 94, 3 (2003).
- [49] N. Ozguven and P. C. McIntyre, *Appl. Phys. Lett.* 92, 181907 (2008).
- [50] B. Saha, M. Sharma, A. Sarma, A. Rath, P. V. Satyam, P. Chakraborty and M. K. Sanyal, *Appl. Surf. Sci.*, 256, 547 (2009).
- [51] P. H. Tan, K. Brunner, D. Bougeard and G. Abstreiter, *Phys. Rev. B*, 68, 125302 (2003).
- [52] M. I. Alonso and K. Winer, *Phys. Rev. B*, 39, 10056 (1989).
- [53] P. A. Temple and C. E. Hathaway, *Phys. Rev. B*, 7, 3685 (1973).
- [54] J. S. Lannin, *Phys. Rev. B*, 16, 1510 (1977).
- [55] B. A. Weinstein, M. Cardona, *Phys. Rev. B*, 7, 2545 (1973).
- [56] Z. Sui, I. P. Herman and J. Bevk, *Appl. Phys. Lett.* 58, 2351 (1991).
- [57] J. L. Liu, J. Wan, Z. M. Jiang, A. Khitun, K. L. Wang and D. P. Yu, *J. Appl. Phys.* 92, 6804 (2002).

- [58] S. H. Kwok, P. Y. Yu, C. H. Tung, Y. H. Zhang, M. F. Li, C. H. Peng and J. M. Zhou, *Phys. Rev. B*, 59, 4980 (1999).
- [59] F. Cerdeira, C. J. Buchenauer, F. H. Pollak and M. Cardona, *Phys. Rev. B*, 5, 580 (1972).
- [60] A. B. Talochkin, V. A. Markov and V. I. Mashanov, *Appl. Phys. Lett.* 91, 093127 (2007).
- [61] A. B. Talochkin and A. G. Cherkov, *Nanotechnology*, 20, 345702 (2009).
- [62] Robert Hull and John C. Bean, *Semiconductors and Semimetals*, Vol. 56, Academic Press (1999).
- [63] M. Dubslaff, M. Hanke, S. Schoder, M. Burghammer, T. Boeck and J. Patommel, *Appl. Phys. Lett.* 96, 133107 (2010).
- [64] A. Malachias, M. Stoffel, M. Schmidbauer, T. U. Schulli, G. Medeiros-Ribeiro, O. G. Schmidt, R. Magalhaes-Paniago and T. H. Metzger, *Phys. Rev. B*, 82, 035307 (2010).
- [65] C. Mocuta, J. Stangl, K. Mundboth, T. H. Metzger, G. Bauer, I. A. Vartanyants, M. Schmidbauer and T. Boeck, *Phys. Rev. B*, 77, 245425 (2008).
- [66] T. U. Schulli, G. Vastola, M. I. Richard, A. Malachias, G. Renaud, F. Uhlik, F. Montalenti, G. Chen, L. Miglio, F. Schaffler and G. Bauer, *Phys. Rev. Lett.* 102, 025502 (2009).
- [67] M. I. Richard, V. Favre-Nicolin, G. Renaud, T. U. Schulli, C. Priester, Z. Zhong and T. H. Metzger, *Appl. Phys. Lett.* 94, 013112 (2009).
- [68] G. Chang, G. Vastola, H. Lichtenberger, D. Pachinger, G. Bauer, W. Jantsch, F. Schaffler and L. Miglio, *Appl. Phys. Lett.* 92, 113106 (2008).
- [69] P. Zaumseil, G. G. Fischer, K. Brunner and K. Eberl, *J. Appl. Phys.* 81, 9 (1997).
- [70] J. M. Baribeau, X. Wu, N. L. Rowell and D. J. Lockwood, *J. Phys.: Condens. Matter* 18, R139 (2006).
- [71] M. K. Sanyal, S. K. Sinha, A. Gibaud, K. G. Huang, B. L. Carvalho, M. Rafailovich, J. Sokolov, M. X. Zhao and W. Zhao, *Europhys. Lett.*, 21, 691 (1993).
- [72] M. K. Sanyal, J. K. Basu, A. Datta and S. Banerjee, *Europhys. Lett.*, 36, 265 (1996).
- [73] J. J. Zhang, N. Hrauda, H. Groiss, A. Rastelli, J. Stangl, F. Schaffler, O. G. Schmidt and G. Bauer, *Appl. Phys. Lett.*, 96, 193101 (2010).

- [74] J. M. Vandenberg, A. T. Macrander, R. A. Hamm and M. B. Panish, *Phys. Rev. B*, 44, 8, 3991 (1991).
- [75] X. G. He, M. Erdtmann, R. Williams, S. Kim, and M. Razeghi, *Appl. Phys. Lett.* 65, 2812 (1994).
- [76] C. W. Zhao, Y. M. Xing, J. Z. Yu and G. Q. Han, *Physica B*, 405, 3433 (2010).
- [77] S. K. Sinha, M. K. Sanyal, S. K. Satija, C. F. Majkrzak, D. A. Neumann, H. Hommad, S. Szpalad, A. Gibaud and H. Morkoc, *Physica B*, 198, 72 (1994).
- [78] W. Kissinger, H. J. Osten, G. Lippert, B. Dietrich and E. Bugiel, *J. Appl. Phys.* 76, 8042 (1994).
- [79] J. Tersoff, B. J. Spencer, A. Rastelli, and H. von Kanel, *Phys. Rev. Lett.* 89, 196104 (2002).
- [80] Y. W. Mo and M. G. Lagally, *J. Crys. Growth*, 111, 876 (1991).
- [81] E. Sutter, P. Sutter and J. E. Bernard, *Appl. Phys. Lett.* 84, 2262 (2004).
- [82] P. D. Nellist and S. J. Pennycook, *Advances in Imaging and Electron physics*, 113, 147 (2000).
- [83] D. Grutzmacher, T. Fromherz, C. Dais, J. Stangl, E. Muller, Y. Ekinici, H. H. Solak, H. Sigg, R. T. Lechner, E. Wintersberger, S. Birner, V. Holy, G. Bauer, *Nanolett.* 7, 3150 (2007).
- [84] D. J. Paul, *Adv. Mater.* 11, 191 (1999).
- [85] H. C. Chen, C. W. Wang, S. W. Lee, L. J. Chen, *Adv. Mater.* 18, 367 (2006).
- [86] K. L. Wang, D. Cha, J. Liu, C. Chen, *Proceedings of the IEEE*, 95, 1866 (2007).
- [87] P. Boucand, S. Sauvage, M. Elkurdi, E. Mercier, T. Brunhes, V. Le. Thanh, D. Bouchier, O. Kermarrec, Y. Campidelli, D. Bensahel, *Phys. Rev. B*, 64, 155310 (2001).
- [88] F. Liu, M. G. Lagally, *Phys. Rev. Lett.* 76, 3156 (1996).
- [89] R. M. Tromp, *Phys. Rev. B*, 47, 7125 (1993).
- [90] J. Tersoff, *Phys. Rev. B*, 43, 9377 (1991).
- [91] F. Liu, F. Wu, M. G. Lagally, *Chem. Rev.* 97, 1045 (1997).
- [92] H. H. Cheng, W. P. Huang, V. I. Mashanov, G. Sun, *Jour. Appl. Phys.* 108, 044314 (2010).

- [93] H. H. Cheng, C. T. Chia, V. A. Markov, X. J. Guo, C. C. Chen, Y. H. Peng, C. H. Kuan, *Thin Solid Films*, 369, 182 (2000).
- [94] Y. L. Soo, G. Kioseoglou, S. Huang, S. Kim, Y. H. Kao, Y. H. Peng, H. H. Cheng, *Appl. Phys. Lett.* 78, 3684 (2001).
- [95] A. Malachias, S. Kycia, G. Medeiros-Ribeiro, R. Magalhaes-Paniago, T. I. Kamins, R. Stanley Williams, *Phys. Rev. Lett.* 91, 176101 (2003).
- [96] T. Takagahara, K. Takeda, *Phys. Rev. B*, 46, 15578 (1992).
- [97] C. S. Peng, Q. Huang, W. Q. Cheng, J. M. Zhou, Y. H. Zhang, T. T. Sheng, C. H. Tung, *Phys. Rev. B*, 57, 8805 (1998).
- [98] T. U. Schulli, J. Stangl, Z. Zhong, R. T. Lechner, M. Sztucki, T. H. Metzger, G. Bauer, *Phys. Rev. Lett.* 90, 066105 (2003).
- [99] M. K. Sanyal, S. K. Sinha, A. Gibaud, K. G. Huang, B. L. Carvalho, M. Rafailovich, J. Sokolov, X. Zhao, W. Zhao, *Europhys. Lett.* 21, 691 (1993).
- [100] R. Magalhaes-Paniago, G. Medeiros-Ribeiro, A. Malachias, S. Kycia, T. I. Kamins, R. Stan Williams, *Phys. Rev. B*, 66, 245312 (2002).
- [101] O. H. Seeck, C. Deiter, K. Plaum, F. Bertam, A. Beerlink, H. Franz, J. Horboch, H. Schulte-Schrepping, B. M. Murphy, M. Greve, O. Magnussen, *J. Synchrotron Radiat.* 19, 30 (2012).
- [102] M. Sharma, M. K. Sanyal, M. K. Mukhopadhyay, M. K. Bera, B. Saha, P. Chakraborty, *Jour. Appl. Phys.* 110, 102204 (2011).
- [103] M. S. Leite, J. L. Gray, R. Hull, J. A. Floro, R. Magalhaes-Paniago, G. Medeiros-Ribeiro, *Phys. Rev. B*, 73, 121308(R) (2006).
- [104] M. Larsson, A. Elfving, W.X. Ni, G. V. Hansson, P. O. Holtz, *Phys. Rev. B*, 73, 195319 (2006).
- [105] H. Yang, Z. Tao, J. Lin, F. Lu, Z. Jiang, Z. Zhong, *Appl. Phys. Lett.* 92, 111907 (2008).
- [106] C. G. V. Walle, R. M. Martin, *Phys. Rev. B*, 34, 5621 (1986).
- [107] C. S. Peng, Q. Huang, W. Q. Cheng, J. M. Zhou, Y. H. Zhang, T. T. Sheng and C. H. Tung, *Phys. Rev. B*, 57, 8805 (1998).
- [108] G. D. Scholes and G. Rumbles, *Nat. Mat.* 5, 683 (2006).
- [109] D. Grutzmacher, T. Fromherz, C. Dais, J. Stangl, E. Muller, Y. Ekinici, H. H. Solak, H. Sigg, R. T. Lechner, E. Wintersberger, S. Birner, V. Holy, G. Bauer, *Nanolett.* 7, 3150 (2007).

- [110] J. Wan, G. L. Jin, Z. M. Jiang, Y. H. Luo, J. L. Liu and K. L. Wang, *Appl. Phys. Lett.* 78, 1763 (2001).
- [111] J. Wan, Y. H. Luo, Z. M. Jiang, G. Jin, J. L. Liu, Kang L. Wang, X. Z. Liao and J. Zou, *Appl. Phys. Lett.* 79, 1980 (2001).
- [112] C. G. V. Walle and R. M. Martin, *Phys. Rev. B*, 34, 5621 (1986).
- [113] O. G. Schmidt, K. Eberl and Y. Rau, *Phys. Rev. B*, 62, 16715 (2001).
- [114] M. Larsson, A. Elfving, P. O. Holtz, G. V. Hansson and W. -X. Ni, *Appl. Phys. Lett.* 82, 4785 (2003).
- [115] V. L. Thanh, V. Yam, P. Boucaud, F. Fortuna, C. Ulysse, D. Bouchier, L. Vervoort and J. -M. Lourtioz, *Phys. Rev. B*, 60, 5851 (1999).
- [116] Y. L. Soo, G. Kioseoglou, S. Huang, S. Kim, Y. H. Kao, Y. H. Peng and H. H. Cheng, *Appl. Phys. Lett.* 78, 3684 (2001).
- [117] H. H. Cheng, W. P. Huang, V. I. Mashanov and G. Sun, *J. Appl. Phys.* 108, 044314 (2010).
- [118] M. Brehm, M. Grydlik, H. Groiss, F. Hackl, F. Schaffler, T. Fromherz and G. Bauer, *J. Appl. Phys.* 109, 123505 (2011).
- [119] M. Sharma, M. K. Sanyal, B. Satpati and S. K. Ray, *Phys. Rev. B*, 89, 205304 (2014).
- [120] M-Y. Ryu, T. R. Harris, Y. K. Yeo, R. T. Beeier and J. Kouvetakis, *Appl. Phys. Lett.* 102, 171908 (2013).
- [121] J. Weber and M. I. Alonso, *Phys. Rev. B*, 40, 5683 (1989).
- [122] H. Yang, Z. Tao, J. Lin, F. Lu, Z. Jiang and Z. Zhong, *Appl. Phys. Lett.* 92, 111907 (2008).
- [123] C. S. Peng, Q. Huang, W. Q. Cheng, J. M. Zhou, Y. H. Zhang, T. T. Sheng, C. H. Tung, *Phys. Rev. B*, 57, 8805 (1998).
- [124] M. Larsson, A. Elfving, W.X. Ni, G. V. Hansson and P. O. Holtz, *Phys. Rev. B*, 73, 195319 (2006).
- [125] D. J. Lockwood, J-M Baribeau, B. V. Kamenev, E-K Lee and L. Tsybeskov, *Semicond. Sci. Technol.* 23, 064003 (2008).
- [126] J. Y. Marzin, J. M. Gerard, A. Izrael, D. Barrier and G. Bastard, *Phys. Rev. Lett.* 73, 716 (1994).
- [127] K. Brunner, U. Bockelmann, G. Abstreiter, M. Walther, G. Bohm, G. Tran-
kle, and G. Weimann, *Phys. Rev. Lett.* 69, 3216 (1992).

- [128] M. Geller, A. Marent, T. Nowozin, D. Bimberg, N. Akcay and N. Oncan, *Appl. Phys. Lett.* 92, 092108 (2008).
- [129] A. D. B. Maia, E. C. F. da Silva, A. A. Quivy, V. Bindilatti, V. M. de Aquino and I. F. L. Dias, *J. Phys. D: Appl. Phys.* 45, 225104 (2012).
- [130] M. Usman, V. Tasco, M. T. Todaro, M. D. Giorgi, E. P. O'Reilly, G. Klimeck and A. Passaseo, *Nanotechnology* 23, 165202 (2012).
- [131] V. Mliner, M. Bozkurt, J. M. Ulloa, M. Ediger, G. Bester, A. Badolato, P. M. Koenraad, R. J. Warburton and A. Zunger, *Phys. Rev. B* 80, 165425 (2009).
- [132] G. Biasiol and S. Heun, *Phys. Rep.* 500, 117 (2011).
- [133] P. B. Joyce, T. J. Krzyzewski, G. R. Bell, B. A. Joyce and T. S. Jones, *Phys. Rev. B* 58, R15981 (1998).
- [134] A. Lemaitre, G. Patriarche and F. Glas, *Appl. Phys. Lett.* 85, 3717 (2004).
- [135] A. G. Cullis, D. J. Norris, T. Walther, M. A. Migliorato and M. Hopkinson, *Phys. Rev. B* 66, 081305(R) (2002).
- [136] S. Kret, T. Benabbas, C. Delamarre, Y. Androussi, A. Dubon, J. Y. Laval and A. Lefebvre, *J. Appl. Phys.* 86, 1988 (1999).
- [137] A. D. Giddings, J. G. Keizer, M. Hara, G. J. Hamhuis, H. Yuasa, H. Fukuzawa and P. M. Koenraad, *Phys. Rev. B* 83, 205308 (2011).
- [138] N. Liu, J. Tersoff, O. Baklenov, A. L. Holmes, Jr. and C. K. Shih, *Phys. Rev. Lett.* 84, 334 (2000).
- [139] P. B. Joyce, T. J. Krzyzewski, G. R. Bell, T. S. Jones, S. Malik, D. Childs and R. Murray, *Phys. Rev. B* 62, 10891 (2000).
- [140] F. Arciprete, M. Fanfoni, F. Patella, A. Della Pia, A. Balzarotti and E. Placidi, *Phys. Rev. B* 81, 165306 (2010).
- [141] A. Zolotaryov, A. Schramm, Ch. Heyn and W. Hansen, *Appl. Phys. Lett.* 91, 083107 (2007).
- [142] A. Malachias, S. Kycia, G. Medeiros-Ribeiro, R. Magalhaes-Paniago, T. I. Kamins, R. Stanley Williams, *Phys. Rev. Lett.* 91, 176101 (2003).
- [143] I. Kegel, T. H. Metzger, A. Lorke, J. Peisl, J. Stangl, G. Bauer, J. M. Gacia and P. M. Petroff, *Phys. Rev. Lett.* 85, 1694 (2000).
- [144] M. Yahyaoui, K. Sellami, S. Ben. Radhia, K. Boujdaria, M. Chamarro, B. Eble, C. Testelin and A. Lematre, *Semicond. Sci. Technol.*, 29, 075013 (2014).

- [145] R. Leon, Y. Kim, C. Jagadish, M. Gal, J. Zou and D. J. H. Cockayne, *Appl. Phys. Lett.* 69, 1888 (1996).
- [146] E. C. Le. Ru, J. Fack and R. Murray, *Phys. Rev. B*, 67, 245318, (2003).
- [147] L. Chu, M. Arzberger, G. Bhm and G. Abstreiter, *J. Appl. Phys.* 85, 2355 (1999).